FLY-BY-FEEL AEROSERVOELASTICITY

A Dissertation

by

VISHVAS SAMUEL SURYAKUMAR

Submitted to the Office of Graduate and Professional Studies of
Texas A&M University
in partial fulfillment of the requirement for the degree of

DOCTOR OF PHILOSOPHY

Chair of Committee,	Thomas W. Strganac
Committee Members,	Paul G.A. Cizmas
	Othon K. Rediniotis
	Aniruddha Datta
Head of Department,	Rodney Bowersox

December 2016

Major Subject: Aerospace Engineering

ABSTRACT

Recent experiments have suggested a strong correlation between local flow features on the airfoil surface such as the leading edge stagnation point (LESP), transition or the flow separation point with global integrated quantities such as aerodynamic lift. “Fly-By-Feel” refers to a physics-based sensing and control framework where local flow features are tracked in real-time to determine aerodynamic loads. This formulation offers possibilities for the development of robust, low-order flight control architectures.

An essential contribution towards this objective is the theoretical development showing the direct relationship of the LESP with circulation for small-amplitude, unsteady, airfoil maneuvers. The theory is validated through numerical simulations and wind tunnel tests.

With the availability of an aerodynamic observable, a low-order, energy-based control formulation is derived for aeroelastic stabilization and gust load alleviation. The sensing and control framework is implemented on the Nonlinear Aeroelastic Test Apparatus at Texas A&M University. The LESP is located using hot-film sensors distributed around the wing leading edge. Stabilization of limit cycle oscillations exhibited by a nonlinear wing section is demonstrated in the presence of gusts. Aeroelastic stabilization is also demonstrated on a flying wing configuration exhibiting body freedom flutter through numerical simulations.

Soli Deo Gloria

ACKNOWLEDGMENTS

The success of my graduate program owes largely to the professional and considerate advisement of my dissertation supervisor, Dr. Thomas Strganac. He continually put his students first and maintained a supportive environment where I was free to pursue my ideas.

I would like to thank my committee members: Drs. Cizmas, Redionitis and Datta, for their suggestions that helped improve the dissertation. In particular, the discussions during the preliminary exam and the defense were helpful in refining my thoughts.

The visionary and technical monitor for this project, Arun Mangalam, (Senior Scientist, Tao Systems of Integration, Inc), provided the inspiration and the idea of "Fly-By-Feel" sensing and controls. Much of the research is a direct result of many conversations that occurred at Chipotle and Potbelly. Arun provided much technical support right from the details to the big-picture.

I would like to especially thank Yogesh Babbar not just for his critical role in the project as our hardware lead but also for being a great friend and mentor. We co-authored research papers but also composed great music.

Thanks are also due to Dr. Mark Drela/MIT and Dr. Tuncer Cebeci who provided software tools and licenses that were valuable for model validation.

Financial support from NASA's Aeronautics Mission Directorate under Grant No. NNX14AM61A with Martin Brenner as grant monitor, and AFRL under Contract No. FA8650-07-C-3706 with Pete Flick as contract monitor are gratefully acknowledged.

Over the course of my stay at College Station, I've made many friends that have made life at Aggieland meaningful. The many friends at ICF@TAMU, New Hope Church and Confluence (an Indian-music band) richly contributed to life outside the lab.

Finally, thanks to my father, mother and sister for their constant encouragement.

NOMENCLATURE

h	Plunge displacement
α	Pitch displacement
β	Flap displacement
δ	Leading-edge stagnation point displacement
ρ	Air density
ϕ	Velocity potential
a	Distance (normalized by semi-chord) of pitch-axis from mid-chord
b	Airfoil semi-chord
c	Distance (normalized by semi-chord) of control surface pivot from mid-chord
s	Wing span
r	Leading-edge nose radius
η_T	Airfoil thickness distribution
η_C	Airfoil camber distribution
τ	Phase delay
G	Gain parameter
W_A	Aerodynamic work done for a cycle
P_A	Aerodynamic power input to the structure
x_α	Wing center of mass location (normalized by semi-chord)
c_h	Plunge damping

c_α	Pitch damping
k_h	Plunge stiffness
k_α	Pitch stiffness
m_T	Total system mass
m_a	NATA apparatus mass
m_w	NATA wing mass
I_α	Total system inertia about pitching axis
I_a	NATA apparatus inertia about pitching axis
I_w	NATA wing inertia about pitching axis
Q	Heat-transfer rate
U	Free-stream velocity
R_z	Aircraft vertical displacement
θ	Euler pitch angle
ϕ	Euler roll angle
Γ	Circulation

TABLE OF CONTENTS

LIST OF FIGURES

LIST OF TABLES

1 INTRODUCTION

The increasing interest in the development of flexible high-performance flight vehicles employing advanced sensing and control architectures has driven aeroservoelasticity (ASE) [1] research in recent times. Structurally efficient configurations are expected for actively controlled flexible aircraft that optimally exploit aero-structural interactions to minimize weight and improve performance. However, with the performance benefits obtained from lighter, flexible wings is the concomitant need to address potential ASE-related instabilities. Of significant interest is the development of optimal control solutions to efficiently and safely manage aero-structural interactions that are robust to external disturbances and model uncertainty.

Previous methods to mitigate aeroelastic instabilities include passive and active approaches. The benefits obtained from passive aeroelastic tailoring of the structure are limited by constraints such as material damage tolerance/durability [2] and the inability to adapt in-flight to off-design conditions. The active approach, utilizing a distributed network of sensors and actuators, is more efficient in that guidance and navigation objectives, the flexible aircraft structure and the unsteady aerodynamic environment may be managed in an integrated real-time framework that is responsive to uncertainty and external disturbances.

However, the conventional approach for active controls to suppress aeroelastic instabilities using state-feedback techniques suffers from several limitations. Since full-state feedback is required for optimality, modern controller synthesis (H_2, H_∞) produces high-order control structures that are sensitive to model uncertainty and may pose hardware implementation issues. High-order controllers are the consequence of using large-dimensional ASE models for controller synthesis. The multiplicity is a result of including states associated with rigid-body dynamics, flexible modes, circulation and actuator dynamics.

State-feedback approaches are also strongly model-dependent, and therefore, controller performance may be compromised if model uncertainties are significant. In particular, aerodynamic state estimates are subject to much uncertainty due to the lack of a real-time aerodynamic observable. ASE control systems typically employ inertial sensors such as accelerometers or gyroscopes to estimate aerodynamic states indirectly from the response of the structure using an unsteady aerodynamic model. The accuracy of the aerodynamic state estimates therefore depends on the quality of the aerodynamic model employed.

Large dimensional controller structures are unattractive for hardware realizations. In addition to implementation issues, the problem of controller fragility [3] may require additional consideration. Finally, high-order control structures may pose difficulties

for verification and validation procedures [4]. Compared to low-order classical control methods, various interactions between system modes, inputs and outputs are not as clear and transparent.

An alternative framework for ASE – "Fly-By-Feel" – uses a physics-based aerodynamic sensing method to measure aerodynamic circulation in real-time. The method determines global aerodynamic quantities of interest such as lift by tracking localized critical flow features on the airfoil surface such as the leading-edge stagnation point (LESP), transition or flow separation. Previous experimental studies have suggested a strong correlation between integrated aerodynamic quantities (e.g. C_L) and local flow features. Due to the availability of a real-time observable of circulation, tighter uncertainty bounds on the aerodynamic state estimates may be expected, leading to superior controller performance. In addition, the sensing method also offers the possibility of using measured aerodynamic loads directly in low-order feedback structures for flutter suppression and gust load alleviation.

1.1 Research Objectives

The primary objective of this research is to investigate Fly-By-Feel aerodynamic sensing for ASE and thereby demonstrate that many of the issues (uncertainty, large-dimensionality, etc) with the conventional approach to ASE (using inertial sensors) may be largely avoided. For this purpose, the relationship of the LESP to lift for unsteady airfoil

maneuvers is characterized using unsteady thin-airfoil theory, numerical simulations and wind tunnel tests. Control methods for aeroelastic stabilization utilizing measured loads are developed based on energy methods. Low-order control structures are shown to be effective for aeroelastic stabilization and gust load alleviation. The sensing and control method was demonstrated on the Nonlinear Aeroelastic Test Apparatus (NATA) at Texas A&M University. Limit cycle oscillations exhibited by a nonlinear wing section were suppressed even in the presence of oncoming gust disturbances. In addition, the control method is demonstrated for a flying wing configuration exhibiting Body-Freedom-Flutter (BFF) using ASWING, an ASE analysis code. Specific contributions are summarized as follows:

1. An unsteady aerodynamic model based on the LESP is developed using thin-airfoil theory. The model is validated using numerical simulations and wind tunnel tests.
2. A low-order energy-based control method using aerodynamic load feedback is developed and demonstrated on a nonlinear wing section (NATA) and a flying wing configuration (ASWING). Stability and robustness characteristics for the NATA are analyzed using the aerodynamic work functional concept.
3. Aerodynamic loads estimation methods are developed using load transducers. Cross-validation studies are conducted for loads measurements obtained from load transducers, hot-film sensors and airfoil kinematics. Calibration methods are developed for loads estimated using hot-film sensors and airfoil kinematics using the load transducer as a reference. System identification procedures for the NATA are developed

and validated.

1.2 Outline

The dissertation is organized as follows:

Section 1 , the current section, introduced the research problem, motivation and research objectives.

Section 2 presents a literature review of previous work relevant to this research. A brief overview on past studies on aeroelasticity, flutter suppression and fly-by-feel sensing is provided.

Section 3 develops an unsteady aerodynamic model based on the LESP. Thin-airfoil approximations are employed, closely following Theodorsen's approach to analyze the unsteady aerodynamics of an oscillating airfoil. The theory is validated using numerical simulations and wind tunnel tests for a variety of airfoil maneuvers – oscillations in pitch, plunge and control surface modes and gusts. The material is a reproduction of Ref. [5] with minor changes.

Section 4 describes the experimental hardware and the associated sensor suite. Physics-based loads estimation methods are derived for measurements made using load transducers, hot-film sensors and airfoil kinematics. System identification and calibration procedures for the NATA are also described. Representative test results illustrating the relevant physics are discussed.

Section 5 presents the energy-based sectional control approach using measured aerody-

namic loads demonstrated on the NATA. The NATA system model is described and is used for controller characterization. Stability properties of the control structure are analyzed using the aerodynamic work functional concept. The influence of controller gains on stabilization performance is investigated. Experimental results demonstrating the performance of the controller are discussed.

Section 6 extends the sectional sensing and control approach to a swept flying wing configuration exhibiting body-freedom-flutter. The controller performance is demonstrated and analyzed using ASWING.

Section 7 presents important conclusions drawn from this research. Opportunities for future research are identified.

2 BACKGROUND *

2.1 Aeroservoelasticity

Aeroservoelasticity (ASE) is a multidisciplinary field that deals with the interaction of active control systems, the flexible aircraft structure and the unsteady aerodynamic environment. The field has received significant attention in recent times as the aerospace industry continues to make significant progress towards the use of advanced light-weight materials enabled by the development of high-performance actuators and information-rich sensors. These interactions cannot be ignored for flexible vehicles and requires an integrated approach to design effective control strategies. In particular, careful consideration of potential instabilities arising out of such interactions is necessary. Instabilities such as flutter, a dynamic instability occurring due to a coalescence of aeroelastic modes, may be precipitously catastrophic. Control systems designed to suppress such instabilities therefore must be sufficiently robust to uncertainties and external disturbances to satisfy required safety margins. A partial aeroservoelasticity research history and potential for future applications are described by Mukhopadhyay and Livne [6, 7].

*Part of this section is reprinted from "Unsteady Aerodynamic Model based on the Leading-Edge Stagnation Point" by Vishvas S. Suryakumar, Yogesh Babbar, Thomas W. Strganac, and Arun S. Mangalam, 2016, Journal of Aircraft, Vol. 53, No. 6, pp. 1626-1637. Copyright 2016 by Vishvas S. Suryakumar, Yogesh Babbar, Thomas W. Strganac, and Arun S. Mangalam.

2.2 Active Flutter Suppression

The Wright brothers on their historic flight (17 December 1903) used wing flexibility for roll control of the aircraft [8]. The wing tips were twisted with a cable control actuation system and thereby stable flight was achieved. Since then, significant progress has been made in the past century. A major contribution to active controls research was the X-53 Active Aeroelastic Wing (AAW) program [9]. A modified F/A-18 aircraft was used to demonstrate improved aircraft performance utilizing a multidisciplinary framework involving aerodynamics, active controls and advanced structures. In particular, wing flexibility was exploited to improve roll performance. A more recent effort is the development of the re-configurable X-56 Multi-Utility Technology Testbed (MUTT) [10]. The X-56 vehicle is uniquely suited in its ability to exhibit body-freedom-flutter phenomena and serves as a testbed to demonstrate flutter suppression concepts. The SensorCraft program [11] is another area of active aeroelastic control applied to high-aspect ratio aircraft that seeks to incorporate advanced sensing technologies in addressing Intelligence, Surveillance and Reconnaissance (ISR) capabilities. Gust-load alleviation using aeroservoelastic control has been previously demonstrated in wind tunnel tests [12].

In addition, active controls have been extensively studied through analytical and experimental studies on two degree of freedom wing sections. Two important facilities that have been used for these studies are the Benchmark Active Control Technologies wing (BACT) [13] and the Nonlinear Aeroelastic Test Apparatus (NATA) [14]. Flight

tests have previously shown the existence of nonlinear responses such as limit cycle oscillations (LCOs) occurring even within the flight envelope. The NATA platform, designed to study such nonlinear responses, is capable of exhibiting LCOs as a result of a spring-hardening type structural nonlinearity in the pitch stiffness. The test-bed has been extensively characterized in several previous studies and physics-based models have been developed [15]. Various linear and nonlinear control strategies were investigated and demonstrated experimentally on the NATA test-bed. In particular, Block and Strganac [16] used a LQG controller employing a full-span trailing-edge control surface. The Kalman filter was used to estimate non-measurable states such as the aerodynamic lag-states. The controller successfully stabilized the system, if activated during a developing LCO. However, its capability was limited when applied after the LCO had fully developed. Nonlinear controller approaches based on adaptive feedback linearization scheme were also developed [17, 18]. Adaptive control was found to be necessary to compensate for the inexact cancellation of nonlinearities (via feedback linearization). In an effort to improve controller performance, Platinitis et al [19] used both the wing leading and trailing edge control surfaces. Though stabilization was achieved, the control commands were saturated and the wing settled in a non-zero pitch and plunge equilibrium. Zebb et al [20], demonstrated an LPV controller that was auto-scheduled with airspeed. The controller was able to quickly stabilize the system using only the trailing edge control surface through allowable wind tunnel speeds.

Typically, active control methods are strongly model-dependent. For the previous studies reviewed for the NATA platform, the control development was based on a simplified aeroservoelastic model for the nonlinear airfoil section. For several cases, the quasi-steady assumption was used to simplify aerodynamic modeling. The simplicity of the model facilitated the development of provably stable nonlinear controllers. However, in general, for three dimensional flexible flight vehicle configurations, it is difficult to derive analytically or identify from data, similar simplified models that adequately represent the physics. Accordingly, model-based control structures tend to be of high-order due to the complexity of the aero-structural model. In addition, controller performance is significantly limited by model uncertainties. For instance, accident investigations of the NASA Helios crash concluded that causes included limited modeling capabilities and an inadequate understanding of the complex nonlinear interactions between unsteady aerodynamics, flexible structures and control systems [21]. Often, modeling the unsteady aerodynamics is the more challenging aspect that is subject to significant uncertainty. High-angle of attack phenomena, effect of gusts, crossflow and fuselage-wing interactions, remain a challenge to accurately model. The uncertainty arises primarily due to the lack of a real-time aerodynamic observable. The current practice to estimate unsteady aerodynamic loads indirectly from the response of the structure (using inertial sensors such as accelerometers and gyroscopes) suffers from the aforementioned limitations.

2.3 Fly-By-Feel Sensing

As discussed, model-based control synthesis methods for flexible aircraft use complex aero-structural models. Such models are obtained either using computational methods or identified from flight test data, and do not typically involve an aerodynamic observable apart from the aircraft angle-of-attack and similar kinematic states. Without an aerodynamic observable, aerodynamic effects, such as the effect of separated flows on aerodynamic forces and moments, must be inferred from the inertial states, resulting in significant uncertainty in the aerodynamic model. Consequently, to reduce uncertainty, a large number of experiments need to be conducted to interpolate the space parameterized by flight conditions, which is an expensive process. Accordingly, to simplify the parameter space, the approximation of these complex systems has spurred interest in the development of reduced-order models (ROMs) [22]. However, ROMs based on system identification techniques are often less reliable outside the operating space from which they are derived, indicating that the ROMs are strongly data dependent. The unsteady aerodynamics, which is a function of the structural states, the wake and external disturbances such as gusts, is the more difficult component to identify accurately. For instance, considering very flexible wings, modeling aerodynamic nonlinear behavior such as dynamic stall requires a complex nonlinear state-space semi-empirical approach [23], posing a challenge for accurate identification. Consequently, control design for flexible aircraft, taking into account robustness, high-dimensionality and nonlinearities, is a challenging task and continues to remain an active area of research.

However, a new direction [24] seeks to directly sense the spatio-temporal aerodynamic environment instead of modeling the circulation developed around the wing. With the use of an aerodynamic observable, tighter uncertainty bounds are expected and aerodynamic data such as the span-wise lift coefficient may be obtained real-time. Incorporating distributed aerodynamic output-feedback with co-located actuation could lead to an efficient control system that is robust to the uncertain environment. This direction is a transition in control-design philosophy from the use of complex models towards directly utilizing information-rich sensors, potentially simplifying controller synthesis and improving robustness. Utilizing real-time aerodynamic feedback also offers possibilities of optimizing aircraft performance objectives online, judiciously exploiting structural flexibility and the aerodynamic environment. In addition, distributed sensing and control could provide aircraft with adequate redundancy against sensor and/or actuator failure.

An effort in this direction is the use of a distributed flush-air data system (FADS) [25] for health-monitoring and stability augmentation. This method involves the use of static-pressure ports that are strategically placed at locations of maximum pressure sensitivity. Sectional airfoil coefficients may then be derived from these measurements. An alternative approach that is explored in this paper is the use of sensors to identify Critical Aerodynamic Flow Feature Indicators (CAFFIs) [26]. Such indicators (Fig. 2.1) include points of "flow bifurcation" such as the leading edge stagnation point (LESP), flow separation/reattachment points, and other locations of significance such as the

shock location and boundary-layer transition. Intuitively, we expect integrated quantities such as lift, drag or moments to be strongly correlated with local flow features such as the LESP and the flow separation point [27, 28]. The CAFFIs may thus be treated as real-time observables representing the current aerodynamic state. Indeed, several recent experiments and studies [2, 26, 29–32] from wind tunnel tests to flight tests, have confirmed this observation. In addition, sensor calibration and associated concerns (range of validity, drift and accuracy) are rendered less critical, if the CAFFIs are accurately located with minimal calibration. This is accomplished using relative measures and phase-based signal processing techniques [30]. CAFFIs may be identified using several flow properties at the wing surface level – pressure, shear stress or heat-transfer. Previous studies mentioned have demonstrated the use of hot-film sensors to identify the LESP using distributed convective heat-transfer measurements. CAFFIs have advantages over the previously mentioned FADS-based static-pressure ports. In addition to being less dependent on calibration, the theoretical analysis, particularly unsteady aerodynamics, is more easily treated using CAFFIs as will be shown in the following sections.

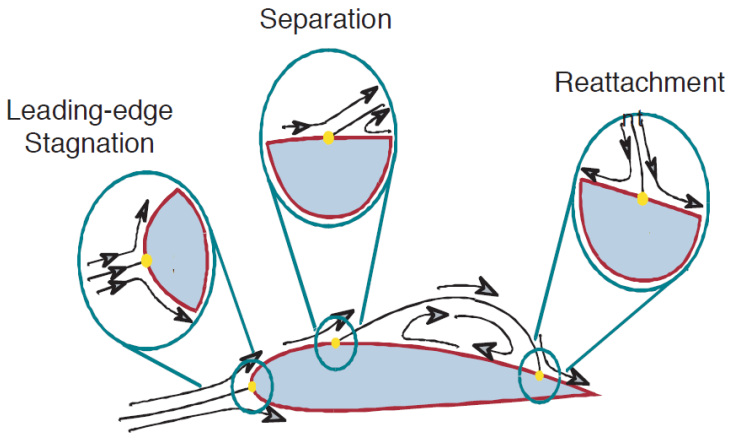

Figure 2.1: Critical Aerodynamic Flow Feature Indicators (CAFFIs) [24]

For steady flows, it is well-known that the LESP is directly related to the angle of attack [33], and hence, the lift. However, references in the literature concerning the LESP and its relation to unsteady aerodynamics are scarce. McCroskey [34] provides frequency-domain formulas for the chord-wise movement of the LESP for a thin oscillating airfoil. But no subsequent efforts are made to relate the LESP to the lift. Similarly, for an oscillating thick airfoil, Woods [27] derives frequency-domain formulas for the LESP movement. A primary objective of this research therefore is to formulate the necessary theory that relates the stagnation point to the unsteady lift.

3 UNSTEADY AERODYNAMIC MODEL BASED ON THE LEADING-EDGE STAGNATION POINT *

3.1 Introduction

In this section, the relationship between the LESP and the lift is derived using first-order potential flow assumptions and important results from Theodorsen's [35, 36] theory for an oscillating airfoil. However, the model is shown to be valid for arbitrary maneuvers besides simple oscillations. The linearity of the governing equations permits the inclusion of several boundary conditions specified across the chord: pitch, plunge, control surface displacements or gusts. As previously mentioned, current unsteady aerodynamic models for an airfoil use only kinematic states such as pitch angle, plunge displacement and control surface deflections as inputs. To capture the effect of the wake and account for the history of the motion, transfer functions or state-space models are typically employed. The experimental identification of the circulation dynamics involves expensive unsteady wind tunnel tests to fully characterize [37]. However, in using the LESP along with some kinematic states, it is shown that a simple frequency-independent relation for lift is found, i.e., no lag states are needed and the effect of the wake is captured by the LESP. As a result of the model simplicity, the aerodynamic model identification in this case is far less challenging.

*Part of this section is reprinted from "Unsteady Aerodynamic Model based on the Leading-Edge Stagnation Point" by Vishvas S. Suryakumar, Yogesh Babbar, Thomas W. Strganac, and Arun S. Mangalam, 2016, Journal of Aircraft, Vol. 53, No. 6, pp. 1626-1637. Copyright 2016 by Vishvas S. Suryakumar, Yogesh Babbar, Thomas W. Strganac, and Arun S. Mangalam.

The section is organized as follows. An unsteady aerodynamic model based on the LESP is derived and its essential features are discussed. We next describe the verification of the model using numerical simulations and wind tunnel experiments. Numerical simulations involve steady and unsteady panel methods. For the wind tunnel tests, the real-time LESP location is estimated using a hot-film sensor array instrumented around the leading edge of the wing. Finally, potential applications of this technology are outlined. In particular, the application towards active flutter suppression and gust load alleviation is briefly described.

3.2 Model Derivation

For the steady potential flow over an airfoil, the stagnation point on the airfoil surface is a monotonic function of the angle of attack. It lies at a chord-wise distance $x \propto \delta^2$ from the leading edge, where δ is a multiple of the angle of attack [33]. Since C_L vs. α is linear for small angles, C_L vs. δ is also linear. The stagnation point on the airfoil, representing the effective angle of attack, is well-defined and easily located using distributed sensing techniques such as a hot-film array. For unsteady flows, Theodorsen derives a relation between the effective angle of attack and the circulatory part of lift. A similar relationship between the stagnation point and the circulatory lift may therefore be hypothesized. However, the following theoretical development indicates that several other terms – for instance, pitch rate, control surface deflection and its rate – need to be included. For low reduced frequencies, these rate terms may be partially encapsulated in

a $\dot{\delta}$ term, to yield a simpler formulation. The need and the significance of these rate terms are examined in the next section.

Herein, we derive a simple relationship linking the stagnation point to the unsteady lift for a cambered airfoil with thickness and undergoing arbitrary unsteady maneuvers in pitch and plunge modes along with control-surface deflections. The derivation is based on important results derived by Theodorsen for unsteady thin-airfoils. The interpretation of Theodorsen's method as described in Ref. [36] is followed. The velocity distribution for the unsteady flow is first determined, from which the stagnation point location is calculated. Then, using the Kutta condition, we show that the circulatory lift is directly related to the stagnation point.

The solution to the unsteady incompressible, irrotational flow problem around a thin-airfoil is found by solving, $\nabla^2\phi = 0$. The flow solution consists of the freestream (ϕ_∞) and the flow disturbance (ϕ'). The flow disturbances due to the airfoil motion, thickness, camber and control surface displacements are assumed to be encapsulated by the small parameter ϵ, such that:

$$\phi' = \phi'_1 + \phi'_2 + ... \tag{3.1}$$

where $\phi'_i = O(\epsilon^i),\ i = 1,2,3,....$

Since our focus is on obtaining a first-order estimate, higher-order terms are neglected. Accordingly, the boundary conditions reduce to the specification of the normal

velocity across the chord. Following Bisplingoff et al [36], the following disturbance velocity components may be defined:

$$u - U = u' = \frac{\partial \phi'}{\partial x}, v = v' = \frac{\partial \phi'}{\partial y}, w = w' = \frac{\partial \phi'}{\partial z} \tag{3.2}$$

such that $u', v', w' \ll U$. To formulate the boundary conditions, typical thin-airfoil assumptions such as ($|\frac{\partial z}{\partial x}| \ll 1$,$|u| \ll U$) are enforced. Note that these assumptions, and consequently, the flow solution, are invalid in the leading edge region in spite of the formulation providing first-order accurate results for integrated quantities such as lift and moment. The flow perturbation series that is not uniformly valid, particularly at the leading edge, becomes increasingly less accurate as higher order terms are considered. Contrary to the exact solution, thin-airfoil theory predicts an infinite velocity at the leading edge. This is of concern, since the velocity distribution near the leading edge is used to determine the stagnation point. However, using a correction proposed by Reigels [33], it may be shown that a first-order accurate location for the stagnation point may be found regardless of the validity of the first-order velocity distribution near the leading edge. The flow as seen by an observer moving with the airfoil near the leading edge is assumed to be approximately the steady flow around a parabola [38]. Reigels' rule is then given as:

$$\frac{\bar{q_1}}{U} = \left(\frac{s}{s + 0.5r}\right)^{0.5} \frac{q_1}{U} \tag{3.3}$$

where $\bar{q_1}$ is the corrected speed (which is now valid near the leading edge), r is the leading edge radius and s, the chordwise coordinate from the leading-edge. Thus, according to the rule, the stagnation point located by the first-order theory ($q_1 = 0$) will also be the stagnation point using the corrected velocity distribution ($\bar{q_1} = 0$).

Theodorsen constructs the disturbance flow pattern using two sets of singularities. The first set consists of a source-sink sheet distributed across the chord which is used to satisfy the boundary conditions, resulting in non-circulatory effects. The second set consists of vortices distributed across the chord and the shed wake to satisfy the Kutta condition, resulting in the circulatory effect. The boundary conditions here refer to those that produce lift such as the angle of attack, airfoil motion, camber, control surface displacement or gusts. Non-lifting features such as thickness that alter the velocity distribution may simply be superimposed.

The boundary conditions for the airfoil with thickness and camber is linearized and represented as the superposition of the flat-plate with thickness and camber contributions that are treated separately. For mathematical convenience, the problem is expressed in a conformally-mapped plane using the Joukowski transformation. The flat-plate in the xz plane (Fig. 3.1) is transformed to a circle in the XZ plane using:

$$x + iz = (X + iZ) + \frac{b^2}{4(X + iZ)} \tag{3.4}$$

Accordingly, the chordwise stagnation point displacement is related to the angular displacement on the conformally mapped circle assuming $\delta \ll 1$ through:

$$\delta = \sqrt{2(x_\delta / b)} \tag{3.5}$$

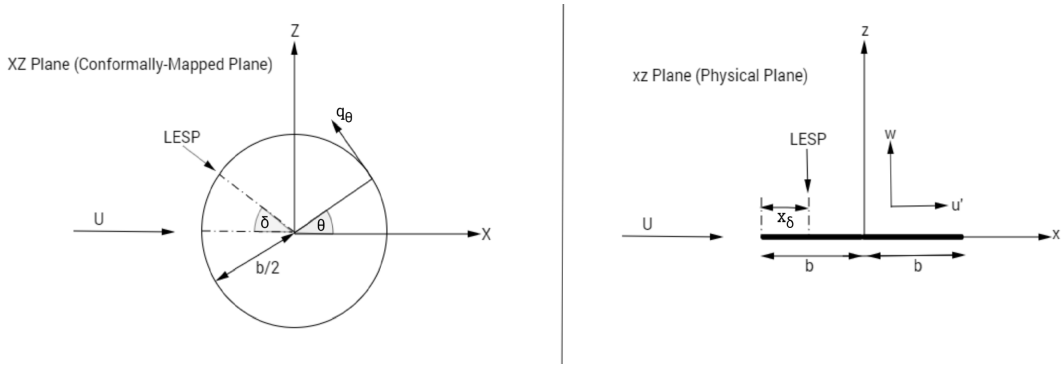

Figure 3.1: Joukowski's Conformal Transformation

To locate the stagnation point, we find the tangential velocity (q_θ) contributions near the leading edge due to non-circulatory, circulatory and thickness effects.

The LESP (δ) is tentatively assumed to be located on the upper surface, i.e., $\theta = \pi - \delta$ such that $\delta \ll 1$. Substituting $\cos(\theta \approx \pi) = -1$ in the tangential velocity distribution (Eq. 5-257, Ref. [36]) due to source-sink non-circulatory singularities, we have:

$$q_{\theta_{NC}} = \frac{2}{\pi} \int_0^\pi \frac{w_a \sin^2 \phi d\phi}{(\cos\phi + 1)} \tag{3.6}$$

where ϕ is the angular co-ordinate on the conformally mapped plane and w_a is the normal velocity across the chord.

Similarly, the circulatory component of the tangential velocity distribution (Eq. 5-281, Ref. [36]) near the leading edge, found by integrating the effect of shed vortices in

the wake and bound vortices in the wing is calculated:

$$q_{\theta_C} = \frac{1}{\pi b}\int_b^\infty \left(\sqrt{\frac{\xi - b}{\xi + b}}\right)\gamma_w d\xi \tag{3.7}$$

where ξ is the location of the wake vortex element on the x axis, and $\gamma_w d\xi$, its circulation strength.

The Kutta condition (Eq. 5-297, Ref. [36]) is given as:

$$\frac{2}{\pi}\int_0^\pi \frac{w_a \sin^2\phi d\phi}{(\cos\phi - 1)} + \frac{1}{\pi b}\int_b^\infty \left(\sqrt{\frac{\xi + b}{\xi - b}}\right)\gamma_w d\xi = 0 \tag{3.8}$$

resulting in the circulatory lift (Eq. 5-294, Ref. [36]):

$$L_C = -\rho U \int_b^\infty \left(\frac{\xi}{\sqrt{\xi^2 - b^2}}\right)\gamma_w d\xi \tag{3.9}$$

From Eqs. 3.7, 3.8 and 3.9, q_{θ_C} is found in terms of L_c:

$$q_{\theta_C} = \frac{2}{\pi}\int_0^\pi \frac{w_a \sin^2\phi d\phi}{(\cos\phi - 1)} + \frac{2}{\pi b}\frac{-L_C}{\rho U} \tag{3.10}$$

The non-lifting thickness contribution to the tangential velocity is now calculated. Specifically, "Joukowski" type thickness profiles of the following form are considered:

$$\bar{\eta}_t = f(\bar{x})\sqrt{(1 - \bar{x}^2)} \tag{3.11}$$

where $\bar{\eta}_t = \eta_t / b$ and $f(\bar{x})$ is a polynomial with $\bar{x} = x/b$. The particular form was chosen since it facilitates the computation of analytical integration. This analytical form may be derived for any commonly used airfoil by fitting the airfoil thickness to this functional form. The first-order accurate velocity distribution for the thickness contribution is calculated from the theory of singular integral equations (Eq. 7.31a, Ref. [39]):

$$\frac{u'_T}{U}(\bar{x}) = \frac{1}{\pi}\int_{-1}^1 \frac{d\bar{\eta}_t}{d\bar{x}}(\bar{x}_0)\frac{d\bar{x}_0}{\bar{x} - \bar{x}_0} \tag{3.12}$$

The velocity (τ) near the stagnation point at the leading edge is found by substituting Eqs. 3.11, 3.12 with $\bar{x} = -1$:

$$\tau = \frac{u'_T}{U}(-1), \tag{3.13}$$

which is then expressed in the circle plane:

$$q_{\theta_T} = -2U\tau\delta \tag{3.14}$$

The total tangential velocity including non-circulatory and circulatory components of the flat plate along with thickness effects is found:

$$q_\theta = q_{\theta_{NC}} + q_{\theta_C} + q_{\theta_T} = \frac{2}{\pi b}\frac{-L_C}{\rho U} - \frac{2}{\pi}\int_0^\pi 2w_a \cos\phi d\phi - 2U\tau\delta \tag{3.15}$$

From an order of magnitude analysis, the resultant velocity (q_1) on the airfoil surface to the first order is given by (Eq. 7.25a, Ref. [39]):

$$q_1 = U + u' \tag{3.16}$$

Therefore, to the first order, the stagnation point will be located at $u' = -U$. Note that the vertical velocity component w does not play a role. Consequently, the stagnation point seen in both inertial and body-fixed frames to the first order may be shown to be equivalent.

At the stagnation point, with $u' = -U$, the tangential velocity is then given by (using Eq. 5-235b, Ref. [36]):

$$q_\theta = 2U\delta \tag{3.17}$$

The boundary conditions representing motion in the pitch, plunge and control surface

modes are now specified across the chord:

$$w_a = w_c - \dot{h} - U\alpha - \dot{\alpha}[x - ba], \qquad -b \leq x \leq bc \tag{3.18}$$

$$w_a = w_c - \dot{h} - U\alpha - \dot{\alpha}[x - ba] - U\beta - \dot{\beta}[x - bc], \qquad bc \leq x \leq b \tag{3.19}$$

where the control surface is hinged at $x = bc$, $x = ba$ is the axis of rotation, and w_c is the normal velocity due to the airfoil camber. In a similar method used to calculate the effect of thickness, the contributions arising from camber are calculated by substituting the normalized airfoil camber, $\bar{\eta}_c = \eta_c/b$, in:

$$w_c = U\frac{d\bar{\eta}_c}{d\bar{x}} \tag{3.20}$$

With Eqs. 3.15, 3.17, 3.18 and 3.19, the circulatory lift is found to be:

$$L_C = 2\pi\rho U^2 b\left(\frac{\dot{\alpha}b}{2U} + \frac{\sqrt{1-c^2}}{\pi}\beta + \frac{b}{2\pi U}\left(\cos^{-1}c - c\sqrt{1-c^2}\right)\dot{\beta} - \frac{(1+\tau)}{2}\delta\right) + L_0 \tag{3.21}$$

The non-circulatory part of lift is not a function of δ. Further simplification may be achieved for low reduced frequencies by partially encapsulating the rate terms using $\dot{\delta}$. From Theodorsen's theory, the effective angle of attack is given as:

$$\alpha_{\text{eff}} = C(k)\left(\alpha + \frac{\dot{h}}{U} + \frac{\dot{\alpha}b(0.5-a)}{U} + \left(\frac{\sqrt{1-c^2} + \cos^{-1}c}{\pi}\right)\beta + \right. \tag{3.22}$$

$$\left.\left(\frac{b(1-2c)\cos^{-1}c + (2-c)b\sqrt{1-c^2}}{2U\pi}\right)\dot{\beta}\right) \tag{3.23}$$

where $C(k)$ is the circulation function.

From Eqs. 3.21 and 3.22, assuming $C(k) \approx 1$ (for low reduced frequencies), ignoring double-time derivatives and the thickness contribution we find:

$$\dot{\alpha} = -0.5\dot{\delta} - \frac{\cos^{-1} c}{\pi}\dot{\beta} \tag{3.24}$$

which is then substituted back in Eq. 3.21 and with the addition of non-circulatory effects (ignoring double-derivatives), a simplified expression for C_L is found:

$$C_L = -(1+\tau)\pi\delta - \frac{\pi b}{U}\dot{\delta} + 2\sqrt{1-c^2}\beta - \frac{2bc\sqrt{1-c^2}}{U}\dot{\beta} + C_{L_0} \tag{3.25}$$

For the steady-flow over a flat-plate, we recover the familiar relationship:

$$\delta = -2\alpha \tag{3.26}$$

3.3 Model Features

The following features are noted about the model:

1. To estimate unsteady lift using the LESP, Eq. 3.21 reveals that a wake model containing aerodynamic lag states is not required for an airfoil executing small amplitude maneuvers. The LESP is therefore an observable for the circulation developed over the airfoil. In contrast, for models based only on airfoil kinematics, an unsteady wake model such as Theodorsen's circulation function [35] or Wagner's indicial response function [40] is required to estimate aerodynamic loads from the structural response. Since the effect of the wake is captured by the LESP, the model results in a low-order form that simplifies identification and implementation for control systems. However, large angle of attack maneuvers involving flow separation will require modeling associated fluid dynamical phenomena not ac-

counted for by the LESP (or other CAFFIs). For airfoil maneuvers involving small amplitudes and low reduced frequencies, the model given by Eq. 3.25 requires only two sensor measurements along with their rates: the LESP and the control surface displacement. Sensor systems currently exist to measure both quantities in real-time.

2. The airfoil thickness affects the slope of the $C_L(\delta)$ curve. However, since both $\delta \ll 1$ and $\tau \ll 1$, the thickness appears as a minor second order effect. The effect of camber is an offset (C_{L_0}) to the $C_L(\delta)$ curve. In the next section, the effects of thickness and camber are examined based on numerical studies. While the relative size of the control surface parameter c appears, the non-dimensional pitch axis location a does not appear in the final form (a and c appear in Theodorsen's result for unsteady lift). This is a useful result, since it is difficult to accurately estimate the elastic axis of the wing for complex wing configurations. a is however required to transfer resultant aerodynamic loads from the quarter-chord.

3. For low reduced frequencies ($k < 0.1$), where the contribution of rate terms is negligible, we expect the lift to be nearly out-of-phase with the LESP. For the reduced frequencies in the medium range ($0.1 < k < 0.3$), where $\ddot{h}$ is not significant and for plunge only motions, the lift and the LESP are again nearly out-of-phase. This observation was also noted in earlier experiments [24, 41]. From the preceding developments, we find the LESP motion captures the effect of a boundary condition

(downwash) if it is constant across the chord or such that $\int_0^\pi w_a \cos\phi d\phi = 0$ (see Eq. 3.15). Accordingly, the pitch rate and the control surface displacement are not entirely captured by the LESP and this results in a few extra terms in Eq. 3.25. As an approximation, slow-gusts and the downwash from the tip-vortices may be treated as an equivalent plunge velocity [42]. Their corresponding effects will therefore be captured by the LESP.

4. The model derived is subject to first-order approximations, i.e, for small angles of attack. The stagnation point in the circle-plane δ, similar to the angle of attack, is a first-order quantity (Eq. 3.26). The physical stagnation point on the airfoil however is second order (Eq. 3.5). Since small angle approximations are invalid beyond $\delta > 10\,\mathrm{deg}$, the linear model is less accurate beyond $\alpha > 5\,\mathrm{deg}$ and a nonlinear empirical fit may be required. For large angles of attack with massive flow separation and associated phenomena such as dynamic stall, potential flow assumptions breakdown. However, if the separation point is measured real-time along with the LESP, then it may be possible to estimate the lift for separated flows. Previous wind tunnel tests have indicated that the lift may be accurately estimated using the surfacewise LESP and flow separation location for large angle of attack quasi-steady maneuvers. Further studies are required to characterize this relationship for dynamic stall.

3.4 Model Validation

The analytical relation between LESP and lift (Eq. 3.25) is validated using both computational and experimental methods. A variety of scenarios are considered to study different aspects of the problem – steady, unsteady, inviscid and viscous. Through this study, thin-airfoil theory predictions based on the LESP and the angle of attack are compared. The value in measuring (using δ) as opposed to modeling (using α) circulation is emphasized.

The normalized airfoil that is used for validating the model (both simulations and experiments) is shown in Fig. 3.2 along with the thickness and camber profiles.

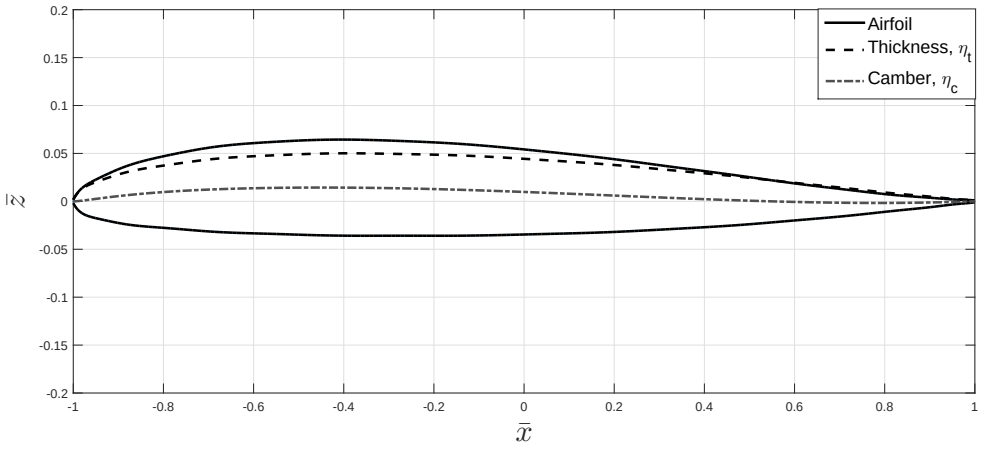

Figure 3.2: Airfoil Geometry used for Model Validation

The thickness is found to be approximated by:

$$\bar{\eta}_t = f(\bar{x})\sqrt{(1-\bar{x}^2)} = (0.089 - 0.057\bar{x} - 0.016\bar{x}^2)\sqrt{(1-\bar{x}^2)} \tag{3.27}$$

Using the integral formulas in Ref. [39], we find from Eq. 3.13: $\tau = 0.1628$

Similarly, the camber is found to be approximated by:

$$\bar{\eta}_c = 0.0197 - 0.036\bar{x} - 0.019\bar{x}^2 + 0.036\bar{x}^3 \tag{3.28}$$

From Eqs. 3.15 and 3.20, we find: $C_{L_0} = 0.12$

To determine the chord-wise stagnation point x_δ computationally, the point of minimum flow speed is simply found from the panel/grid solution at the airfoil surface for each time-step. The accuracy of estimating the stagnation point is then only dependent on the panel resolution. However, in a practical setting, it is difficult to accurately ascertain the airfoil shape and the sensor locations on the surface in terms of a cartesian co-ordinate grid. In such a case, the nose region of the airfoil may be approximated by a parabola: $x = \frac{z^2}{2r}$. Only the leading-edge nose radius need be measured. Since the surface-wise distances from the leading-edge of the sensors are known relatively accurately, it is then possible to straightforwardly estimate their corresponding chord-wise locations based on the identified parabola. The chord-wise locations are subsequently mapped to the circle plane to determine δ. However, a small error is accrued due to the misalignment of the parabola axis and the chordline.

Due to the discretization inherent in the use of grid points or sensors, the LESP motion may appear noisy. To obtain smooth estimates of the LESP as it transitions between sensors, the minimum is found from a three-point interpolation scheme using neighboring

sensors on either side of the sensor that records the minimum speed.

3.4.1 Computational Results

Panel-method based numerical simulations are employed to evaluate the analytical model predictions. The steady case is computed using the steady panel code (X-Foil) developed by Drela and Giles [43] and the unsteady case using the unsteady panel code developed by Cebeci [44]. The stagnation point is calculated from the velocity distribution around the nose region. Sufficient refinement is therefore required of the panel discretization around the leading edge. For the numerical study, the airfoil of unit chord is considered. With the control-surface pivot location fixed at $c = 0.5$, the LESP model (Eq. 3.25) is summarized as:

$$C_L = -3.653\delta - 0.5\pi\frac{\dot{\delta}}{U} + 1.732\beta - 0.433\frac{\dot{\beta}}{U} + 0.12 \tag{3.29}$$

Steady Flow

Figure 3.3 compares the thin-airfoil theory predictions with the panel method for both inviscid and viscous cases through various angles of attack and control surface deflections. For the inviscid case, the thin-airfoil theory predictions are accurate for small angles of attack. Minor discrepancies set in for larger angles, since the small angle approximation loses validity and second order effects become significant. The 'C_L vs. α' curve shows discrepancies at larger angles that are more conspicuous than 'C_L vs. δ'. Interestingly, for the viscous case, although the 'C_L vs. α' panel result reveals discrepancies due to Reynolds number effects, the inviscid thin-airfoil theory based on LESP does better in comparison. The behavior of C_L with δ remains mostly linear

regardless of viscous effects. The result, therefore, suggests that the change in potential flow circulation due to viscous effects happens to be captured inherently by the LESP. Viscous effects result in the formation of a boundary layer that changes the effective shape of the airfoil seen by the potential flow. Consequently, the circulation, and hence, the lift and the LESP are accordingly affected.

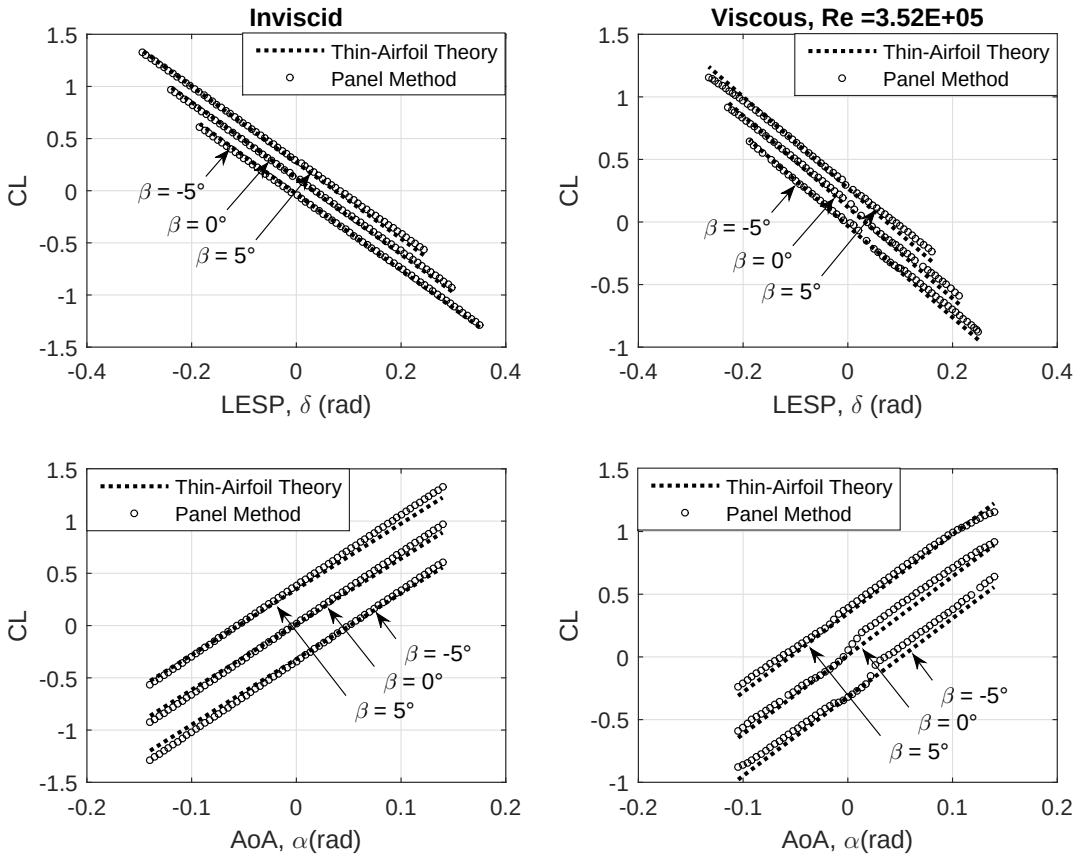

Figure 3.3: Steady Flow Results for Various Angles of Attack and Control Surface Deflections

We next study the contribution of thickness and the error incurred as a result of approximating the nose region as a parabola. Note from Fig. 3.4, the contribution from thickness effects as expected from the theory is a change in slope. Also, the effect of approximating the nose region as a parabola does not cause a significant error. The nose region is approximated with a parabola of nose radius 1% chord. Furthermore, for small δ, the errors introduced as a result of neglecting the thickness effect and the parabola approximation are insignificant.

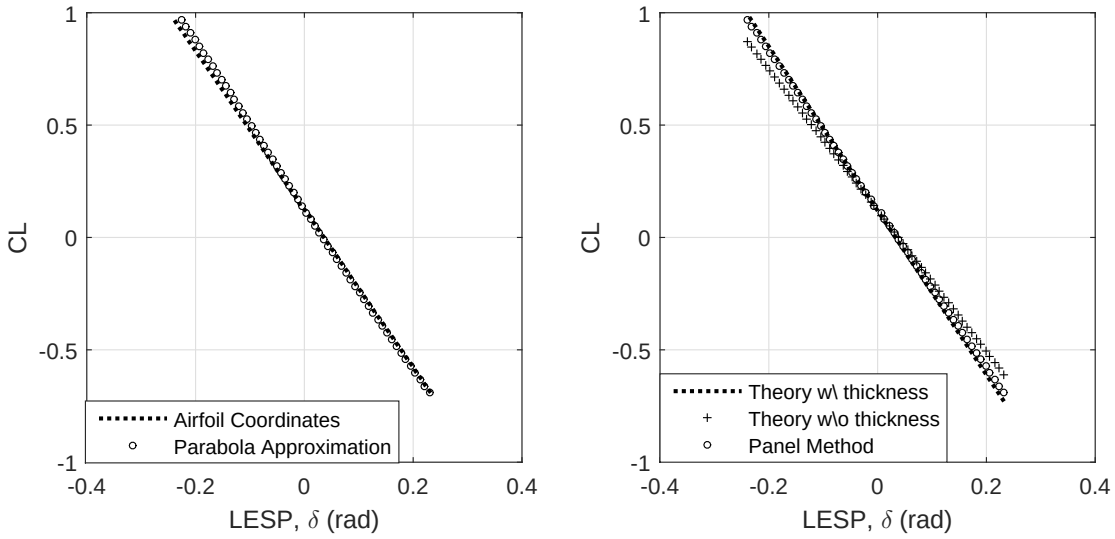

Figure 3.4: Effect of Parabola Approximation and Thickness (Inviscid Flow)

Unsteady Flow

The model that is validated for the steady flow is now evaluated for unsteady airfoil motions. Pitch and plunge harmonic motions are considered separately. We specifically investigate the influence of the rate terms. Figure 3.5 shows the time-history comparison of C_L for the pitching airfoil. The pitch axis is located at quarter-chord.

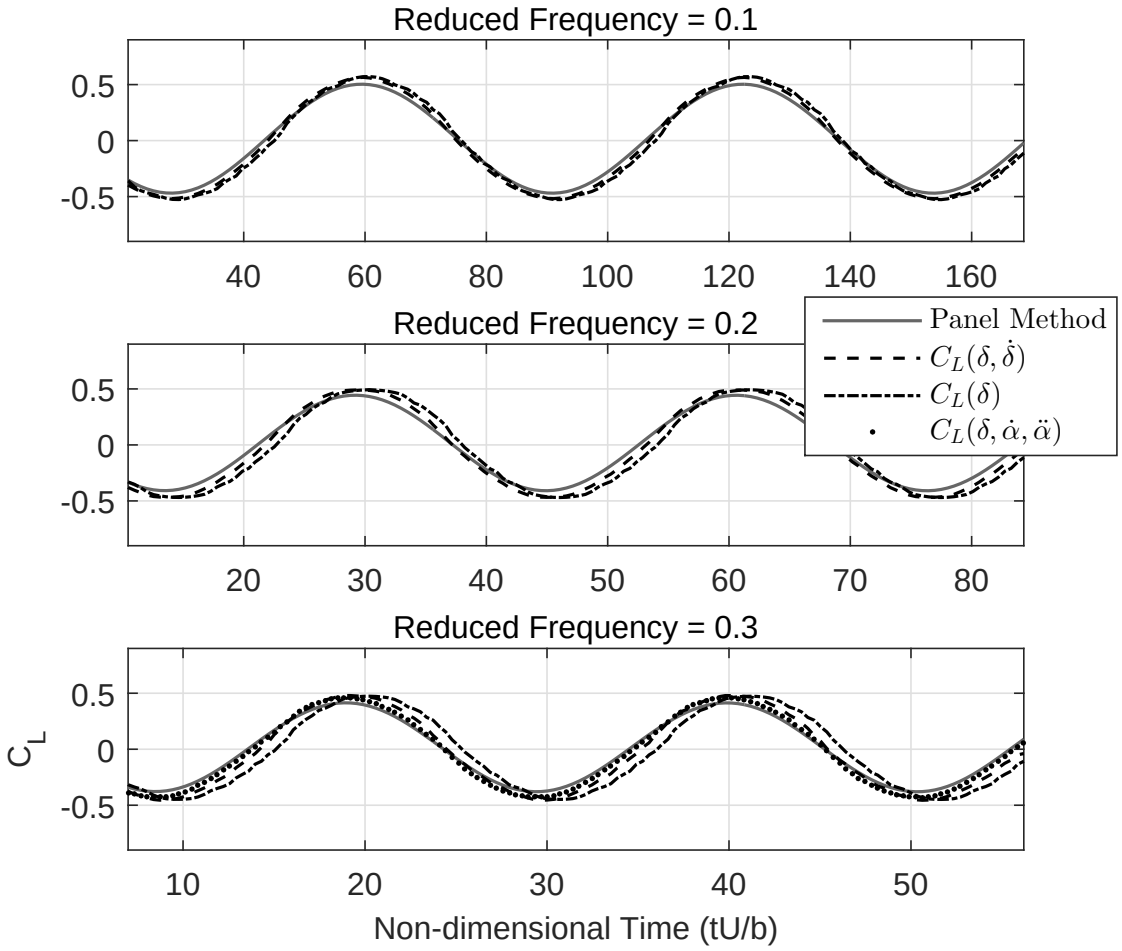

Figure 3.5: Pitch-Only Maneuver, Amplitude 5 deg

For a pitching amplitude of 5 deg, increasing reduced frequencies (0.1, 0.2, 0.3) are considered. The model with LESP-rate information included – $C_L(\delta, \dot{\delta})$ – captures the frequency-dependent phase-lead. The contribution from the phase-lead is seen to be more significant at higher reduced frequencies (compare $C_L(\delta, \dot{\delta})$ vs $C_L(\delta)$). At low reduced frequencies ($k < 0.1$), the LESP-rate contribution is negligible. At higher frequencies ($k > 0.3$), the model – $C_L(\delta, \dot{\delta})$ – reveals a small phase-lag. This is due to Eq. 3.24 losing

validity (since $C(k) \neq 1$) in addition to the increasing significance of frequency-dependent second order effects. Thus, using Eq. 3.21 along with non-circulatory contributions from $\dot{\alpha}$ and $\ddot{\alpha}$, a better comparison is found (See $C_L(\delta, \dot{\alpha}, \ddot{\alpha})$, Fig. 3.5).

Figure 3.6 shows the time-history comparison for the plunging airfoil with an amplitude of 30% chord. As discussed previously, for plunge-only maneuvers and for low-to-medium reduced frequencies, the LESP-rate information is not needed to estimate C_L. Thus, $C_L(\delta)$ compares well with the panel result for $k = 0.2$ with minor discrepancies. However, the agreement deteriorates for higher reduced frequencies due to growing significance of the apparent mass effects $\ddot{h}$. Accounting for these terms, the agreement with the panel result improves (See $C_L(\delta, \ddot{h})$, Fig. 3.6).

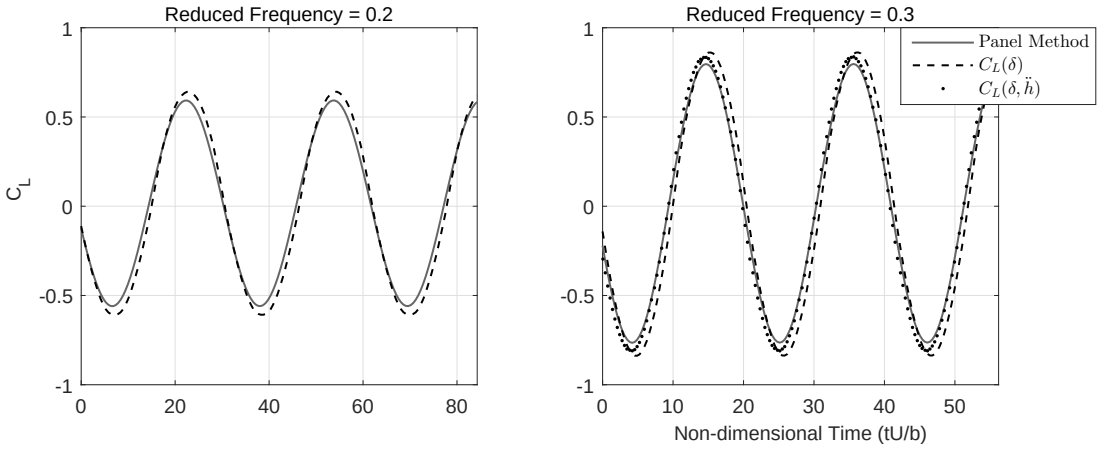

Figure 3.6: Plunge-Only Maneuver, Amplitude 30% chord

It is more practical to measure distributed flow properties such as shear stress, convective heat-transfer and pressure to determine the stagnation point in lieu of the boundary-layer edge velocity. Since the oncoming flow bifurcates at the stagnation point, we expect

surface flow quantities such as flow speed, pressure and shear stress to reach their local extremum at the stagnation point to satisfy flow symmetry. For instance, Fig. 3.7 shows negligible error in choosing maximum C_P over minimum speed. Thus, pressure-based sensors may also be used to locate the LESP. However, since the spatial gradients for surface pressures near the LESP are negligible, directly locating the LESP using pressure sensors is susceptible to calibration errors. Pressure sensors offer limited bandwidth as a result of mechanical (peizoresistive, peizoelectric) or pneumatic (pressure-taps) lags. Deconvolution techniques may be developed to recover the actual response, but this process requires considerable effort. Sensor response may also change with time and requires periodic calibration. In addition, due to the leading-edge curvature, installing flush-mounted surface pressure transducers could be problematic and using pressure ports instead leads to significant pneumatic lags.

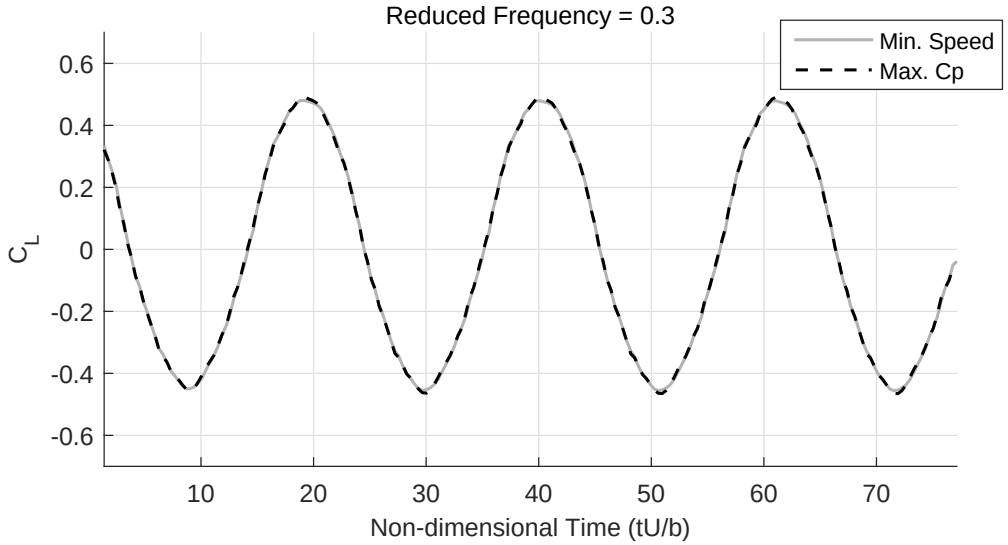

Figure 3.7: Estimating LESP using Max. C_p vs. Min. Speed

An alternative sensing strategy is the use of hot-film sensor arrays to determine the stagnation point from distributed heat-transfer measurements. Hot-film sensors are non-intrusive, compact, and, easier to install around the leading-edge. The heat-transfer distribution near the LESP shows sharp spatial gradients, and therefore, identifying the LESP is less sensitive to calibration errors. The sensor assembly does not contain diaphragms or moving parts. Accordingly, the sensor response characterized by high sensitivity over a large bandwidth is significantly faster than pressure-based systems. However, hot-film sensor arrays are fragile and susceptible to damage from adverse environmental conditions. Compensation methods to account for the hot-film substrate heat transfer may also need to be developed. In the following section, locating the leading edge stagnation point using a hot-film array is demonstrated.

3.4.2 Experimental Results

To validate the model experimentally, steady and unsteady tests were conducted at Texas A&M university's 3x4 ft. low speed wind tunnel. The test facility is equipped with a Pitch-Plunge Drive System (PPDS) and a Nonlinear Aeroelastic Test Apparatus (NATA II) (Figs. 3.8, 3.9 and 3.10). The PPDS [45] is a forced oscillation apparatus that may be used for both aerodynamic or structural dynamics calibration purposes. In addition, the apparatus serves as a gust generator. The setup is capable of oscillation frequencies in pitch and plunge upto 4 Hz. The NATA II [46] platform, modeled after NATA I [16], is capable of exhibiting limit-cycle oscillations (LCOs) of about 3 Hz at wind speeds in the range 12–14 m/s. The NATA II platform consists of a two degree of

freedom wing section that is allowed to pitch and plunge. A spring-hardening type nonlinearity designed into the torsional mode provides a stabilizing influence leading to LCOs.

The facility is useful for studying unsteady aerodynamics, nonlinear aeroelasticity and active flutter suppression. Two 4 ft. foam-core carbon-composite wings were fabricated for testing. One of the test wings instrumented with the hot-film sensor array is shown in Fig. 3.8. For the NATA II wing, the array consists of 32 sensors distributed between $\pm 0.05\%$ chord and mounted mid-span. The hot-film sensors provide real-time measurements of the power dissipated to the flow.

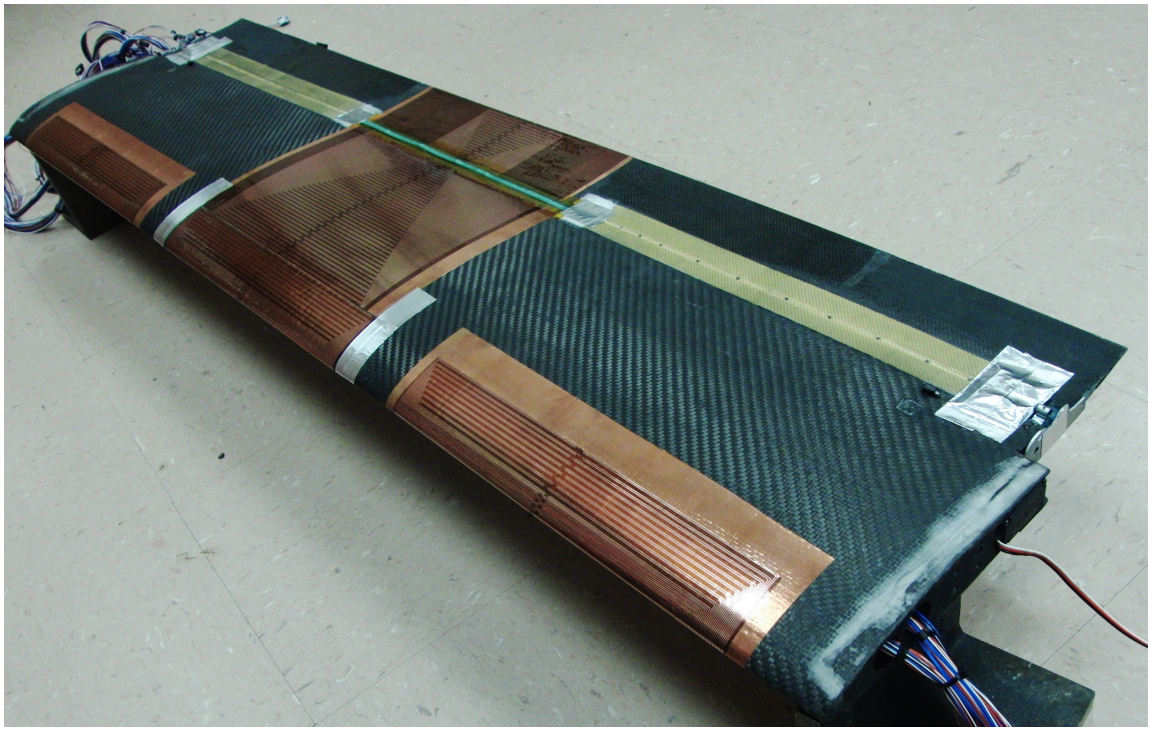

Figure 3.8: Wing Instrumented with Hot-Film Sensors

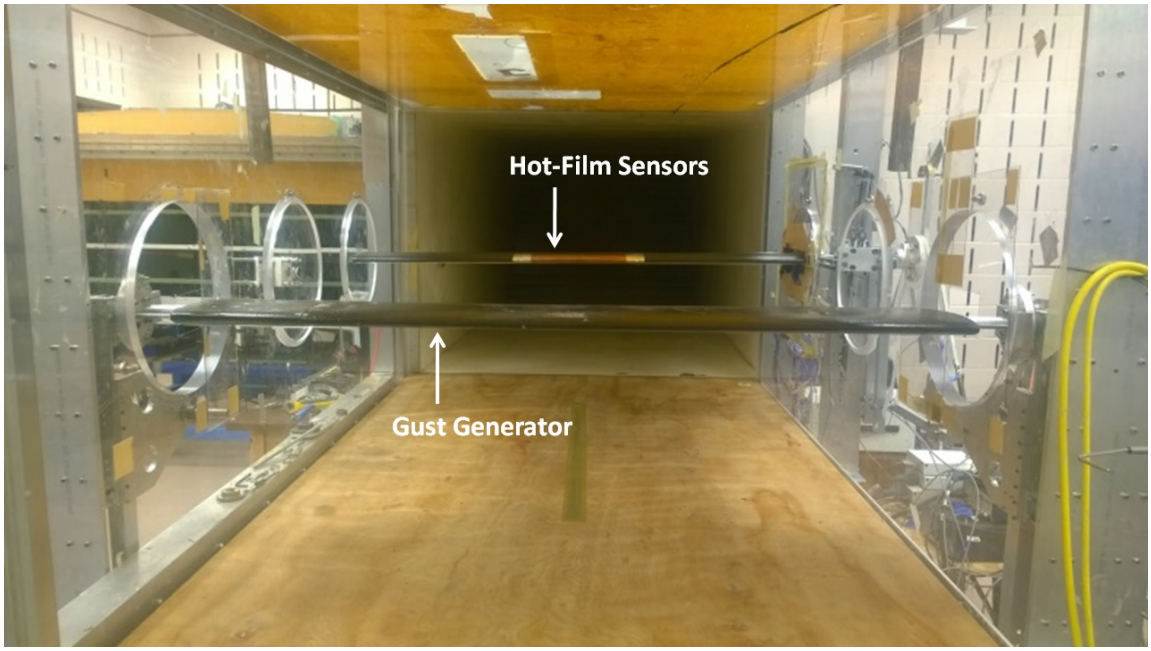

Figure 3.9: Gust Generator and NATA II, Front View

Figure 3.10: Gust Generator and NATA II, Side View

The test-bed is equipped with a variety of sensors: load sensors (ATI® Delta 6DOF), piezoelectric accelerometers, angular and position optical encoders for aerodynamic and inertial load measurements. Freestream properties (velocity, pressure and temperature) are measured by pressure and temperature transducers. A hot-wire sensor installed

approximately a chord length ahead of the wing is used to characterize the gust field impacting the NATA II wing. A full-span trailing-edge control surface is built into the wing that is actuated using a servo-motor.

The unsteady lift measurements that are used to validate the model are obtained from the load sensors. However, with the wing in motion, the load sensors measure both aerodynamic and inertial loads acting on the wing. A physics-based model for the inertial loads using accelerometer and encoder measurements is used to isolate the unsteady aerodynamic loads. Flexibility in the wing is assumed to be minor, and therefore, only rigid-body dynamics are considered. More details on the method to isolate aerodynamic loads are found in Refs. [45, 47] and in Section 4.

The stagnation point is identified from the hot-film sensor array where the convective heat-transfer is a minimum. Using unsteady boundary-layer theory [48], the shear-stress, pressure gradient, and convective heat-transfer, are related by:

$$\tau_w = k_1 Q^3 + k_2 \frac{dP}{dx} Q^{-1} + k_3 \frac{\partial Q}{\partial t} \tag{3.30}$$

where Q is the convective heat transfer rate (power dissipated to the fluid by the sensor) and P is the pressure. k_1, k_2, and k_3 are constants defined in Ref. [48]. For low reduced frequencies, $k_3 \frac{\partial Q}{\partial t}$ is negligible. At the stagnation point, $\frac{dP}{dx} \approx 0$, and thus, locating the point of minimum heat transfer locates the minimum shear stress, and therefore, the LESP. To compare sensor measurements with theory, an estimate of the theoretical Q is found

from the cube-root of the wall shear stress computed by X-Foil. The experimental and theoretical Q are normalized for every sensor to remove calibration gain and offset errors. Given data for several angles of attack, the mean is first subtracted to remove the offset. The logarithm of the modulus is then computed, following which the mean is subtracted again, to remove the gain. Figure 3.11 shows a reasonable comparison for a sample set of sensors. The minor discrepancies may be due to sensor placement measurement errors and the assumptions inherent in boundary-layer analysis.

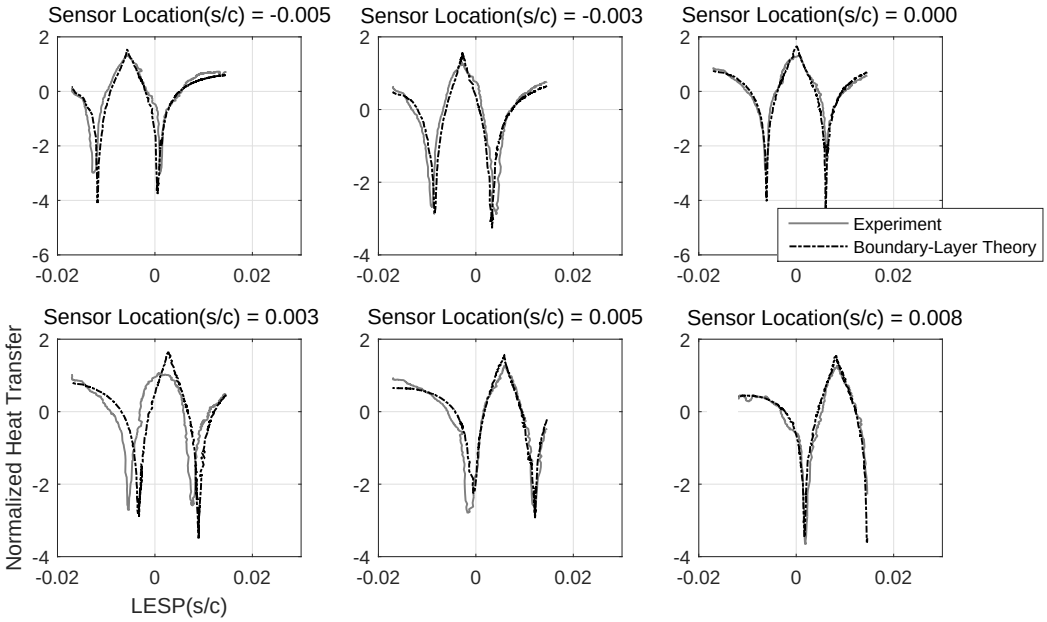

Figure 3.11: Normalized Heat Transfer vs LESP, Experiment Compared with Boundary Layer Theory

The accuracy of directly locating the LESP using the power dissipation depends on the resolution and calibration of the sensors. However, since relative measures are required to locate the minimum, the sensors need only be calibrated such that they uniformly

output the same power at zero wind-speed. Absolute sensor calibration reflecting actual convective heat-transfer measurements is not required. To provide smooth interpolation as the LESP travels between sensors, the aforementioned three-point minimum finding algorithm is used. A guess region is first determined by choosing a relatively low power region. The initial minimum that is found in this region is improved upon using the three-point interpolation method. As discussed previously, for a more accurate chord-wise LESP estimation, the leading-edge region is approximated by a parabola with a nose radius of 1.2% chord. Sensor locations are then given as surface-wise distances from the leading-edge on this parabola. It is also possible to locate the LESP using an uncalibrated low resolution array by generating a map between sensor measurements and the LESP. The map may be derived using the LESP determined from the signal minimum for individual sensors.

Several wind-tunnel tests were conducted – steady tests through various angles of attack and control surface deflections, oscillations in pitch, plunge and control surface, and the onset of gusts. Data from these tests are primarily used to validate the LESP model for these various scenarios. For the wing that is tested, the airfoil has a chord scaled to 11 inches. All other parameters remaining the same, the LESP model is now given as:

$$C_L = -3.653\delta - 0.438\frac{\dot{\delta}}{U} + 1.732\beta - 0.121\frac{\dot{\beta}}{U} + 0.12 \tag{3.31}$$

Steady Flow

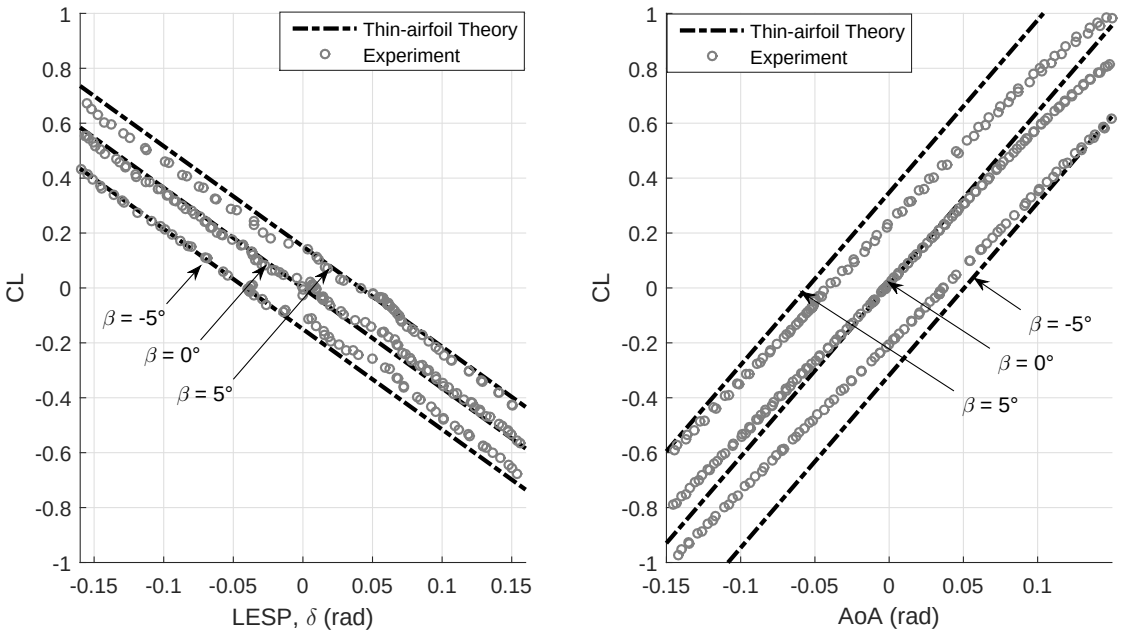

Figure 3.12: Static Tests

Figure 3.12 shows steady flow results for various angles of attack and three control surface deflections: -5, 0, 5 deg. Similar to the computational results, the agreement of the thin-airfoil theory predictions with the load sensors is significantly better for the LESP than the angle of attack. In particular, note the C_{L_δ} slope is more accurately predicted than C_{L_α}. The contribution from the control surface deflection to C_L is also more accurately predicted by the LESP. The minor discrepancies may be due to possible twisting of the control surface at high dynamic pressures. The control surface is actuated at the wing root and its rotation is measured by an encoder also mounted at the wing root. Although the computational results verified the effect of camber, the prediction for C_{L_0} had an appreciable error. The discrepancy is attributed to sensor placement errors, in particular,

the error in locating the leading edge reference and the misalignment of the control surface for $\beta = 0$. Another possible source of error is the load sensor drift.

However, due to the simplicity of the model, experimentally identifying C_{L_0} and other parameters do not involve significant difficulties. For clarity, the plots shown are corrected for this offset determined from the $\beta = 0$ case. The data was recorded at a freestream velocity of 19 m/s. The trends based on the LESP are fairly linear for this case. At lower velocities ($\approx$ 10 m/s), minor nonlinearities in the $C_L(\delta)$ curve are observed. This may be due to low Reynolds number effects such as the development of the laminar separation bubble.

Unsteady flow

Figure 3.13 shows the results for the wing in LCO undergoing oscillations in both pitch and plunge modes. The pitch axis is located at the quarter-chord position and the reduced frequency for this case is 0.2. The heat transfer plot shows the movement of the LESP (dark contour) with time. The minimum is clearly visible due to the high resolution and proper calibration of the sensors. The C_L estimate from LESP is in good agreement with that obtained from the load sensor measurements.

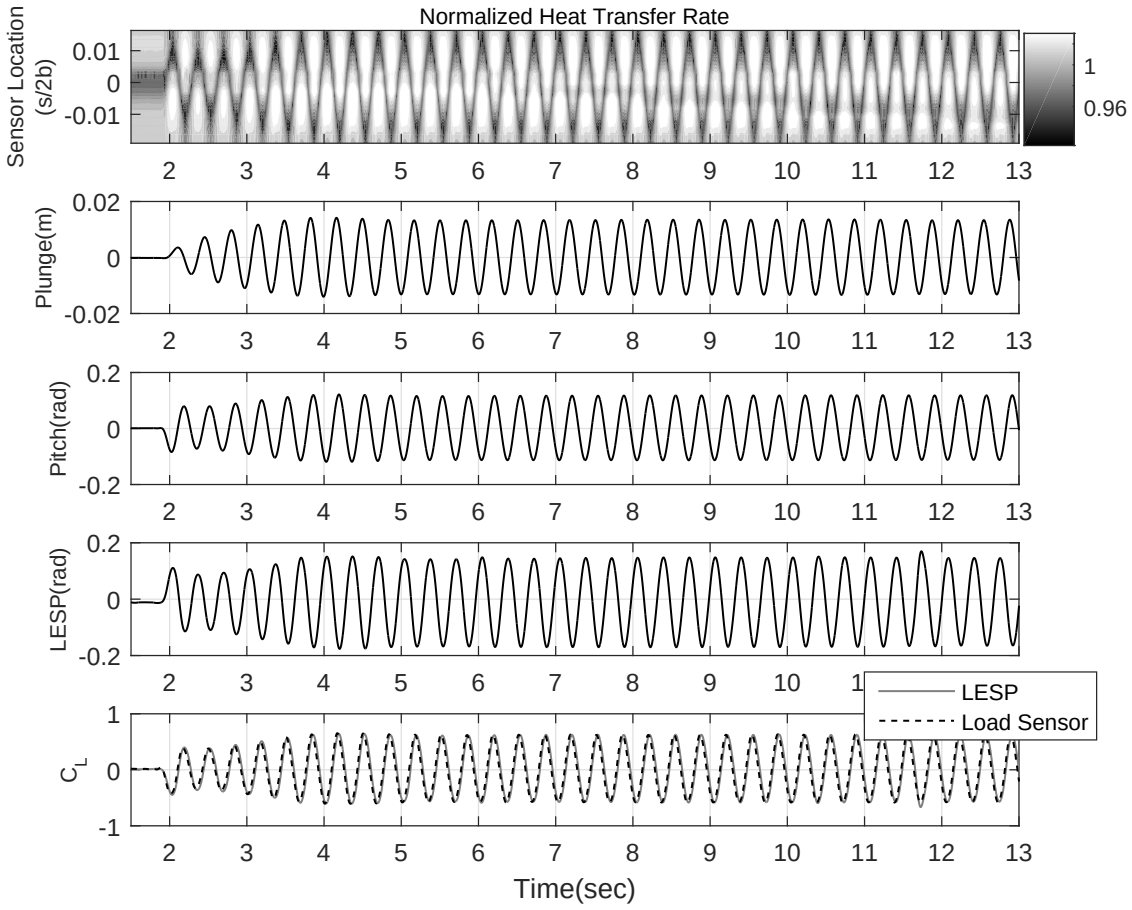

Figure 3.13: Dynamic Tests: Limit Cycle Oscillations

Figure 3.14 shows the results for a frequency sweep in the trailing edge control surface with the pitch mode locked. The wing is allowed to oscillate in the plunge mode. Again, good agreement is reached between the load sensor measurement and LESP predicted lift.

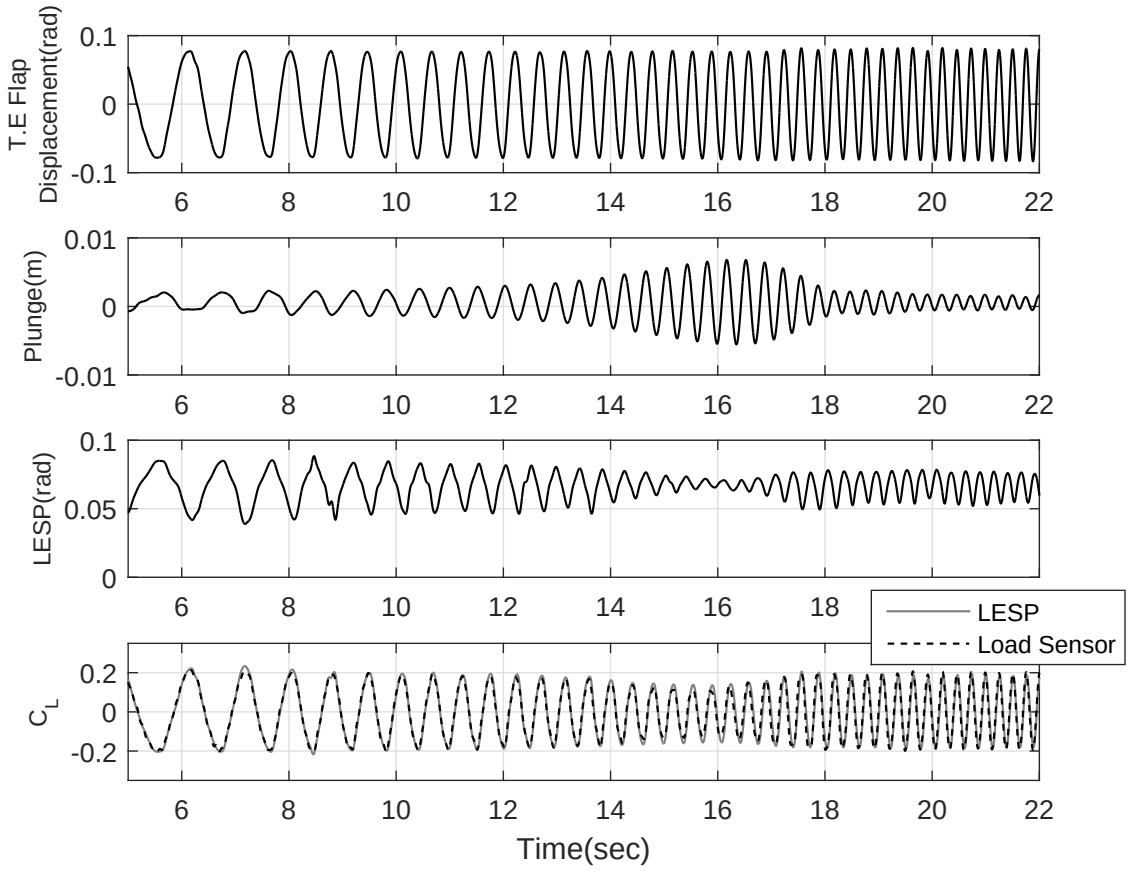

Figure 3.14: Dynamic Tests: Control Surface Oscillations

Figure 3.15 shows the model predictions for an onset of harmonic gusts. The gust wing was subject to a 4.5 deg amplitude pitch oscillation at 2.2 Hz. The gust frequency content in the test-section is known approximately using the hot-wire setup mounted ahead of the wing. Note that though minor discrepancies in amplitude are observed, the waveform is well predicted. With the wing cantilevered at the root, associated modal vibrations that are not accounted for in the load sensor measurements, introduce errors, particularly for high frequency excitations.

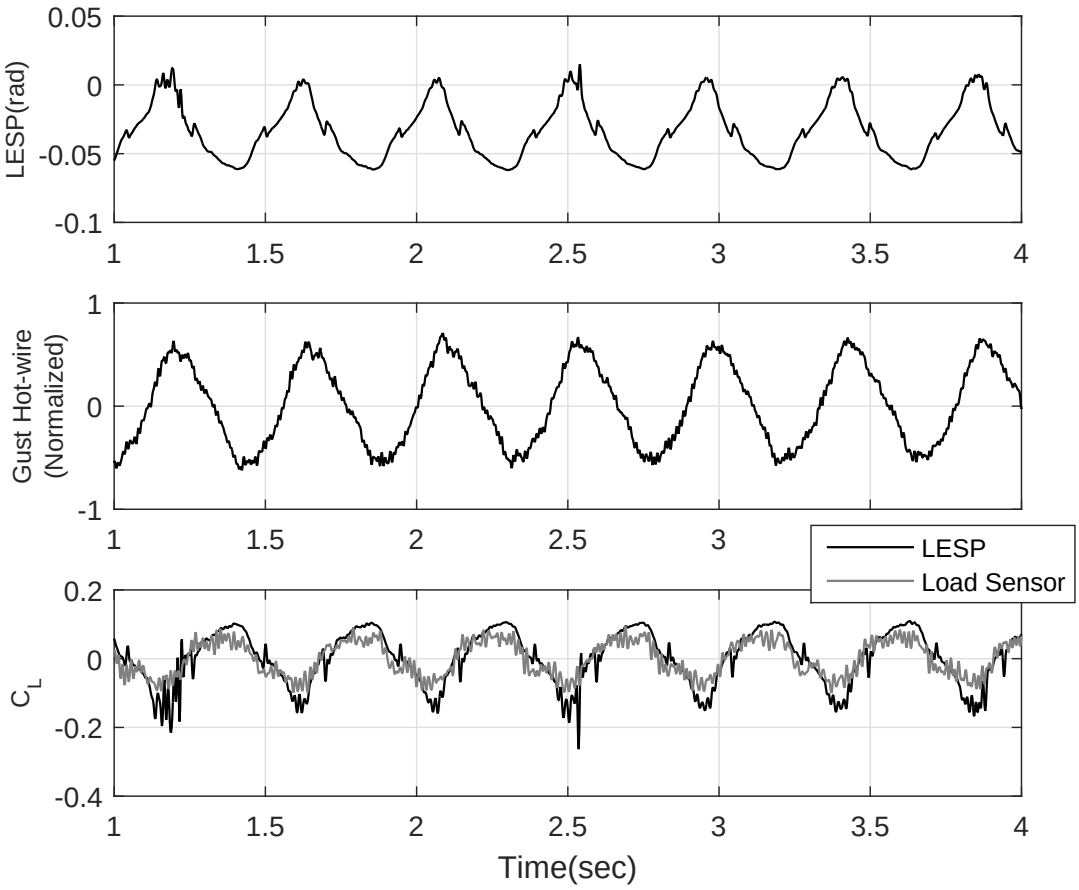

Figure 3.15: Dynamic Tests: Harmonic Gust Onset

Although not clearly visible in Figs. 3.13, 3.14 and 3.15, the C_L determined from the LESP shows a minor phase-lag with respect to the load sensor measurements. In contrast to hot-wire probes that show a first-order response, hot-film sensors have a fractional-order response associated with the substrate heat transfer [49], and, if not compensated for through deconvolution, results in a phase lag. However, in determining the LESP, as the signal minimum is required, only phase-lags as a result of signal convolution play a role; the effect of convolution in amplitude fluctuations is a relatively

insignificant influence.

For the bandwidth relevant to the NATA II apparatus, a first-order filter is found to correct the phase-lag such that:

$$C_L = C(s)f(\delta, \dot{\delta}) + g(\beta, \dot{\beta}) \tag{3.32}$$

The compensator $C(s)$ is applied only on terms containing δ and $\dot{\delta}$ and is identified from input-output ($f(\delta, \dot{\delta}) \rightarrow C_L$) experimental data. The system identification toolbox available in MATLAB® is used for this purpose. $C(s)$ also compensates for the phase-lag due to assumptions involved in using Eq. 3.24 and lags incurred in the data acquisition process such as filtering. The phase response of the identified compensator $C(s)$ is shown in Fig. 3.16. The phase lag is seen to increase with frequency reaching to about 40 deg at 3 Hz. The phase response of the compensated model $C(s)f(\delta, \dot{\delta})$ is also shown. Note that the phase-lags in this case have substantially reduced. The phase response of the compensated output is calculated from a first-order filter similar to $C(s)$ that is identified from data.

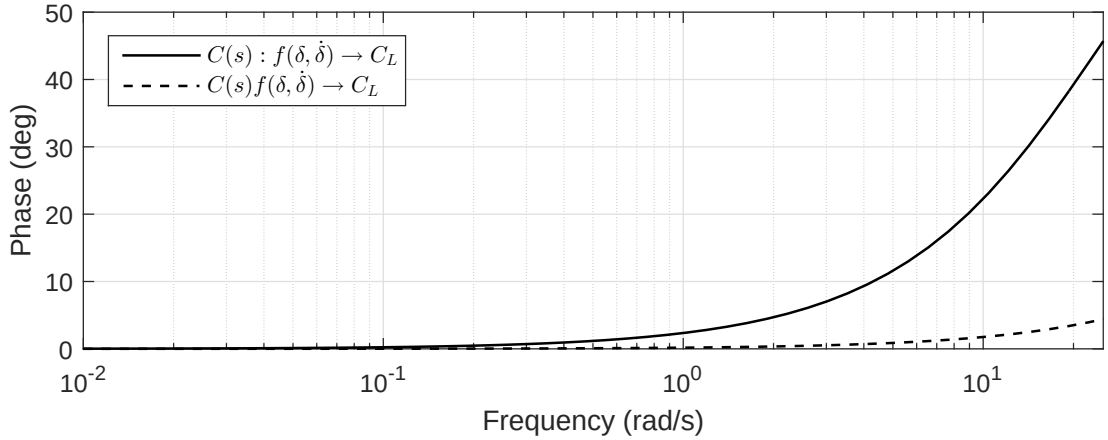

Figure 3.16: Phase Response: LESP Compensator $C(s)$

3.5 Applications

The availability of real-time aerodynamic load measurement offers several possibilities in its utility towards distributed sensing and control. An immediate application is towards stability augmentation of flexible aircraft such as the suppression of aeroelastic instabilities and gust-load alleviation. Online performance optimization by intelligently shaping the lift and drag distribution using aerodynamic-output feedback is another possibility. For high-aspect ratio wings, hot-film sensor arrays mounted along the wing leading edge may be used to provide sectional real-time aerodynamic load estimates along the span. Changes in span-wise circulation due to tip vortices and wing-fuselage aerodynamic interactions may be accounted for by tracking the span-wise LESP.

The applicability of real-time LESP measurements towards flutter suppression and gust load allevation was demonstrated using the NATA-II platform. A simple control law based on shaping C_L estimated from the LESP such that the effect of aerodynamics is always dissipative was tested. Active energy dissipation through this method facilitates simultaneous stabilization and disturbance rejection. The control formulation is inherently robust as it does not require knowledge of the underlying nonlinear structural dynamics. More details concerning the control law and its implementation are discussed in Section 5.

4 EXPERIMENTAL APPARATUS

4.1 Introduction

Several experimental facilities currently exist to study aeroelastic phenomena and unsteady aerodynamics. The Langley Transonic Dynamics Tunnel(TDT) [50] is well-known with a rich history of research programs that were significant to the progress of aeroelasticity. Recently, a forced oscillation apparatus, the Oscillating Turntable (OTT) [51] was installed at the TDT that is useful for studies involving unsteady aerodynamic phenomena due to forced oscillations. On a smaller scale, however, experimental test-beds were built to study particular aspects of aeroelastic behavior such as Limit Cycle Oscillations (LCOs). The Nonlinear Aeroelastic Test Apparatus(NATA) [14] at Texas A&M University is one such facility. The apparatus consists of a two-degree of freedom wing section that is allowed pitch and plunge motions supported by extensional springs. The NATA platform is capable of exhibiting LCOs as a result of a spring-hardening type structural nonlinearity in the pitch stiffness. Several previous studies have used the NATA platform to demonstrate active control methods to suppress LCOs [15–20] .

A similar apparatus (NATA-II) [46] modeled after the NATA was recently constructed at Texas A&M University. The NATA-II apparatus is built onto a test section (3’x4’) that is larger than its predecessor (2’x3’). Improvements over the previous NATA apparatus include a reinforced mounting structure for the wing that allows minimal

deformations in modes outside the scope of study, in particular, cantilever modes. To enable active control, the test wing has a full-span trailing-edge surface that is actuated using a servo motor. In addition, a forced oscillation apparatus was also constructed and is mounted ahead of the NATA-II. This apparatus consists of a pitch-plunge drive system (PPDS) [45] that is used to drive the wing through prescribed maneuvers. The primary purpose of this setup is to study unsteady aerodynamic loading developed due to forced motions in pitch and plunge. The PPDS is similar to the OTT but differs in the approach to measure aerodynamic loads. The OTT uses distributed pressure measurements to obtain aerodynamic loads while the PPDS primarily uses load sensors for these measurements. The PPDS is also useful as a shaker device to identify inertial properties of the test article. In addition, the forced wing also serves as a gust generator for the downstream aeroelastic apparatus. Thus, both facilities (NATA-II and PPDS) may be used in conjunction to study nonlinear aeroelastic responses and control in the presence of gusts. The test facility is equipped with a comprehensive sensor suite for real-time aerodynamic and structural dynamic measurements.

This section describes the sensor integration framework for the NATA-II–PPDS facility, methods for unsteady aerodynamic load measurement and system identification procedures. Unsteady aerodynamic loads are estimated using three sensor configurations based on load transducers, hot-film sensors and airfoil kinematics. The approach involves the use of simple physics-based models for each case. For instance, the load transducers

measure both aerodynamic and inertial loads, and therefore, a model for inertial loads based on accelerometer and encoder measurements is derived that is used to isolate the aerodynamic loads. The lift is also estimated using the LESP that is located real-time from convective heat-transfer measurements using distributed hot-film sensing techniques. A first-order potential flow model (described in Section 3) is used to estimate lift using the LESP. Methods to locate the LESP from hot-film sensor measurements are also described. Finally, the unsteady lift is also estimated based on airfoil kinematic measurements using conventional aerodynamic theories [35]. Methods for sensor model calibration and identification are described. For the purpose of cross-validation, representative test results illustrating the relevant physics are presented.

The section is organized as follows. Section 4.2 provides hardware details of the experimental setup and associated instrumentation. Section 4.3 describes system identification procedures to identify structural dynamic and aerodynamic properties. Physics-based aerodynamic load estimation models for the three sensor configurations and methods for model calibration are also discussed. Results validating the identification methods are provided in Section 4.3.3

4.2 Hardware Description

The facility consists of two wing assemblies (NATA-II and PPDS) placed in tandem at the 3'x4' low speed wind tunnel test section. The forced wing section mounted on the

PPDS is installed ahead of the test wing mounted on the NATA to simulate aeroelastic behavior in the presence of gusts. The wing is a 4 ft. foam-core carbon-composite construction with interiors designed for hot-film sensor wire management and access. Tests were conducted for wind tunnel speeds in the range 10-25 m/s ($200000 < \text{Re.No} < 500000$).

4.2.1 Nonlinear Aeroelastic Test Apparatus

The NATA is essentially an elastic support system for a cantilevered wing mounted at its root. A schematic of the NATA is shown in Fig. 4.1. The plunge and pitch modes are restrained by extensional springs. The plunge stiffness is designed to be linear. The pitch mode exhibits a spring-hardening type nonlinearity by design. This is achieved using linear extension springs mounted over a nonlinear cam. The spring-hardening nonlinearity provides a stabilizing influence and results in the system exhibiting LCOs. Slippage is avoided using a timing belt that is locked onto a complimentary groove pattern on the cam. The wing center of gravity location may be adjusted using a sliding counterweight in the chord-wise direction. The cantilevered wing is mounted on a load sensor. The back-plate of the load sensor is attached to the moving carriage using a steel shaft to minimize bending deformations. Accelerometers and encoders are mounted on the carriage to measure pitch and plunge inertial states. The setup is equipped with mechanisms to lock the wing in the pitch and plunge modes.

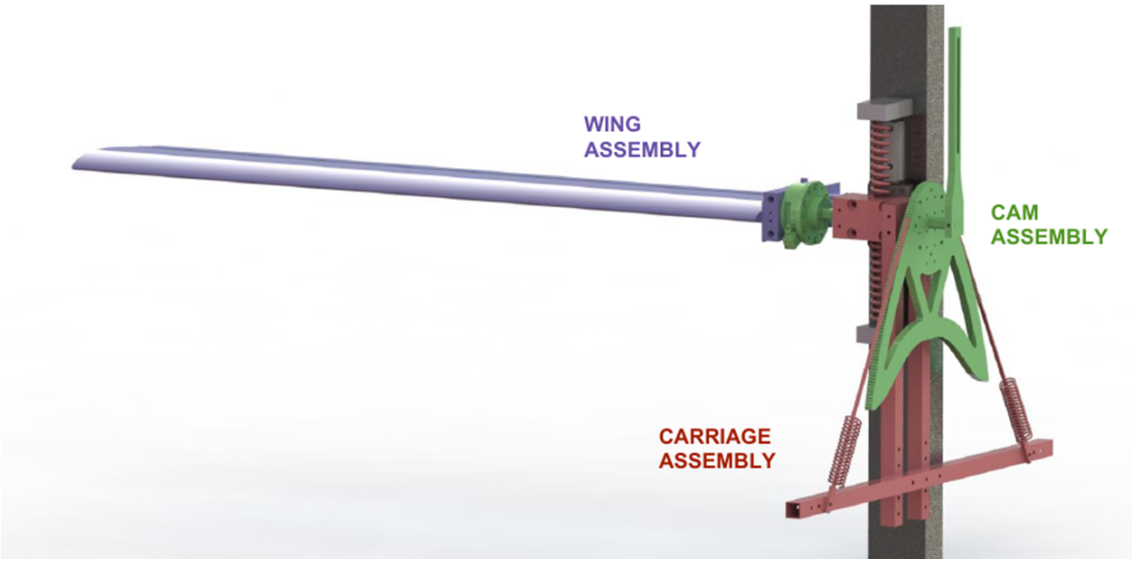

Figure 4.1: NATA-II Schematic [46]

The test wing has a chord of 11 in. and is mounted at the quarter-chord location. The wing extends through the span of the tunnel and is equipped with a full-span trailing-edge control surface for active control studies and is actuated using a servo motor mounted at the wing root. An angular optical encoder also mounted at the wing root measures the control surface deflection. The NATA is capable of exhibiting LCOs of about 3 Hz at wind speeds in the range 12–14 m/s. However, it is possible to excite the system through a range of frequencies through control surface actuation or gust excitation. System responses for wind tunnel speeds exceeding 14 m/s may be tested by stabilizing the wing using active controls. The apparatus is equipped with safety stops on both pitch and plunge modes to prevent large amplitude oscillations. The elastic and inertial parameters of the apparatus are chosen such that the LCO amplitudes are sufficiently within the stops for the desired wind-speed range. Physics-based models for the NATA have been previously developed

and validated.

4.2.2 Pitch-Plunge Drive System

The PPDS is designed for forced airfoil maneuvers in pitch and plunge. It consists of four major components – the test wing, pitch modules, the plunge mechanism and the support frame. A schematic of the PPDS is shown in Fig. 4.2. The wing is directly driven in the pitch mode by two pitch modules mounted on either end. The test wing for this setup has a chord of 12 in. and is mounted at the quarter-chord location. The wing-pitch-module assembly is then driven in the plunge mode by the plunge mechanism. The pitch module houses a servo motor that provides oscillatory pitch motion to the wing through a crank-lever mechanism. Bearings mounted within the pitch module enable smooth motions. The wing is supported on either end with load sensors that are subsequently connected to the pitch modules. Synchronous pitch motion of the pitch modules is achieved by providing synchronized commands to the servo motors on either end of the wing. The pitch modules slide on rails installed along the vertical members of the support frame. Synchronous plunge motion of the pitch modules is achieved mechanically using two identical slider crank mechanisms on either side of the support frame. The plunge motion is provided by a single 5 HP 480V 3-phase AC motor mounted below the test section. Synchronous motion in pitch and plunge is critical to avoid developing large stresses in the wing. The oscillation frequency range for both pitch and plunge actuation is 0–5 Hz. The amplitude range for the pitch mode is 2–22 deg, and for the plunge mode, 0.5–3 in. Since the pitch mode is actuated by the servo motor, a variety of maneuvers - step, frequency sweep, etc.,

are possible. The plunge actuation is currently limited to harmonic oscillations. Anticipated future efforts may address including capabilities for additional plunge maneuvers and phase-locking plunge with the pitch mode.

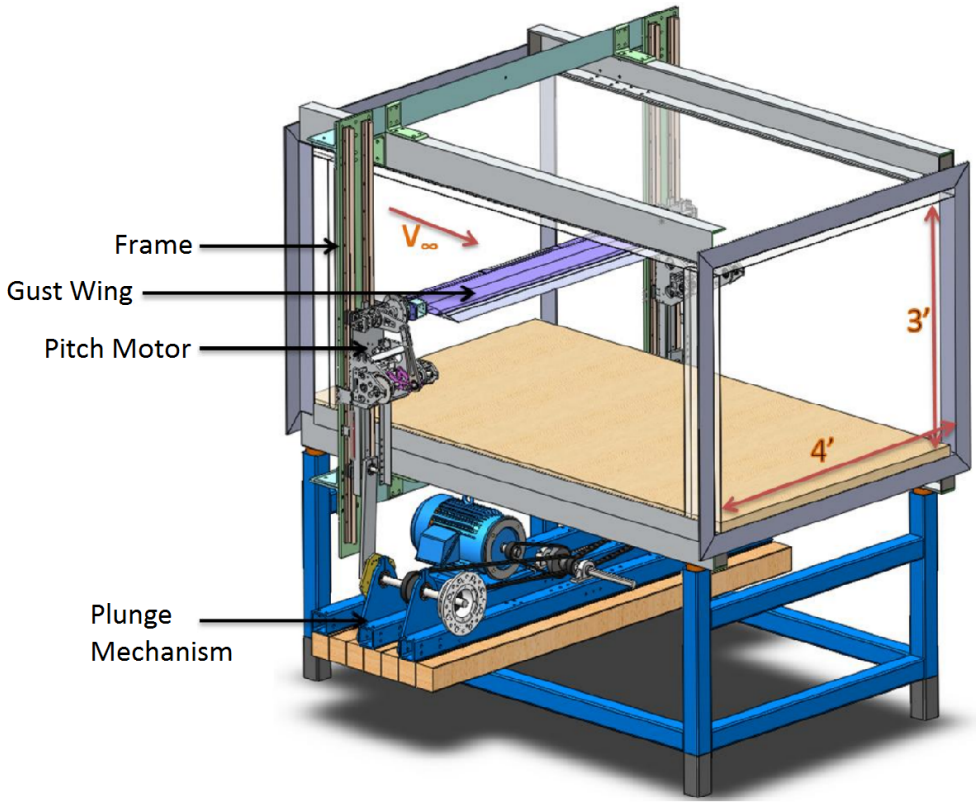

Figure 4.2: PPDS Schematic [46]

4.2.3 Sensor Suite

The test-bed is equipped with a variety of sensors configured for aerodynamic loads measurement. Loads acting on the wing are directly measured using six-component load transducer (ATI® Delta 6DOF). The device is a compact, monolithic, stainless steel structure that converts applied loads to analog strain gauge signals. The load sensors are factory-calibrated to measure forces upto 660N and moments upto 60N with a resolution of 0.125

N and 0.0075 Nm respectively. The inertial loads acting on the wing are estimated using accelerometer and encoder measurements. Piezoelectric-based single-axis accelerometers (PCB 333B40) are mounted on the apparatus to measure linear accelerations due to motion in the pitch and plunge modes. Linear and angular optical encoders are used for plunge, pitch and control surface displacement measurements. The servomotor (Savox SB2272MG) installed on the NATA-II wing operates based on the duty-cycle of an input PWM signal. The servo input command is calibrated based on the control surface encoder measurement. The test wing is instrumented with a hot-film sensor array around the leading-edge region. The hot-film sensors measure the convective heat-transfer rate to the flow. (Heat conduction to the sensor substrate is assumed to be minor.) For a high-resolution calibrated sensor array, the LESP is determined by locating the point of minimum heat-transfer. A pitot-static tube mounted far upstream along with pressure transducers is used for total and static pressure measurements. A RTD temperature sensor (Omega CNi32) is used for the freestream temperature measurement. A hot-wire probe installed midway between the gust generator and the NATA-II is used for gust characterization. Data from all sensors is acquired real-time at a 500 Hz frame rate using NI-PXI hardware. For the purpose of active controls, online data processing includes - identification of the LESP from the hot-film sensors, estimation of aerodynamic loads from force transducers, etc. The load sensors, accelerometers, hot-film sensors, pressure and temperature transducers output analog signals that are read through analog input channels. The encoders and the servomotor interface with the data acquisition system using on-board counter ports.

4.3 System Identification

The sensor suite provides aerodynamic and structural dynamic measurements that are useful for system identification. Relevant physics-based models are developed whose parameters are estimated from experimental data. The system equations are separated into structural dynamic and aerodynamic components to isolate parameters and identify prescribed maneuvers for parameter estimation. Representative results validating identification methods and assumptions on the physics are provided.

4.3.1 Structural Dynamics

In this section, relevant structural dynamic parameters: mass, inertia, stiffness and damping are identified. In addition, a servodynamics model is identified for the trailing-edge control surface. Figure 4.3 shows the schematic of the NATA apparatus without the wing. The effect of the wing (aerodynamic and inertial loads) is transmitted to the apparatus through the loads: F_x, F_y, T_z. The transmitted loads are also sensed by the load transducer. The transducer also allows the decoupling of the equations of motion for the wing and the apparatus. As shown subsequently, this separation simplifies the parameter identification process.

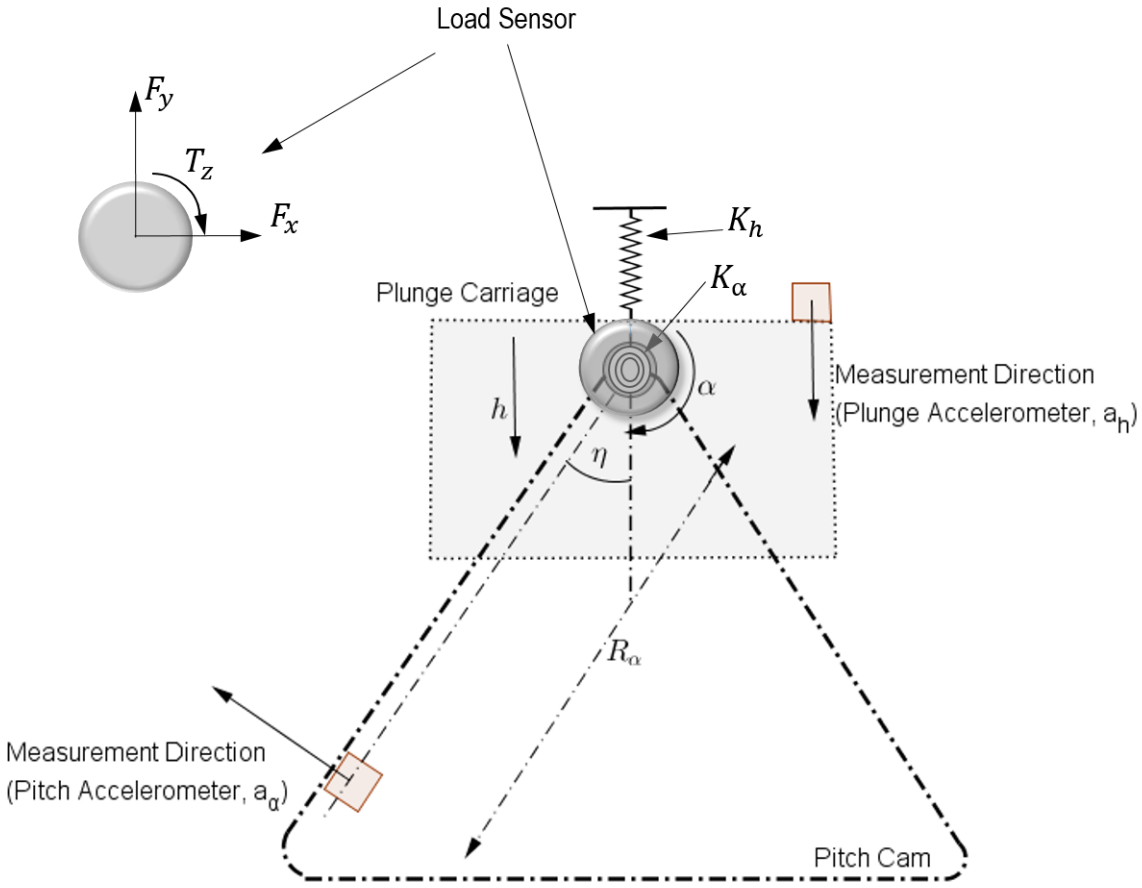

Figure 4.3: Force/Torque Transducer: Sign Conventions

The equations of motion for the apparatus (without the wing) shown in Fig. 4.3 appears as following:

$$m_a\ddot{h} + K_h h + c_h\dot{h} = -F_y \tag{4.1}$$

$$I_a\ddot{\alpha} + K_\alpha\alpha + c_\alpha\dot{\alpha} = T_z \tag{4.2}$$

Note that due to symmetry Eqs. 4.1 and 4.2 are assumed to be inertially decoupled. Viscous damping is assumed for both pitch and plunge modes. The plunge stiffness K_h is linear whereas the pitch stiffness K_α is nonlinear (built into design using the pitch cam).

Figure 4.3 also shows the accelerometer mounting locations for the NATA-II wing and associated sign conventions. The plunge accelerometer a_h directly measures the plunge acceleration. a_α mounted on the rotating cam, measures linear accelerations along its axis due to both pitch and plunge motions. However, angular accelerations of the apparatus about its pivot may be recovered by employing relevant kinematic relationships. $\ddot{\alpha}$ appears as:

$$\ddot{\alpha} = \frac{a_\theta + a_h \sin(\theta + \eta)}{R_\theta} \tag{4.3}$$

The calculated accelerations may be integrated to yield modal velocities in real-time. The integration process is a low-pass filter and thus alleviates measurement noise to some extent. The low frequency drift incurred due to measurement noise is estimated and subsequently removed using a moving average low-pass filter applied on the integrated signal. Accelerations and velocities calculated offline by numerically differentiating the encoder signals were used to validate real-time integrated estimates.

Structural Stiffness

The plunge and pitch stiffness parameters are estimated from steady tests using load transducer and encoder data. For instance, K_h is estimated from a plunge only test where loads are applied on the load transducer, i.e, using h and F_y data. Similarly, the nonlinear pitch stiffness is estimated from a pitch only steady test using α and T_z data. Data obtained from both tests are shown in Fig. 4.4.

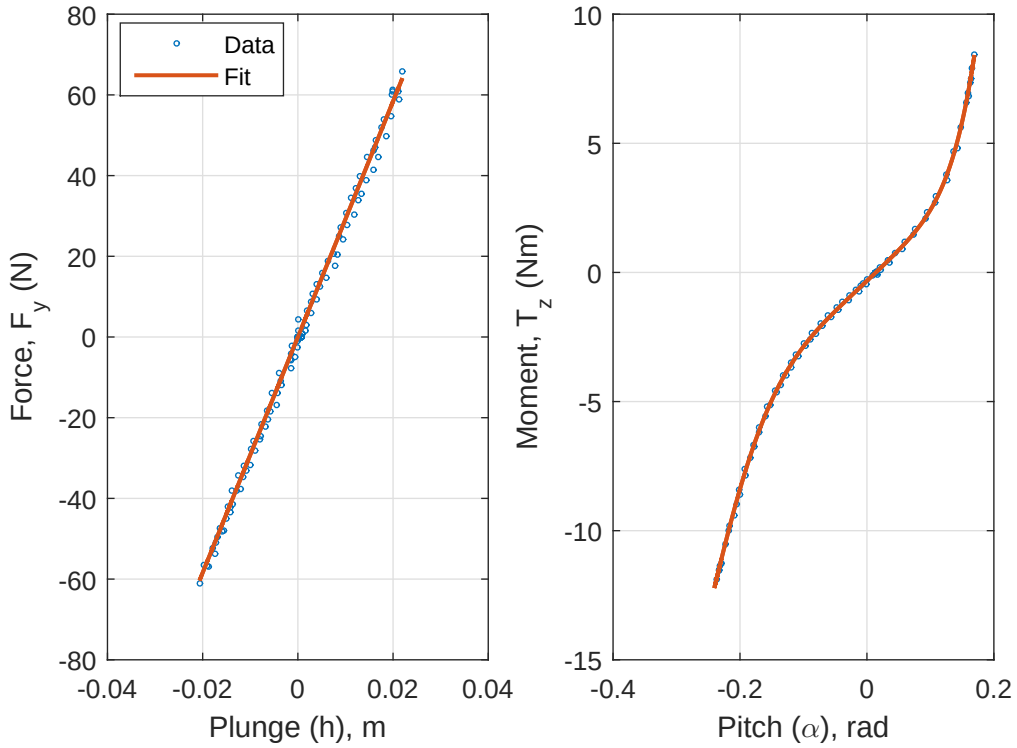

Figure 4.4: Structural Stiffness Estimation

A 6th order polynomial is used to fit the nonlinear pitch stiffness. Note that for the relevant range, the pitch stiffness is hardening. As noted in experiments, the spring-hardening feature results in the aeroelastically unstable wing settling in a limit cycle.

Apparatus Mass, Inertia and Damping

With K_h and K_α known, the apparatus mass, inertia, pitch and plunge damping are estimated from Eqs. 4.1 and 4.2 using dynamic test data. The prescribed test consists of the wing in LCO with a frequency sweep in the trailing edge control surface. The equations

then appear as:

$$m_a\ddot{h} + c_h\dot{h} = \bar{F}_y = -F_y - K_h h \tag{4.4}$$

$$I_a\ddot{\alpha} + c_\alpha\dot{\alpha} = \bar{T}_z = T_z - K_\alpha \alpha \tag{4.5}$$

Using the least-squares approach, the parameters m_a, c_h are estimated from Eq. 4.4 and parameters I_a, c_α from Eq. 4.5. The linear damping model is sufficient to capture the physics as shown in Fig. 4.5.

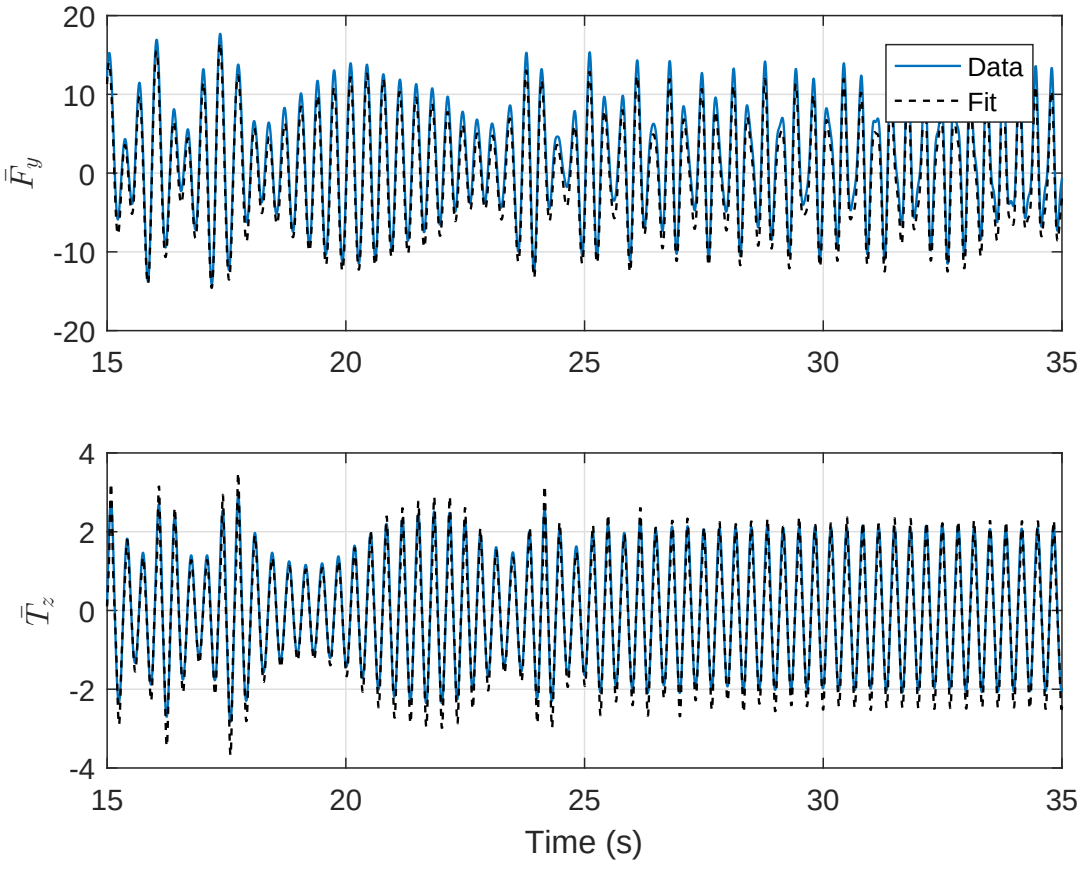

Figure 4.5: Structural Damping Estimation

Wing Mass, Inertia and Center of Gravity

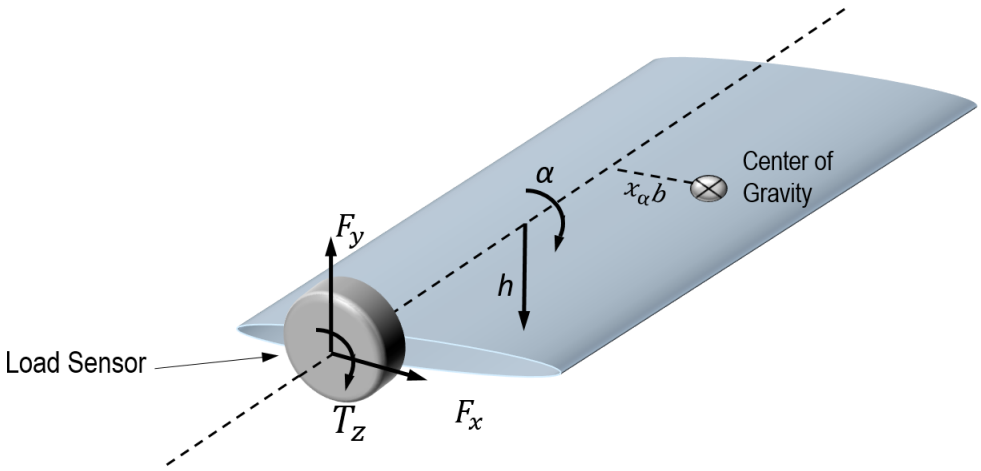

Figure 4.6: Wing Dynamics/Load Sensor Sign Conventions

The wing inertial parameters may be estimated from the equations relating the wing dynamics with the load sensor reaction forces. For a plunge only dynamic maneuver and with no wind ($U = 0$), F_y and T_z are given as:

$$F_y = m_w \ddot{h} \tag{4.6}$$

$$T_z = -m_w R_{cg} \ddot{h} \tag{4.7}$$

m_w and R_{cg} are therefore found given measured data: F_y,T_z and $\ddot{h}$. Similarly, for a no wind pitch only dynamic maneuver, we have:

$$T_z = -I_w \ddot{\alpha} \tag{4.8}$$

Figure 4.6 shows the sign conventions employed. Fig. 4.7 demonstrates the validity of Eqs. 4.6, 4.7 and 4.8.

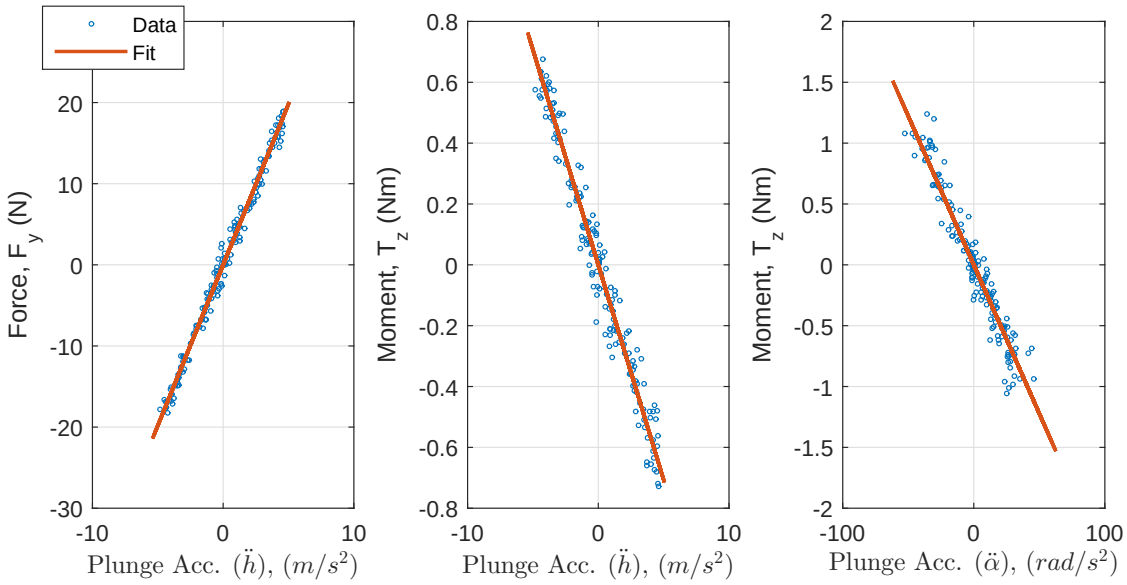

Figure 4.7: Wing Inertial Parameter Estimation

Note that the estimated inertial properties also includes contributions from sensor wires, the load sensor mounting plate and on-board sensors and actuators.

Servodynamics

A second-order model for the servodynamics is assumed relating servo command and control surface response:

$$K_{\ddot{\beta}}\ddot{\beta} + K_{\dot{\beta}}\dot{\beta} + K_{\beta}\beta = \beta_{com} \tag{4.9}$$

Note that the control surface is assumed to be inertially decoupled from the wing dynamics. The prescribed data set for identification is a control surface frequency sweep at a free-stream velocity of 10 m/s. The System Identification Toolbox in MATLAB is used for this purpose. Figure 4.8 shows that a good fit may be found using this model.

Note that the model captures both the phase lag and amplitude errors.

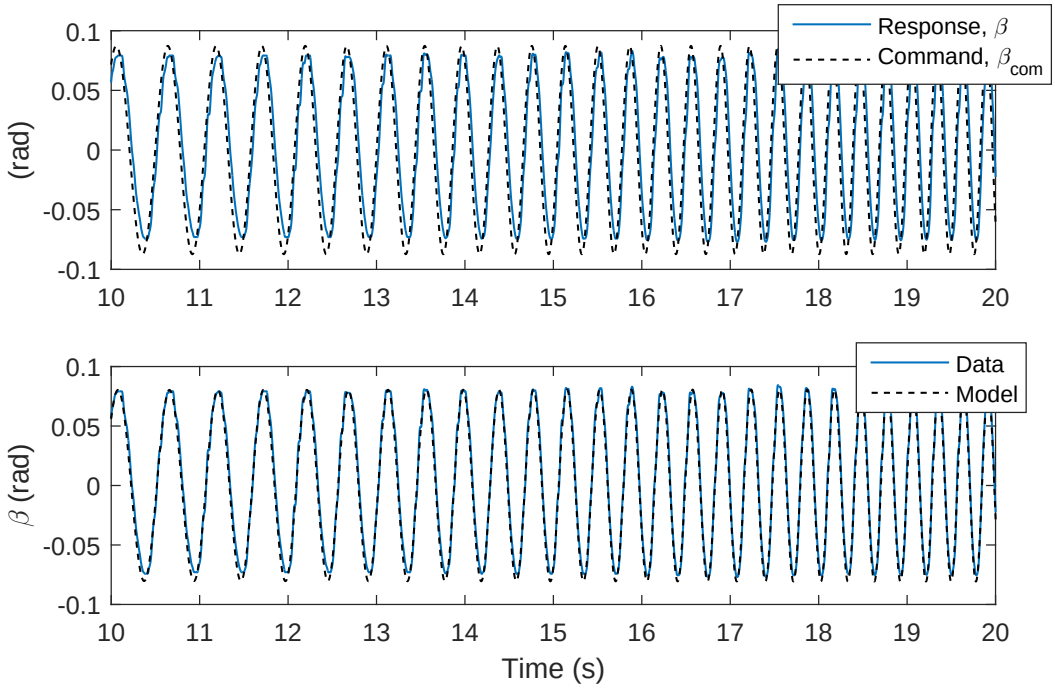

Figure 4.8: Servodynamics Identifiation

Structural Dynamic Parameters

The various identified parameters described previously are listed in Table 4.1.

Parameter	Value
m_a	7.033 Kg
I_a	0.034 $Kg.m^2$
m_w	3.963 Kg
I_w	0.024 $Kg.m^2$
R_{cg}	0.035 m
$K_{\ddot{\beta}}$	0.0002 s^2
$K_{\dot{\beta}}$	0.0198 s
K_{β}	1.0894
c_h	17.514 Kgs^{-1}
c_α	0.092 Kgm^2s^{-1}
K_h	2920.8 Nm^{-1}
K_α	$52604\alpha^5 + 19253\alpha^4 + 201.9\alpha^3$
	$133.4\alpha^2 + 2.9037\alpha + 23.2\ Nm.rad^{-1}$

Table 4.1: Identified Structural Dynamic Parameters

4.3.2 Aerodynamics

Data reduction for aerodynamic load measurement using the aforementioned sensor configurations are described. An important motivation is the opportunity to develop load-based feedback control based on real-time measurements. Towards this end, physics-based models are developed that may be used to determine the unsteady aerodynamic loads from

raw sensor data. Three sensor configurations are considered based on force transducers, hot-film and airfoil kinematics. Configurations based on force and hot-film sensors require, in addition, certain inertial measurements to estimate aerodynamic loading. Calibration methods are developed to fine-tune sensor models based on prediction error minimization techniques. Among the three sensor configurations, the load transducer measurements are considered to be the most accurate and is treated as a calibration reference.

Force/Torque Transducer

For the wing in motion, the load transducer measures aerodynamic, inertial and gravity loads. As shown in Fig. 4.9, the six-component transducer measures forces and torques along a body-fixed axes. For the NATA apparatus, inertial loads include those developed due to both rigid-body motions and wing cantilever modes. Inertial loads cannot be ignored due to the considerably heavy wings that were tested. Flexibility effects are minor, since, excitation through control surface actuation, gusts and limit cycle oscillations is limited to frequencies sufficiently below the wing bending natural frequencies. Accordingly, rigid-body assumptions are employed and were found to result in good model predictions for the inertial loads (See Sec. 4.3.3). The wing on the PPDS apparatus, however, is supported on both ends, and consequently, vibrations are negligible. The control surface mass compared with that of the wing is assumed to be relatively small, and therefore, inertial loads developed due to control surface oscillation are assumed to be negligible. Sensor wires exiting the wing also contribute negligibly to the wing inertia and are given sufficient slack to avoid transferring loads to the support structure instead of through the force transducer.

The sensor is tared after the wing has been mounted, and consequently, gravity loads arise due to the rotating measurement axes. These loads are however insignificant for small pitch angles. The estimated inertial and gravity loads are subsequently subtracted from the resultant loads measured by the load transducer to provide aerodynamic load estimates. The method is illustrated herein for the NATA-II wing and is applicable to the PPDS wing with minor modifications.

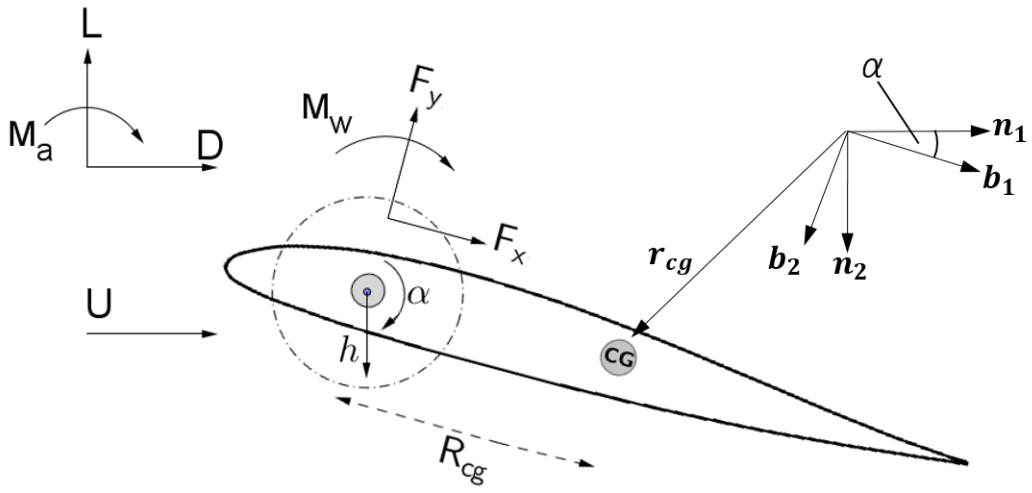

Figure 4.9: Force/Torque Transducer: Sign Conventions and Sensor Locations

To estimate the inertial loads, forces and kinematical quantities are represented in the inertial reference frame $\boldsymbol{n_1}, \boldsymbol{n_2}$ (Fig. 4.9). The linear acceleration of the center of gravity may be shown to be:

$$\ddot{\boldsymbol{r}}_{\boldsymbol{cg}} = (\ddot{h} + \ddot{\alpha} R_{cg} \cos\alpha - \dot{\alpha}^2 R_{cg} \sin\alpha)\boldsymbol{n_2} - (\ddot{\alpha} R_{cg} \sin\alpha + \dot{\alpha}^2 R_{cg} \cos\alpha)\boldsymbol{n_1} \quad (4.10)$$

The translational inertial forces ($\boldsymbol{F_I}$) then appear as (in the inertial frame) :

$$F_{I_1} = -m_w(\ddot{\alpha}R_{cg}\sin\alpha + \dot{\alpha}^2 R_{cg}\cos\alpha) \tag{4.11}$$

$$F_{I_2} = m_w(\ddot{h} + \ddot{\alpha}R_{cg}\cos\alpha - \dot{\alpha}^2 R_{cg}\sin\alpha) \tag{4.12}$$

Denoting the translational acceleration of the wing pivot by $\boldsymbol{a}_* = \ddot{h}\boldsymbol{n_2}$ and the angular momentum about the moving pitch axis by $\boldsymbol{h}_*$, the rotational inertial loads are given by ([52],Pg. 107):

$$\boldsymbol{l}_* = \dot{\boldsymbol{h}}_{\boldsymbol{cg}} + (\boldsymbol{r_{cg}} - \boldsymbol{r}_*)\times m_w(\boldsymbol{a_{cg}} - \boldsymbol{a}_*) + (\boldsymbol{r_{cg}} - \boldsymbol{r}_*)\times m_w\boldsymbol{a}_* \tag{4.13}$$

With $\dot{\boldsymbol{h}}_{\boldsymbol{cg}} = I_{cg}\ddot{\alpha}\boldsymbol{b_3}$ and $\boldsymbol{a_{cg}} - \boldsymbol{a}_* = \ddot{\alpha}R_{cg}\boldsymbol{b_2} - \dot{\alpha}^2 R_{cg}\boldsymbol{b_1}$, we have:

$$\boldsymbol{l}_*.\boldsymbol{b_3} = M_I = I_w\ddot{\alpha} + m_w R_{cg}\ddot{h}\cos\alpha \tag{4.14}$$

where $I_w = I_{cg} + m_w R_{cg}^2$. M_I is the rotational inertial load in the $\boldsymbol{b_3}$ direction.

The Newton-Euler formulation is then employed to relate the three groups of external loads acting on the wing: aerodynamic, gravity and the load transducer reactions with inertial loads. Consider the condition where the load transducer has been biased after the wing has been mounted at $\alpha = 0$. In the aerodynamic frame the load transducer forces are transformed as (See Fig. 4.9):

$$\begin{bmatrix} F'_x \\ F'_y \end{bmatrix} = \begin{bmatrix} \cos\alpha & \sin\alpha \\ -\sin\alpha & \cos\alpha \end{bmatrix} \begin{bmatrix} F_x \\ F_y - W \end{bmatrix} \tag{4.15}$$

$$M_w' = M_w + R_{cg}W \tag{4.16}$$

where W is the weight of the wing. F_x, F_y and M_w are the biased loads expressed in the rotating body-fixed frame $\boldsymbol{b_1}, \boldsymbol{b_2}$. The biased and unbiased loads ($\bar{F}_x, \bar{F}_y$ and $\bar{M}_w$) are related through:

$$F_x = \bar{F}_x \tag{4.17}$$

$$F_y = \bar{F}_y + W \tag{4.18}$$

$$M_w = \bar{M}_w - R_{cg}W \tag{4.19}$$

The resultant loads and the inertial loads, in the aerodynamic frame, are related through:

$$F_{I_1} = -F_x' + D \tag{4.20}$$

$$-F_{I_2} = -F_y' + L - W \tag{4.21}$$

$$M_I = -M_w' + M_a + R_{cg}W\cos\alpha \tag{4.22}$$

Substituting for F_{I_1}, F_{I_2}, we have for the aerodynamic loads:

$$D = F_x' - m_w(\ddot{\alpha}R_{cg}\sin\alpha + \dot{\alpha}^2 R_{cg}\cos\alpha) \tag{4.23}$$

$$L = F_y' + W - m_w(\ddot{h} + \ddot{\alpha}R_{cg}\cos\alpha - \dot{\alpha}^2 R_{cg}\sin\alpha) \tag{4.24}$$

$$M_a = M_w' - R_{cg}W\cos\alpha + I_w\ddot{\alpha} + m_w R_{cg}\ddot{h}\cos\alpha \tag{4.25}$$

Substituting for F_x' and F_y', we have:

$$\begin{bmatrix} D \\ L \end{bmatrix} = \begin{bmatrix} \cos\alpha & \sin\alpha \\ -\sin\alpha & \cos\alpha \end{bmatrix} \begin{bmatrix} F_x \\ F_y - W \end{bmatrix} - m_w R_{cg} \begin{bmatrix} \cos\alpha & \sin\alpha \\ -\sin\alpha & \cos\alpha \end{bmatrix} \begin{bmatrix} \dot{\alpha}^2 \\ \ddot{\alpha} \end{bmatrix} + \begin{bmatrix} 0 \\ m_w(g - \ddot{h}) \end{bmatrix} \quad (4.26)$$

$$M_a = M_w + R_{cg} W(1-\cos\alpha) + I_w \ddot{\alpha} + m_w R_{cg} \ddot{h} \cos\alpha \quad (4.27)$$

The non-dimensional coefficients – C_L, C_D and C_M – are obtained using the measured freestream dynamic pressure.

Hot-Film Array

The hot-film sensor array provides distributed convective heat-transfer measurements around the leading-edge from which the LESP is subsequently determined. As shown in Section 3, the unsteady lift coefficient for the airfoil section may be estimated from the LESP. The hot-film sensor array is non-intrusive, compact and is easily installed around the airfoil leading-edge. The equations are listed here again along with the C_M estimate:

$$C_L = -(1+\tau)\pi\delta - \frac{\pi b}{U}\dot{\delta} + 2\sqrt{1-c^2}\beta - \frac{2bc\sqrt{1-c^2}}{U}\dot{\beta} \quad (4.28)$$

$$C_{M_{1/4}} = \frac{\pi b}{4U}\dot{\delta} - \frac{T_4 + T_{10}}{2}\beta + \frac{b}{2U}\left[\cos^{-1} c - T_1 + T_8 + (c+0.5)T_4 - \frac{T_{11}}{2}\right]\dot{\beta} \quad (4.29)$$

The constants $T_1, T_4, T_8, T_{10}, T_{11}$ are defined in Ref. [35]. It is also possible to

determine the LESP for a low resolution sensor array with uncalibrated sensors using data reduction techniques. For low reduced frequencies, the heat-transfer distribution may be assumed to depend primarily only on the LESP, i.e., for sensor 'i':

$$Q_i = h_i(\delta) \tag{4.30}$$

where Q_i is the convective heat transfer for sensor i. h_i is a nonlinear relationship linking the heat transfer distribution with the stagnation point. With h_i identified, δ may be recovered using h_i^{-1}. To identify h_i, the high-dimensional data may be reduced to a one-dimensional nonlinear manifold. The manifold may be learned from data using techniques such as Nonlinear Principal Component Analysis (NLPCA) [53]. The method constitutes the use of an auto-associative artificial neural network (ANN) with a single-neuron bottleneck hidden layer. The network is trained to perform an identity mapping so as to reproduce the inputs at the output layer. For a successful training episode, the bottleneck layer contains the nonlinear principal component which is a compressed one-dimensional representation of the data. To employ this technique, the LESP is first located manually by analyzing individual sensor data and determining the local minimum from steady flow experiments for various angles of attack. A monotonic relationship is then sought between the nonlinear principal component identified using the NLPCA method and the previously located LESP. This relationship which may be fit to a polynomial is then used to estimate the LESP for an out-of-sample principal component. Note that only sensors in the vicinity of the stagnation point will show a strong correlation with δ. Accordingly, this process is conducted separately for pressure and suction side collection of sensors since the LESP

strongly influences only the side where it is present. The sensor collection is selected based on an approximate estimate of the LESP, for instance, using $\delta = -2\alpha$. The Q_is for a particular sensor collection are normalized such that the same minimum value is reached when the stagnation point is coincident with sensor i. The training is considered successful, if the identified map is able to reproduce the input data at the output layer with reasonable accuracy and if a monotonic relationship exists between the principal component and the LESP. The map h_i identified from static data is assumed to approximately hold true for dynamic conditions. Since the NLPCA method extracts essential features from the data, better out-of-sample behavior may be expected compared to directly identifying h_i^{-1} using a conventional ANN framework. The NLPCA toolbox [54] for MATLAB is utilized to automate the training process.

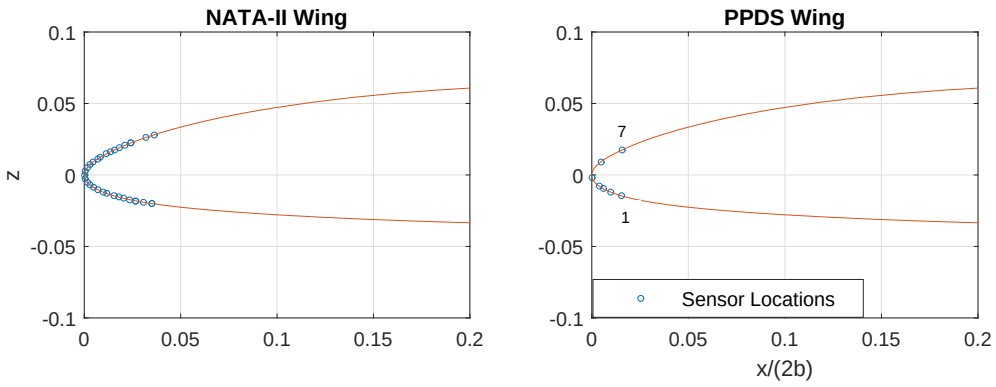

Figure 4.10: Sensor Locations

Figure 4.10 shows the hot-film sensor locations on the PPDS and the NATA-II wing. The sensor array on the NATA-II wing is calibrated and of high density, and thus, the LESP is directly located by determining the minimum heat-transfer location. The PPDS wing, however, has a relatively sparse distribution. The sensors are also uncalibrated,

and therefore, the LESP is located using the NLPCA technique. Sensors 1-5 (numbered clockwise) are considered to be on the pressure side and sensors 5-7, on the suction side.

Kinematics

Aerodynamic loads are also estimated using accelerometer and encoder measurements based on the thin-airfoil unsteady aerodynamic theory [35]. Since arbitrary airfoil motions are considered, the rational function approximation to Theodorsen's circulation function derived by Jones [55] is used. The reduced frequencies encountered in this setup are low enough ($k \leq 0.2$) to ignore apparent mass effects, and therefore, acceleration terms are not included. The time is non-dimensionalized using $\bar{t} = \frac{tU}{b}$. The plunge displacement is normalized using the airfoil semichord, $\xi = \frac{h}{b}$. The unsteady lift coefficient including circulatory and non-circulatory effects is then given by (moments are given in Ref. [35]):

$$C_L = \pi\alpha' + K_1\beta' + C(\bar{s})\left[C_{L_\alpha}\alpha + 2\pi\left(\xi' + (0.5-a)\alpha'\right) + C_{L_\beta}\beta + K_2\beta'\right] \quad (4.31)$$

where the circulation function in terms of the non-dimensional laplace variable $\bar{s}$ is:

$$C(\bar{s}) = \frac{0.5\bar{s}^2 + 0.2808\bar{s} + 0.01365}{\bar{s}^2 + 0.3455\bar{s} + 0.01365} \quad (4.32)$$

and $K_1 = -(c\sqrt{1-c^2} - \cos^{-1}c)$ and $K_2 = (1-2c)\cos^{-1}c + (2-c)\sqrt{1-c^2}$. The sign conventions follow Ref. [35]. To account for viscous effects, a, C_{L_α} and C_{L_β} estimated from steady test data are used instead of flat-plate coefficients.

Eq. 4.31 may be cast in state-space form with C_L as the output with the input defined by $u = [\alpha, \alpha', \xi', \beta, \beta']$. Two states representing the aerodynamic lag are required for $C(\bar{s})$. The resulting form results in proper transfer function representations for all inputs.

The state-space formulation is useful for integration with a state-space representation of a structural dynamics model to simulate aeroelastic behavior and for control system design. Although the steady-state coefficients have been corrected, the coefficients for the rate terms and the circulation function are derived from thin-airfoil theory, and consequently, are subject to associated assumptions such as inviscid flow, planar wake, etc. To account for these effects, a parameterized model may be identified from experimental data using ERA/OKID methods as developed by Brunton et al [37]. These methods, however, require high-frequency maneuvers to fully identify the dynamics. Herein, a simple non-parametric approach is pursued wherein the coefficients of Eq. 4.31 are refined based on experimental data by minimizing the error between model predictions and measurements for C_L. A linear grey-box model is constructed and its coefficients are estimated using the System Identification Toolbox [56] in MATLAB. The training data set consists of unsteady experiments involving motion in the pitch, plunge and control surface modes through the frequency range relevant to the test-setup. The optimization is constrained with a 20% variation allowed on the model coefficients. In addition, the constraint $C(0) = 1$ is enforced to retain the validity of the steady-state coefficients. These bounds were found to result in good model predictions while minimally affecting the frequency response, thus retaining the essential physics for out-of-sample data. Non-dimensionalization removes the velocity dependence, and thus, simplifies the identification process.

The identified aerodynamic model (along with moments) is listed as follows:

$$C_L = 3.77\alpha' + 0.49\beta' + C(\bar{s})\left[5.74\alpha + 7.42\xi' + 6.12\alpha' + 2.37\beta + 1.07\beta'\right] \quad (4.33)$$

$$C_M = -1.70\alpha' - 0.47\beta - 0.42\beta' + 0.025C_L, C(\bar{s}) = \frac{0.6\bar{s}^2 + 0.337\bar{s} + 0.0164}{\bar{s}^2 + 0.4146\bar{s} + 0.0164} \quad (4.34)$$

It should be noted that models based on inertial measurements indirectly infer the aerodynamic loads from the structural response. Accordingly, determining gust loads may be difficult, since the structure is essentially a low-pass filter. However, this task is considerably simplified when using real-time aerodynamic observables such as the LESP that can directly account for gusts as demonstrated in Section 3.

4.3.3 Representative Results

A representative set of results obtained using the test facility and the sensor framework are discussed to illustrate potential research applications in unsteady aerodynamics and aeroservoelasticity. Aerodynamic parameters identified from experimental data are also provided. The aerodynamic load estimates from the three sensor systems described previously are compared for various test scenarios – steady flows, forced oscillations, limit cycle oscillations, gusts, dynamic stall, etc. In general, good agreement is found between the three sensor configurations recognizing that the physics involved in each case for loads estimation is quite different. This serves as a "validation" for the sensor framework and the methods employed to estimate aerodynamic loads. Minor discrepancies are shown to be accounted for using simple calibration methods discussed previously.

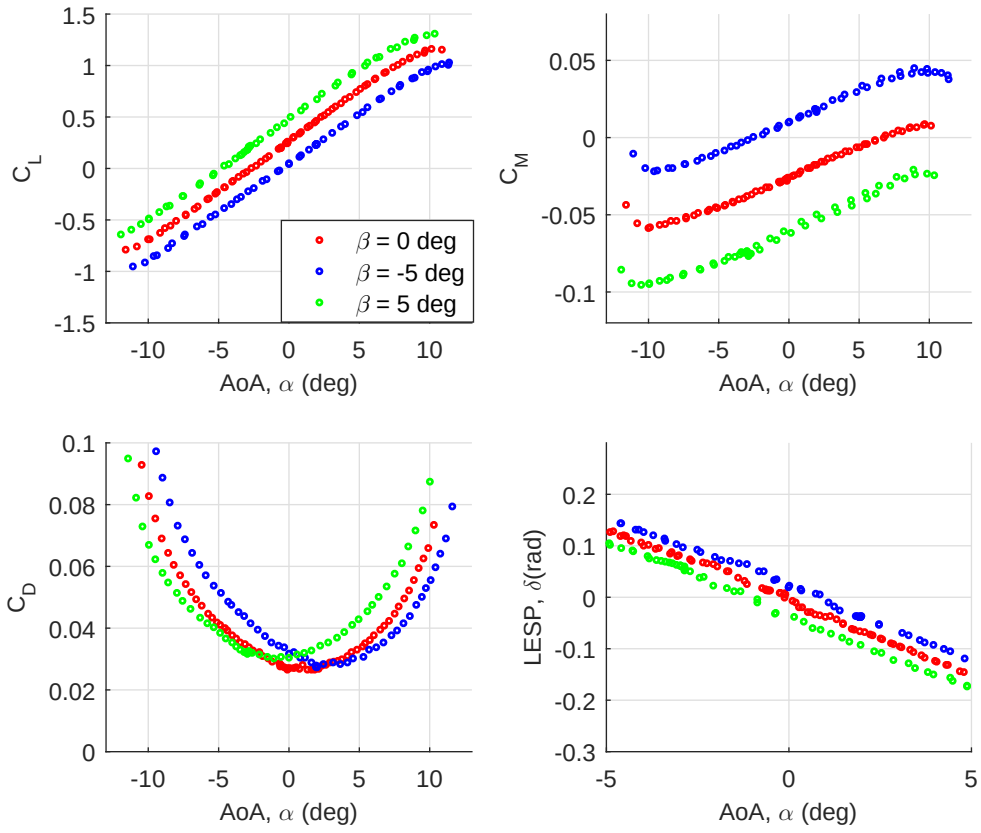

Figure 4.11: Steady tests - Sweep through Various Angles of Attack

Figure. 4.11 shows test results for the steady flow over the NATA-II wing at a freestream velocity of 19 m/s. The thickness and camber profiles for the NATA-II airfoil section are found in Section 3. The PPDS wing has a similar airfoil profile and steady-state results are provided herein only for the NATA-II wing. The aerodynamic quantities of interest – C_L, C_D, C_M and δ – over several angles of attack and control surface displacements, $\beta = -5, 0, 5$ deg are shown. As expected from thin-airfoil theory, for small angles of attack, linear trends are observed for C_L, C_M and δ. However, for the δ curve, minor nonlinearities are observed near the zero angle of attack. The effect of

	C_{L_α}	C_{L_β}	C_{M_α}	C_{M_β}	δ_α	δ_β
Experiment	5.74	2.37	0.14	-0.4	-1.59	-0.29
Theory	6.28	3.82	0	-0.65	-1.72	-0.57

Table 4.2: NATA-II Aerodynamic Derivatives

control surface displacement on C_L, C_M and δ is also linearly related as observed from the approximately equally displaced curves from the $\beta = 0$ deg case. A typical drag bucket is observed for the C_D trends with respect to the angle of attack. The minimum drag angle of attack increases with decreasing control surface angles although the behavior in this case is seen to be nonlinear. For the δ curve, the angle of attack shown is limited to small angles, since, near stall angles, the minimum in the heat-transfer distribution is relatively much less conspicuous, resulting in less reliable LESP estimates. Anticipated future work will address the estimation of the LESP for large angles of attack.

Aerodynamic derivatives with respect to the angle of attack, the LESP and control surface displacement are shown in Table 4.2. Averaged results are computed from three freestream velocities - 10, 14 and 19 m/s. Theoretical estimates are compared with experimentally determined values. The steady-state coefficients of the LESP model (Eqs. 4.28, 4.29) are shown in Table 4.3. The theoretical estimate for the δ derivatives are obtained from Eq. 4.28 and Eq. 4.31 with steady-state assumptions. The coefficients for Eq. 4.31 obtained from theory are found in Ref. [35]. The discrepancies that are noted may be due to wind-tunnel blockage effects, viscous effects, deformation in the wing and control surface twist. In particular, relatively large errors in the β derivative are observed.

	C_{L_δ}	C_{L_β}	C_{M_δ}	C_{M_β}
Experiment	-3.57	1.34	-0.1	-0.43
Theory	-3.65	1.73	0	-0.64

Table 4.3: LESP Model Derivatives

This may be attributed to significant twist deformation in the control surface at high dynamic pressures since the control surface is actuated only from the wing root. It is also known that small disturbance theories are not very successful in predicting aerodynamic loads due to control surface action [1]. This is due to the control surface operating in thick-boundary layers and also due to the effects of flow separation. The theory more accurately predicts the slope with respect to the LESP (C_{L_δ}) rather than with the angle of attack (C_{L_α}). This is due to the inherent capability of the LESP to partially account for changes in circulation due to viscous effects, illustrating the potential use of the LESP as a real-time aerodynamic observable. Similarly, other contributions to changes in the circulation such as three-dimensional finite-span effects, wing-fuselage interactions, etc., may also be captured to some extent.

The dynamic test results are discussed next. Loads and displacements are shown as deviations from the equilibrium. To validate the method of estimating unsteady aerodynamic loads using the force transducer measurements (Eqs. 4.26, 4.27), the accuracy of the inertial loads model is first evaluated. For a wind-off test, assuming the aerodynamic forces are negligible, the force transducer measurements are primarily inertial loads developed in the wing as a result of wing motion. The inertial loads model is then validated

for a random maneuver in plunge and pitch along with a frequency sweep in the control surface at zero wind speed. Figure 4.12 shows good agreement between predictions and measurements for the normal force and moment. Minor discrepancies are observed for the relatively rapid portions of the maneuver. This may be due to the result of neglecting contributions from the wing cantilever mode and aerodynamic apparent mass effects. The model predictions for the edge-wise inertial forces that are not shown were insignificant ($\approx$ 1N). The rigid-body model predictions did not agree with measurements, since, the relatively high-frequency edge-wise cantilevering loads that are not modeled, dominated the response. This is not an issue for the PPDS wing since it is supported on both ends.

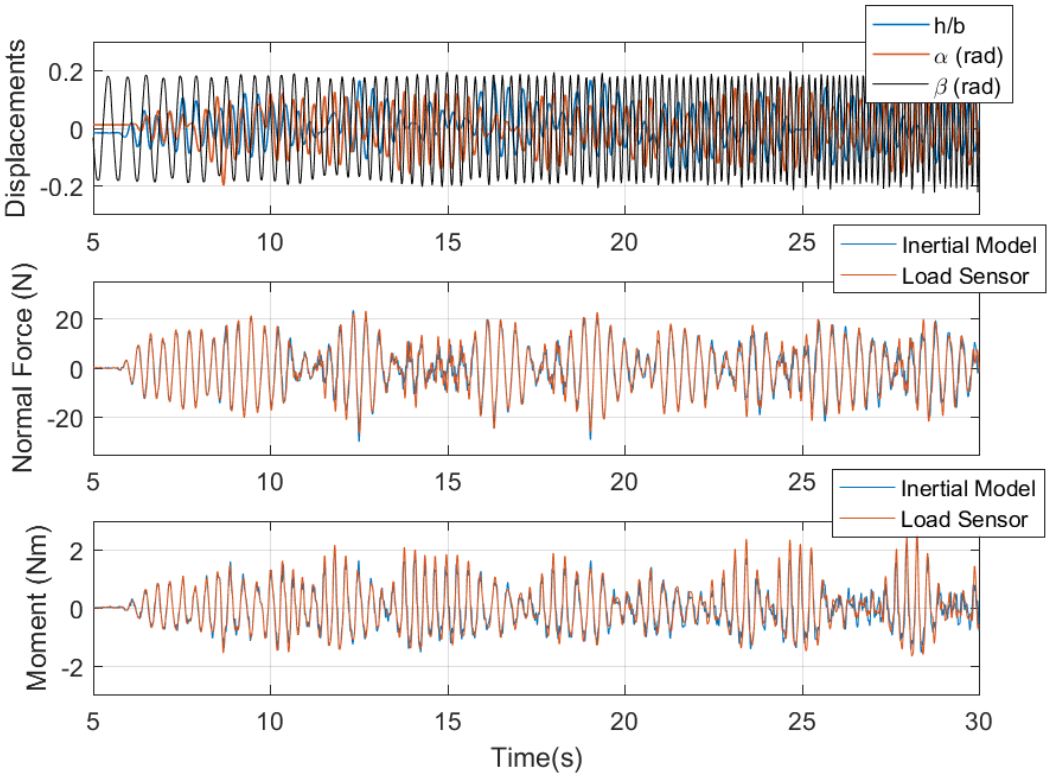

Figure 4.12: Inertial Model Predictions compared with Load Sensor Measurements.

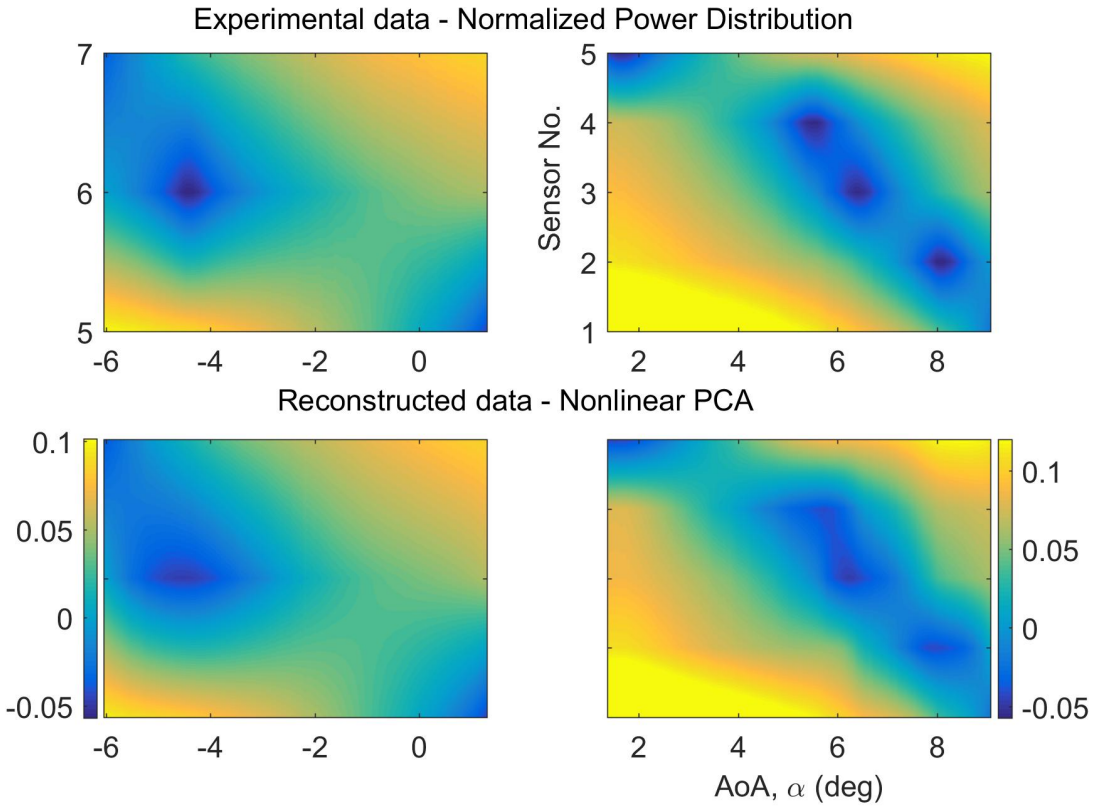

Figure 4.13: Nonlinear PCA: Validation

Figure 4.13 compares normalized experimental data with that reconstructed from the trained ANN for steady flow experiments through several angles of attack. Essential features are captured with minor discrepancies. Dark regions corresponding to a particular sensor indicate the presence of the LESP in the vicinity. The data is normalized using the procedure outlined in Section 4.3.2.

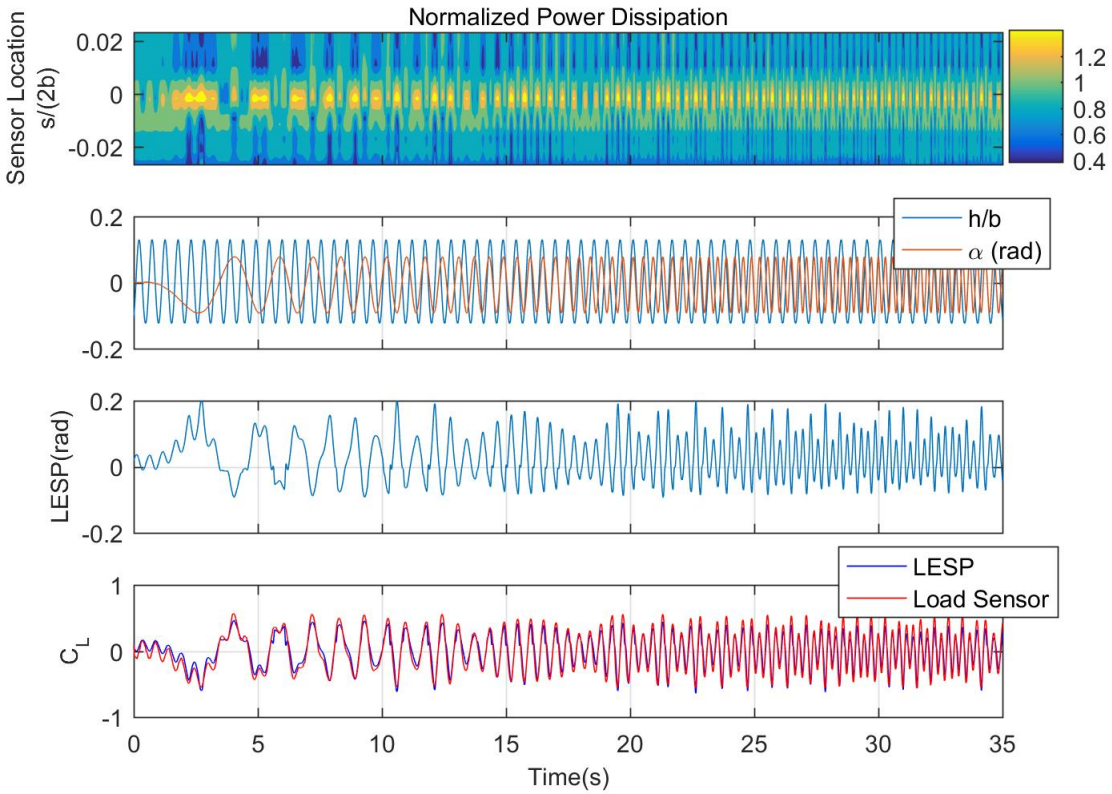

Figure 4.14: PPDS: Frequency Sweep in Pitch, Harmonic Oscillation in Plunge

Figure 4.14 shows system responses for the forced oscillation apparatus. The wing is subject to a frequency sweep in the pitch superimposed over a harmonic oscillation in the plunge mode. Note that in this case, the sensors are not calibrated and are relatively sparsely distributed around the leading-edge (Fig. 4.10). Compared to results shown in Section 3 with the high sensor resolution, note that the LESP now is no longer visible on the power dissipation contour. However, the previously discussed NLPCA technique is utilized to estimate the LESP location. Good agreement is noted between loads calculated using the LESP and the load sensors, thus validating the method to estimate the LESP and the loads model. The inertial parameters for the wing mounted on the forced oscillation

apparatus are found in Ref. [45]

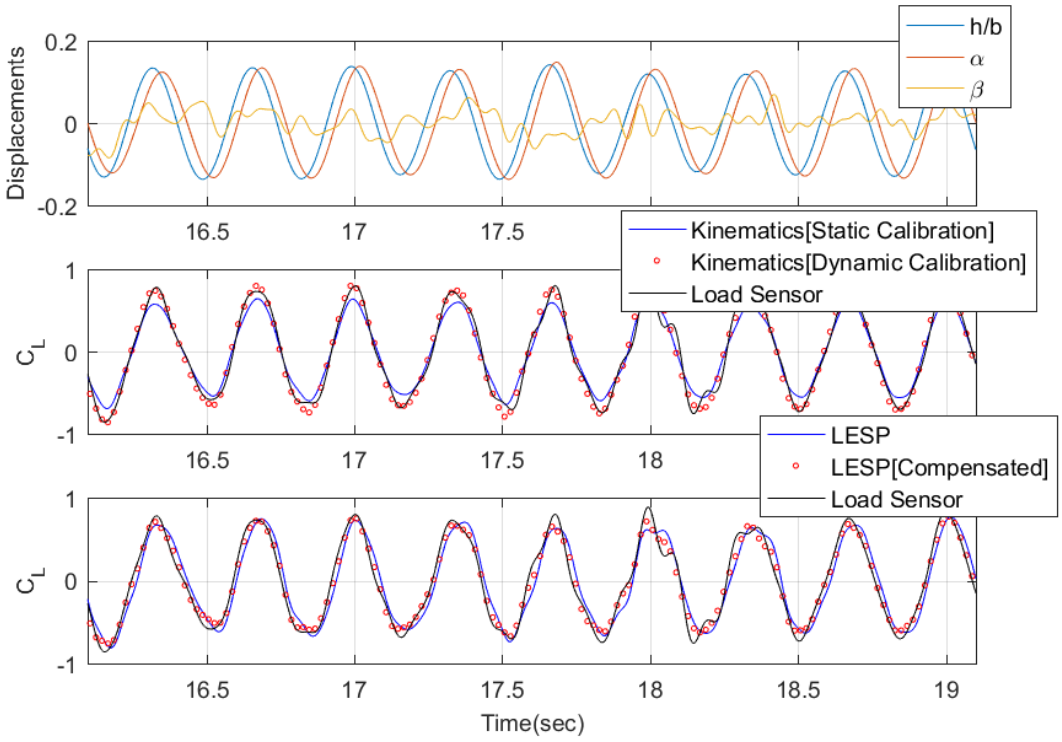

Figure 4.15: Time Domain: Model Comparison and Calibration

Figure 4.15 shows the comparison of C_L measurements for the three sensor systems for the NATA-II wing undergoing LCO with random control surface excitation. The LESP-based and statically calibrated kinematics-based sensor estimates, both dynamically uncompensated, are compared with the load sensor measurements. Both estimates show small errors in amplitude and phase. The errors for the kinematics model are attributed primarily to assumptions such as a flat wake, inviscid flow, etc. The phase-lag observed for the LESP-based estimates is primarily due to the dynamics associated with the hot-film substrate heat conduction. The amplitude errors may be due to second-order effects due

to large-amplitude oscillations. The calibrated models show improvements in comparison with the load sensor measurements for the given random excitation, thus validating the assumed model structure and the identified parameters.

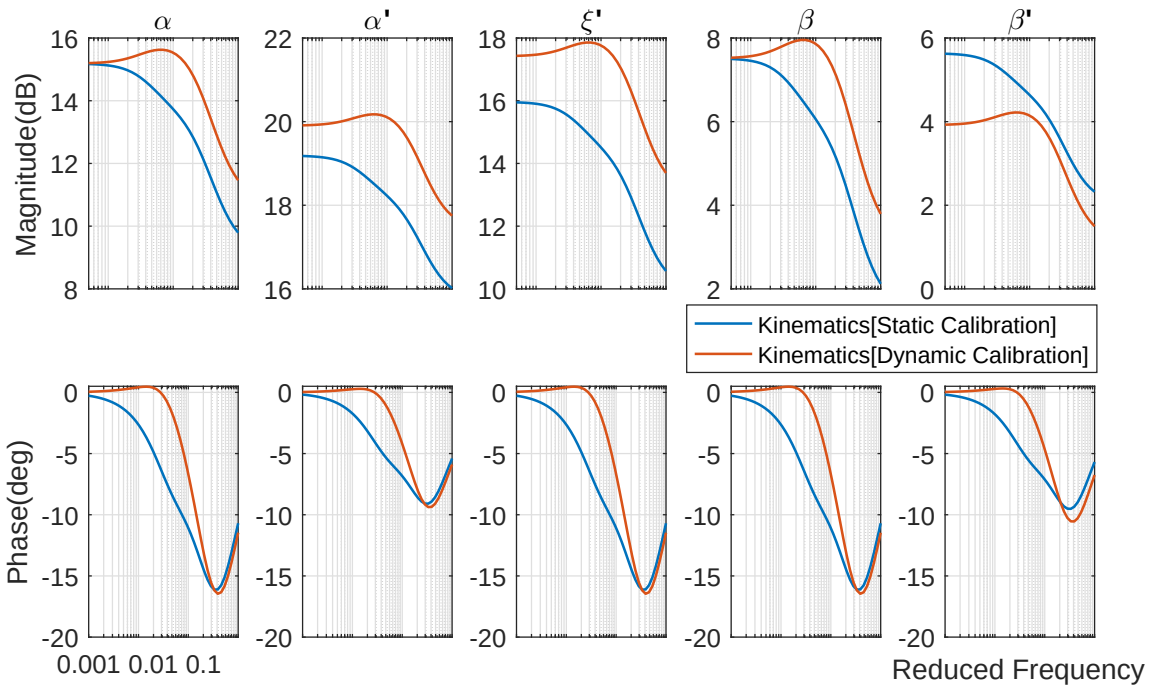

Figure 4.16: Bode Plot: Theory compared with Calibrated Model

Figure 4.16 shows the frequency response of the dynamically calibrated kinematics-based model compared with the statically calibrated equivalent. As shown, although the model is tuned for frequencies relevant to the NATA-II apparatus, its validity outside the frequency bandwidth of interest may still be reasonably accurate. Data recorded for a control surface sweep exciting both pitch and plunge modes was used for training. As expected, note that for the steady case ($\alpha', \xi', k = 0$), the frequency response of the dynamically-calibrated model with inputs α and β converges to the statically-calibrated

model (Eq. 4.31). Corrections for phase occur primarily for $0 < k < 0.1$. Substantial differences are however observed for gains associated with the rate-terms throughout the frequency spectrum.

5 APPLICATION: CONTROL OF A NONLINEAR WING SECTION

5.1 Introduction

The real-time aerodynamic sensing approach is demonstrated experimentally on the Nonlinear Aeroelastic Test Apparatus (NATA). This section details controller development, implementation and closed-loop test results using the NATA platform. The test wing is instrumented with a leading-edge hot-film sensor array that is used to locate the LESP. For the purpose of load feedback, a first-order potential flow model is used to estimate unsteady lift from the LESP displacement. The controller demonstrated experimentally is shown to be effective in the suppression of LCOs even in the presence of oncoming gusts.

The availability of real-time measurements of aerodynamic loads/circulation offers better observability of the aerodynamic modes over inertial sensors (accelerometers, gyroscopes). Accordingly, dynamic output feedback that includes circulation using modern control theory (H_2, H_∞ minimization) may potentially offer significant advantages over the conventional approach of using only inertial sensors. However, the modern state-feedback approach produces high-order complex control structures that may pose challenges to V&V (Verification and Validation) procedures and implementation. An alternative approach considered herein involves the synthesis of low-order control structures based on static-output feedback of aerodynamic loads. Stabilization is achieved

by tracking certain reference signals that are energy dissipative and by rejecting known load disturbances due to the motion of the wing. External disturbances such as gusts are attenuated as a result of feedback. The control formulation is developed from a physics-based approach using fundamental work-energy principles and unsteady thin-airfoil theory. Several studies appear in the literature that treat the flutter phenomenon from an energy perspective [57–59]. In particular, Bendiksen [59] shows that flutter occurs only within a closed region of the system phase space. The control objective, therefore, is to shape the aerodynamic loads such that this unstable region is eliminated. Such a formulation results in low-order control structures with strong robustness properties. The method thus appears particularly attractive for flutter suppression and gust load/response alleviation where stability robustness is critical.

This section is organized as follows. A simplified model of the NATA system capturing the essential physics is introduced. Subsequently, the energy-based formulation for flutter suppression is developed. A parametric study is conducted to investigate the effect of controller gains on system stabilization. The performance of the controller is evaluated using time-domain simulations and frequency-domain analysis. Finally, experimental results demonstrating the capability of the controller are discussed. A preliminary version of this section appears in Ref. [60]. Corrections and updates are provided herein.

5.2 System Model

The equations of motion for the nonlinear pitch and plunge aeroelastic apparatus appear as follows:

$$\begin{bmatrix} m_T & m_w x_\alpha b \\ m_w x_\alpha b & I_\alpha \end{bmatrix} \begin{Bmatrix} \ddot{h} \\ \ddot{\alpha} \end{Bmatrix} + \begin{bmatrix} c_h & 0 \\ 0 & c_\alpha \end{bmatrix} \begin{Bmatrix} \dot{h} \\ \dot{\alpha} \end{Bmatrix} + \begin{bmatrix} k_h & 0 \\ 0 & k_\alpha \end{bmatrix} \begin{Bmatrix} h \\ \alpha \end{Bmatrix} = \begin{Bmatrix} -C_L qS \\ C_M qSc \end{Bmatrix} \quad (5.1)$$

The pitch stiffness k_α is nonlinear and is assumed to be a polynomial function of α, whereas, the plunge stiffness is assumed to be linear. The structural damping is assumed to be viscous for both pitch and plunge modes. This assumption is less accurate for small wing motions where coulomb damping is significant. The dynamics of the control-surface are assumed to be far removed from that of the pitch-plunge structure and is uncoupled from the equations of motion (Eq. 5.1). The servo-dynamics is assumed to be second-order, of the form:

$$K_{\ddot{\beta}}\ddot{\beta} + K_{\dot{\beta}}\dot{\beta} + K_\beta \beta = \beta_{com} \quad (5.2)$$

The lift C_L and moment C_M acting on the wing section may be calculated using thin-airfoil unsteady aerodynamic theory [35]:

$$C_L = \pi\alpha' - T_4\beta' + C(k)\left[2\pi\left(\alpha + \xi' + (0.5-a)\alpha'\right) + 2T_{10}\beta + T_{11}\beta'\right] \quad (5.3)$$

$$C_M = -\frac{\pi}{2}\alpha' - \frac{(T_4+T_{10})}{2}\beta - \left[T_1 - T_8 - (c+0.5)T_4 + 0.5T_{11}\right]\frac{\beta'}{2} + \frac{(a+0.5)}{2}C_L \quad (5.4)$$

where $C(k)$ is Theodorsen's circulation function. The physical time is non-dimensionalized using $\bar{t} = \frac{tU}{b}$. The plunge displacement is normalized using the airfoil semichord, such that $\xi = \frac{h}{b}$. Moderate reduced frequencies ($k \leq 0.2$) are considered, and therefore, acceleration terms (α'', ξ'', β'') are ignored. The constants T_1, T_4, T_8, T_{11} are defined in Ref. [35] and are functions dependent on the control surface size c. The wing is mounted near the quarter-chord ($a \approx -0.5$). To express the aerodynamic model in time-domain, $C(k)$ is approximated using the rational functional approximation given by Jones [55]. For the purpose of time-domain simulations and linear system analysis, the equations are arranged in the state-space format:

$$\dot{X} = A(\alpha)X + B\beta_{com} \tag{5.5}$$

where $C(\bar{s})$ is converted to the equivalent state-space representation with two lag states. The parameter definitions and sign conventions are shown in Fig. 5.1. The parameters appearing in the aeroservoelastic model are identified experimentally from a variety of prescribed tests as described in the Section 4. Previous studies using the NATA assumed coefficients obtained from thin airfoil theory (Eqs. 5.3,5.4) due to the unavailability of a load measurement device. As shown in Fig. 5.2, significantly better agreement is found between system response predictions and measurements using the dynamically calibrated Theodorsen's model. Table 5.1 lists the various identified system parameters (repeated from Section 4 for convenience).

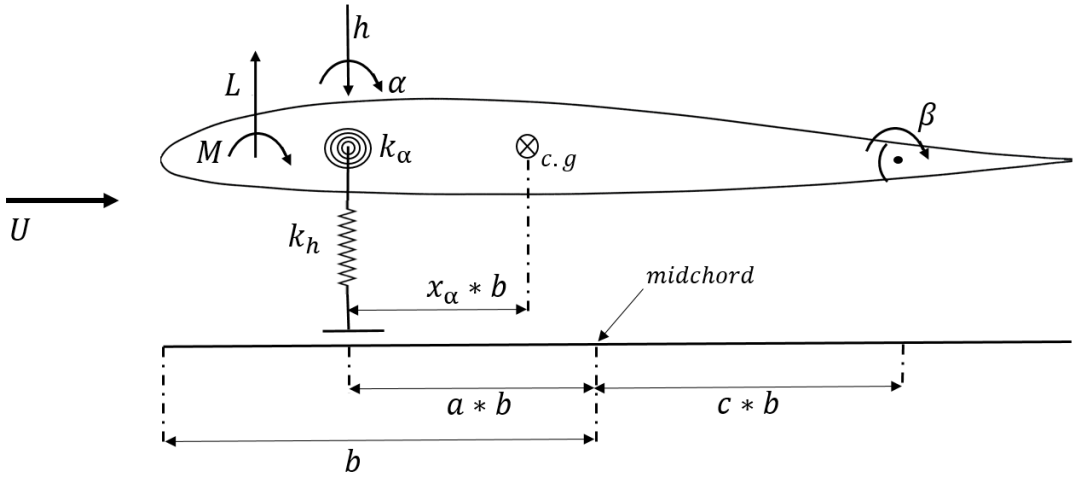

Figure 5.1: NATA-II Wing Section: Parameter Definitions and Sign Conventions

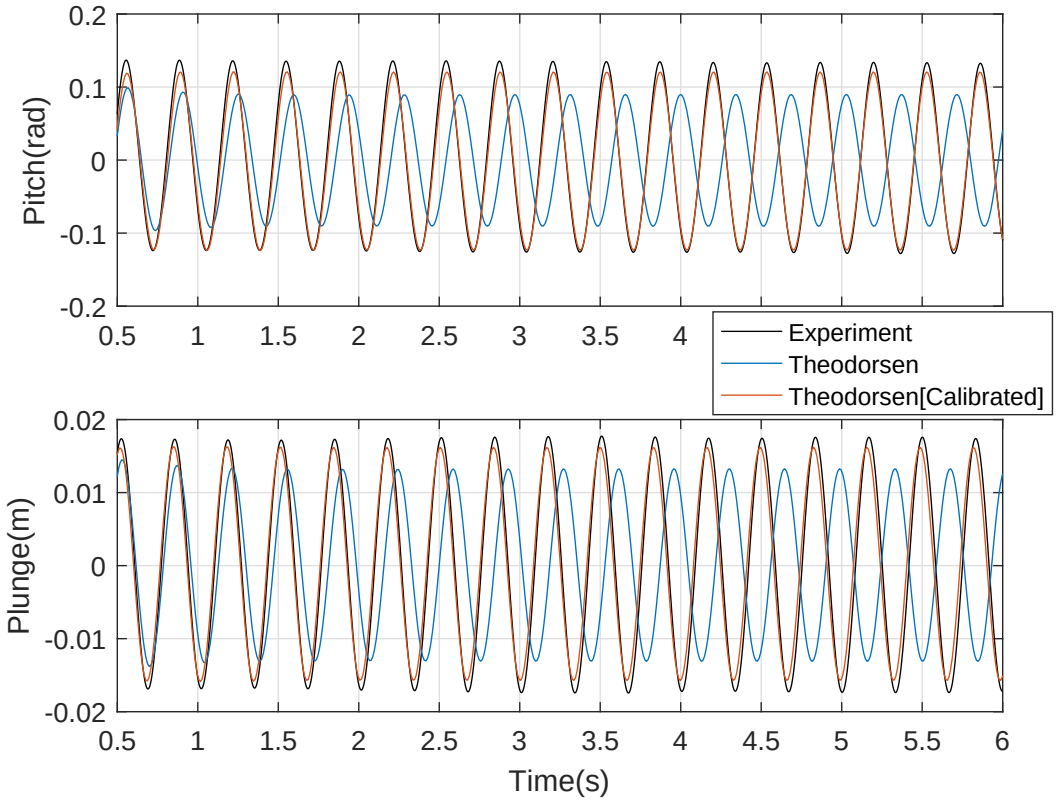

Figure 5.2: Comparison of Predicted System Responses with Experiments

Parameter	Value	Parameter	Value
ρ	1.205 $Kg.m^{-3}$	$K_{\ddot{\beta}}$	0.0002 s^2
a	-0.449	$K_{\dot{\beta}}$	0.0198 s
b	0.1397 m	K_{β}	1.0894
c	0.5	m_{w}	3.963 Kg
s	1.2192 m	m_{T}	10.99 Kg
x_{α}	0.255	I_{α}	0.0588 $Kg.m^{-2}$
k_h	2920.8 Nm^{-1}	c_h	17.514 $Kg.s^{-1}$
k_{α}	$52604\alpha^5 + 19253\alpha^4 + 201.9\alpha^3$	c_{α}	0.0923 $Kg.m^2.s^{-1}$
	$133.4\alpha^2 + 2.9037\alpha + 23.2$ $Nm.rad^{-1}$		

Table 5.1: System Parameters: NATA

The experimentally aerodynamic model is given as:

$$C_L = 3.77\alpha' + 0.49\beta' + C(\bar{s})\left[5.74\alpha + 7.42\xi' + 6.12\alpha' + 2.37\beta + 1.07\beta'\right] \quad (5.6)$$

$$C_M = -1.70\alpha' - 0.47\beta - 0.42\beta' + 0.025C_L, C(\bar{s}) = \frac{0.6\bar{s}^2 + 0.337\bar{s} + 0.0164}{\bar{s}^2 + 0.4146\bar{s} + 0.0164} \quad (5.7)$$

For the purpose of linear system analysis and time-domain simulations the identified nonlinear state-space model is built and tested using Simulink. Note that the control scheme developed herein does not require a model-based state-estimator. The purpose of the model, however, is to gauge the effect of controller gains on stabilization performance. The model is also useful to evaluate the controller performance for conditions that currently cannot be tested experimentally (for instance, different elastic axis locations and control

surface sizes).

5.3 Control Approach

Active aeroelastic control synthesis based on the modern state-space approach typically results in high-order controllers. The complexity of the controller significantly increases if nonlinearities and uncertainties are taken into account. Overall, the state-feedback approach will need to address uncertainties, nonlinearities and large-dimensionality, requiring significant effort for controller design, analysis and implementation. An alternative approach for stabilization is to directly control the aerodynamic loads using output feedback of load measurements. Energy dissipation from the structure may be achieved by shaping the aerodynamic loads such that they track relevant structural modal velocities. The effect of external disturbances such as gusts may be further attenuated due to load-feedback. As shown subsequently, low-order stabilizing control structures may be designed using this physics-based approach. The control formulation does not require a high-dimensional aeroservoelastic state-estimator, and therefore, is attractive for hardware realizations.

From an energy perspective, flutter may be recognized as an instability caused by positive work done on the structure by the aerodynamic forces through a cycle of motion. This is defined more formally using the aerodynamic work functional:

$$W_A = \int_0^T Q_i \dot{q}_i dt \tag{5.8}$$

where Q_i is the generalized aerodynamic load associated with the generalized modal coordinate q_i. If W_A is negative over a period T, then the aerodynamic forces remove energy from the structure and the system is guaranteed to be stable over the cycle. Note that the system may be stable even if energy is added through some part of the cycle. If we were to constrain the aerodynamic loads to track a certain system trajectory using a control mechanism, such that W_A is always negative, then system will be stabilized. For instance, one such candidate is $Q_i = -\dot{q}_i{}^T$. However, it is not always possible to constrain all the generalized aerodynamic forces if the system is under-actuated. For instance, reference tracking for both sectional lift and moment is not possible using only the corresponding sectional trailing edge control surface. (This is however viable with the inclusion of a leading-edge control surface). Subject to certain conditions, it is shown herein that a reference signal for only the lift coefficient, $C_{L_{Ref}} = f(\dot{h}, \dot{\alpha})$, is sufficient for stabilization. Classical single input–single output feedback structures may then be designed for reference tracking.

From Eq. 5.8, it may be recognized that the existence of a neutrally stable surface ($W_A = 0$) in the system phase-space suggests the possible existence of flutter (The phase-space for a particular reduced frequency is spanned by the gain and phase of the plunge mode relative to pitch). Bendiksen [59] shows that this region is a compact closed surface

within which $W_A > 0$. Aerodynamic energy contours for an airfoil may be obtained using the complex aerodynamic influence coefficient matrix constructed from the identified aerodynamic model (Eqs. 5.6, 5.7):

$$\begin{bmatrix} C_L \\ C_M \end{bmatrix} = \begin{bmatrix} \mathbf{A}(k,a) \end{bmatrix} \begin{bmatrix} \xi \\ \alpha \end{bmatrix}$$

where, $\xi = \xi_0 e^{ik\bar{t}}$, $\alpha = \alpha_0 e^{i(k\bar{t}-\phi)}$ and the gain, $G = \xi_0/\alpha_0$. Complex matrix $\mathbf{A}(k,a)$ is a function of the reduced frequency k and pitch axis location a. The reduced frequencies of interest are determined from the structural dynamics and freestream properties. The non-dimensional aerodynamic input power to the structure is given by:

$$\bar{P}_A = -Re(C_L).Re(\xi') + Re(2C_M)Re(\alpha') \tag{5.10}$$

The contribution of the aerodynamic hinge moment to the input power is not considered for analysis because the inertial coupling of the control surface with the wing is assumed to be sufficiently weak. Only the pitch and plunge modes are assumed to be relevant. The aerodynamic work functional in terms of $\bar{P}_A$ is then:

$$W_A = \int_0^{\frac{2\pi}{\omega}} P_A dt = \rho U^2 b^2 \int_0^{\frac{2\pi}{k}} \bar{P}_A d\bar{t} \tag{5.11}$$

The work done expression (Eq. 5.11) is valid only when the wing is subjected to harmonic motions. The expression is not accurate for fast convergent/divergent oscillations. Figure 5.3a shows the contour plot of the aerodynamic work functional evaluated through

the phase-space for the open-loop system. The existence of the flutter boundary separating unstable and stable regions is noted for $k = 0.2, a = -0.5$. The transition from the stable to unstable region therefore indicates that a surface of neutral stability exists ($W_A = 0$). Thus, the plot represents a search through the phase-space for a possible Hopf bifurcation. Also, the unstable region provides necessary conditions (gain, phase) for single harmonic LCOs to exist. For instance, experimentally observed LCOs (near flutter onset) occur at $k = 0.2$ with a gain of 0.96 and phase, 34 deg. Note that the distance from the flutter boundary is a measure of structural damping present in the system. The existence of a neutrally stable surface does not imply the existence of flutter/LCOs but rather provides conditions (gain, phase) for which flutter/LCOs might occur. The possibility of flutter is determined by considering, in addition, the properties of the free-stream and the structure. At the critical flutter speed, however, the system will lie near a neutrally stable surface. The open-loop eigen-value analysis (Fig. 5.3b) obtained by linearizing Eq. 5.5 about zero pitch and zero plunge indicates a flutter onset at $U = 11$m/s with $k \approx 0.3$. Neutrally stable surfaces are observed for the relevant reduced frequency range: $0.1 < k < 0.6$.

If we were to actively control the aerodynamic loads such that W_A is negative throughout the relevant phase space and reduced frequency range, then, regardless of the structural properties, flutter or LCOs cannot occur. Since reference tracking for C_L may be achieved using the trailing-edge control surface, $C_{L_{Ref}}$ is found such that $W_A < 0$ for the stated conditions.

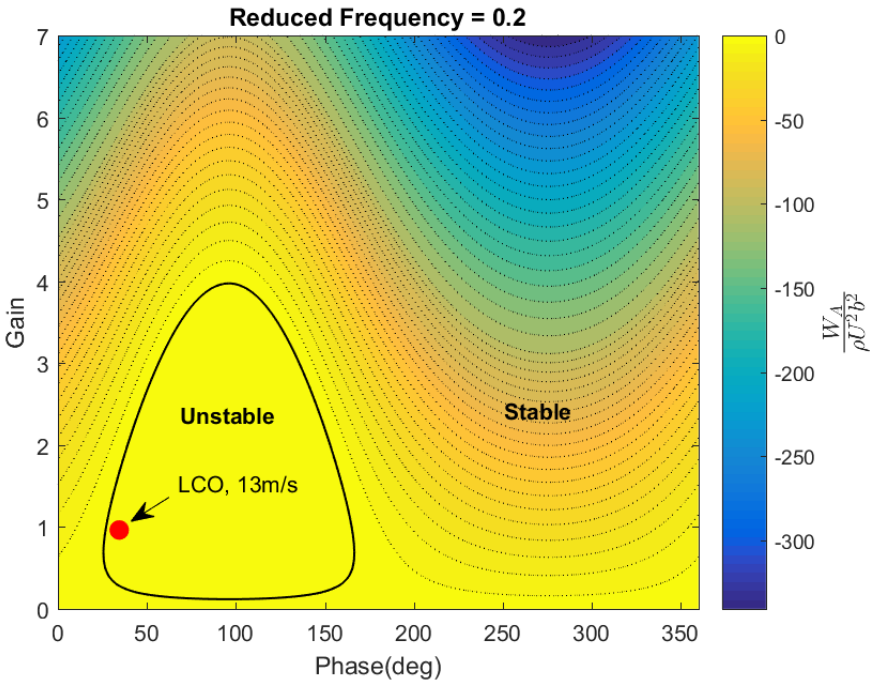

(a) Phase Plot

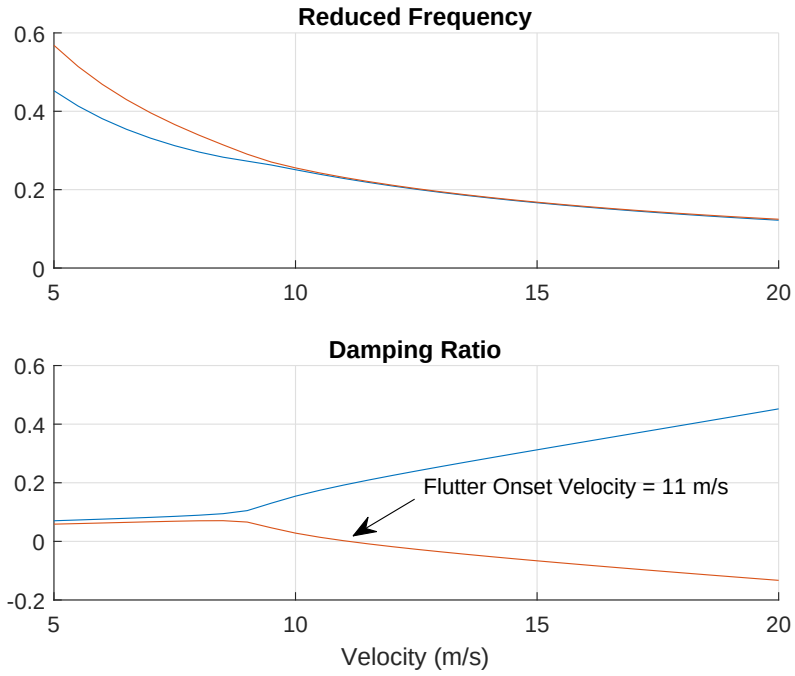

(b) Linear Analysis

Figure 5.3: Open-Loop Analysis

Substituting 5.4 in Eq. 5.10, we have:

$$\bar{P}_A = -Re(C_L).Re\left(\xi' - (a+0.5)\alpha'\right) - \pi Re(\alpha')Re(\alpha') - (T_4 + T_{10})Re(\beta)Re(\alpha')$$
$$-(T_1 - T_8 - (c+0.5)T_4 + 0.5T_{11})Re(\beta')Re(\alpha') \tag{5.12}$$

Examining Eq. 5.12, if C_L is constrained to track the reference, $C_{L_{ref}} = K_{CL}.(\xi' - (a+0.5)\alpha')$, then the first term is negative. Due to deficiencies in tracking the reference, the following output with a phase-lag and amplitude error may be obtained instead:

$$C_L = K_c\left(\xi' - (a+0.5)\alpha'\right)e^{-\tau j} \tag{5.13}$$

where, K_c is the resultant gain on the reference signal with delay, τ.

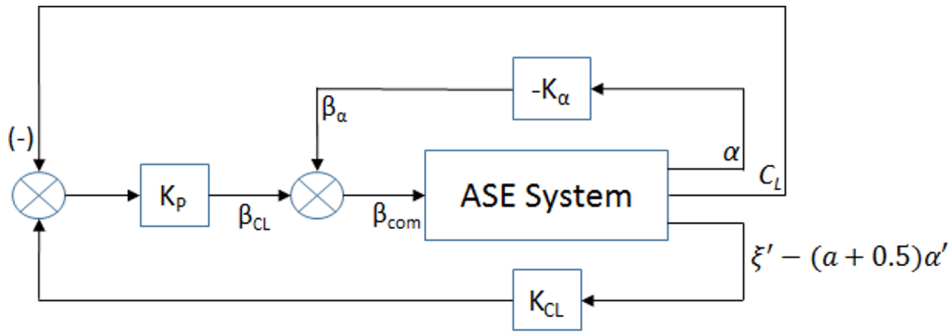

Figure 5.4: Sectional Control Framework

The second term in Eq. 5.12 is always negative. The sign of the third and fourth terms depends on β and β'. Note that $\beta(t)$ depends on the control scheme used to track $C_{L_{ref}}$. A simple tracking structure for this purpose is illustrated in Fig. 5.4. The aerodynamic

system to be controlled is assumed to be of the form: $\beta \rightarrow C_L(\beta, w)$, where w represents the set of exogenous inputs resulting from motion in pitch, plunge and gusts. To improve tracking performance, known components of w are rejected. Unknown disturbances due to gusts are rejected as a result of feedback. With this control structure, C_L is then given as:

$$C_L = C_{L_\alpha}\alpha + C_{L_\beta}(\beta_{CL} + \beta_\alpha) + \Delta(\xi', \alpha', \beta', ...) \tag{5.14}$$

For low reduced frequencies, the effect of the rate terms are minor and the system $\beta \rightarrow C_L(\alpha, \beta)$ is approximately static. K_α is therefore chosen such that $K_\alpha\alpha$ approximately cancels $C_{L_\alpha}\alpha$ through $\beta_\alpha = -K_\alpha\alpha$. Since, $K_\alpha \approx \frac{C_{L_\alpha}}{C_{L_\beta}} \approx 2$ may result in large control surface deflections, K_α must be chosen such that control surface saturation is avoided. A similar simplified relationship does not exist for structural outputs since the system $\beta \rightarrow \alpha$ is nonlinear with slow dynamics (due to the low-pass filter characteristics of the structure). Note that β_α is orthogonal to α' and does not contribute to the work.

Δ contains the effects of rate terms, aerodynamic lag states and gusts. With $C_{L_\alpha}\alpha$ largely eliminated, $\beta_{CL} = \frac{C_L - \Delta}{C_{L_\beta}}$. To simplify analysis, the effect of β_{CL} is considered on a worst-case basis, such that:

$$\beta_{CL} = -K_e \frac{|C_L|}{C_{L_\beta}} \frac{\alpha'}{|\alpha'|} \tag{5.15}$$

β_{CL} is defined to be in-phase with $-\alpha'$ so that it's contribution to the aerodynamic

work is always positive. Note that $(T_4 + T_{10})$ in Eq. 5.12 is positive for $0 < c < 1$. K_e is a multiplicative factor expressing the effect of Δ. For very low reduced frequencies with no external disturbances, $K_e \approx 1$.

Retaining only first derivatives, we have:

$$\beta' = \beta'_{CL} + \beta'_{\alpha} \approx -K_{\alpha}\alpha' \tag{5.16}$$

The effect of β' is destabilizing, since $T_1 - T_8 - (c + 0.5)T_4 + 0.5T_{11} > 0$ for $0 < c < 1$.

With the assigned behavior of β, a parametric study is conducted to ascertain regions of the parameter space for which the controller is stabilizing. From Eqs. 5.11, 5.12, 5.13, 5.15, 5.16 and defining $x = k\bar{t}$, we have $W_A = \rho U^2 b^2 k \alpha_0^2 I$. The sign of W_A now depends on that of integral I, given by:

$$I = \int_0^{2\pi} f(G, \phi, \tau, K_c, K_e, K_{\alpha}, x)dx \tag{5.17}$$

As previously discussed, the controller is stabilizing, if the aerodynamic work functional is negative throughout the phase-space (G, ϕ) and reduced frequency range of interest. Note however that I does not depend on the reduced frequency. From Eq. 5.11, to find regions where $I < 0$, a parameter study is conducted on the variables $[G, \phi, \tau, K_c, K_e, K_{\alpha}]$ in addition to studying the effect of the elastic axis placement a and the control surface size c. The following procedure for the parameter search is conducted. With $K_{\alpha} = 2$, a search through (τ, K_e) is initially conducted on a discretized phase-space

(G, ϕ) of size 50x50, where $G = 0 : 10$ and $\phi = 0 : 2\pi$. The phase space grid may be expanded and/or refined to confirm stability margins. Subsequently, the parameter space (τ, K_e) is partitioned into stable and unstable regions, for fixed K_c, c and a. The effect of K_c, c or a is then assessed separately as shown in Figs. 5.5 and 5.6.

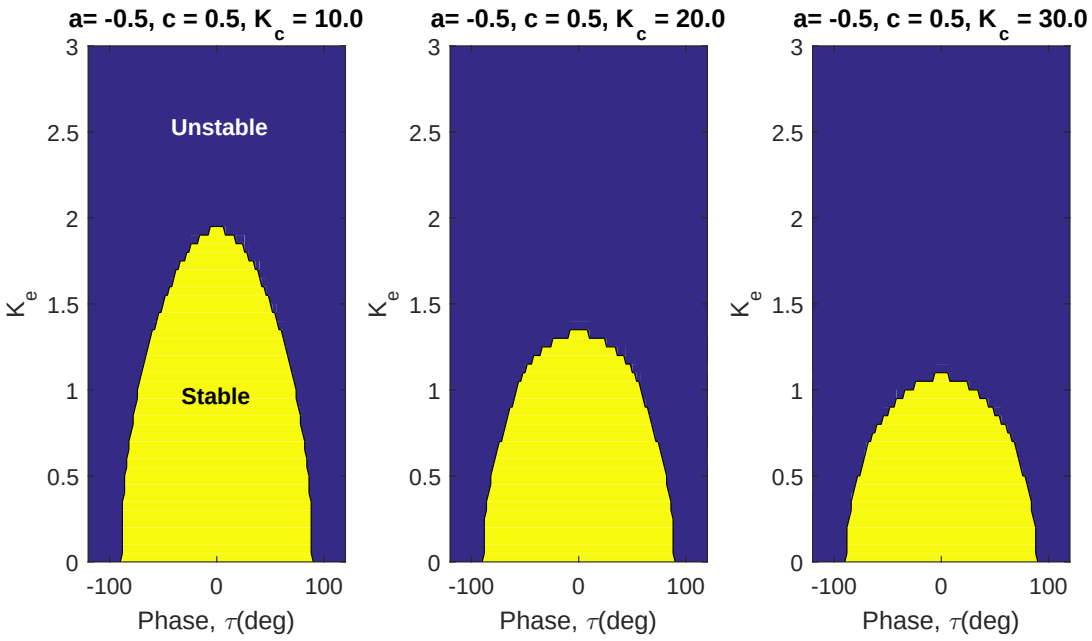

Figure 5.5: Parameter Study - Variation through Gain K_c

For $K_c = 10$, Fig. 5.5 indicates that stabilization is achieved even for $\Delta \approx \pm 100\% C_L$ for small phase-lags. Further, for $K_e \ll 1$, large phase-lags upto 90 deg may be tolerated. As the gain K_c increases or with larger delays in reference tracking the size of Δ allowable for stability decreases. Note that conducting a similar study for a, it was found that the elastic axis location does not significantly influence the stability boundary. Moving the control surface hinge further aft enlarges the stable

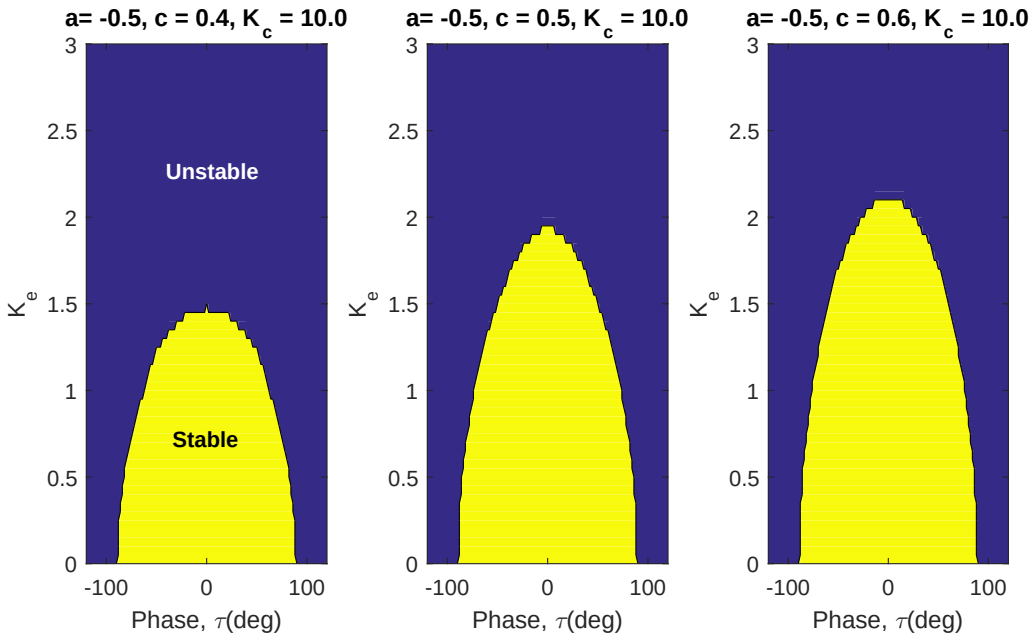

Figure 5.6: Parameter Study - Variation through Control Surface Size, c

region (Fig. 5.6). However, the realization of the stable regions depends on tracking requirements being met with a smaller control power. The utility of the phase-space search is that stability information about the controller may be quickly ascertained without the need for a complex aeroservoelastic model. However, Figs. 5.5 and 5.6 represent a worst-case analysis and faster stabilization may be achieved in practice with larger control gains.

The control approach (Fig. 5.4) is evaluated using numerical and experimental studies of the NATA apparatus. Since $a \approx -0.5$, the reference signal is now specified as $C_{L_{ref}} = K_{CL}.\xi'$. From closed-loop wind tunnel tests, the tuned gain setting: $K_\alpha = 2, K_P = 0.2, K_{CL} = 40$ was found to provide good controller performance with

minimal control surface saturation. Anticipated future efforts will address the use of optimization methods to determine optimal gains for this control structure. Numerical results (frequency and time domain) are discussed in the remainder of this section. Specifically, the effect of gains K_a, K_P and K_{CL} on controller performance and stability is identified.

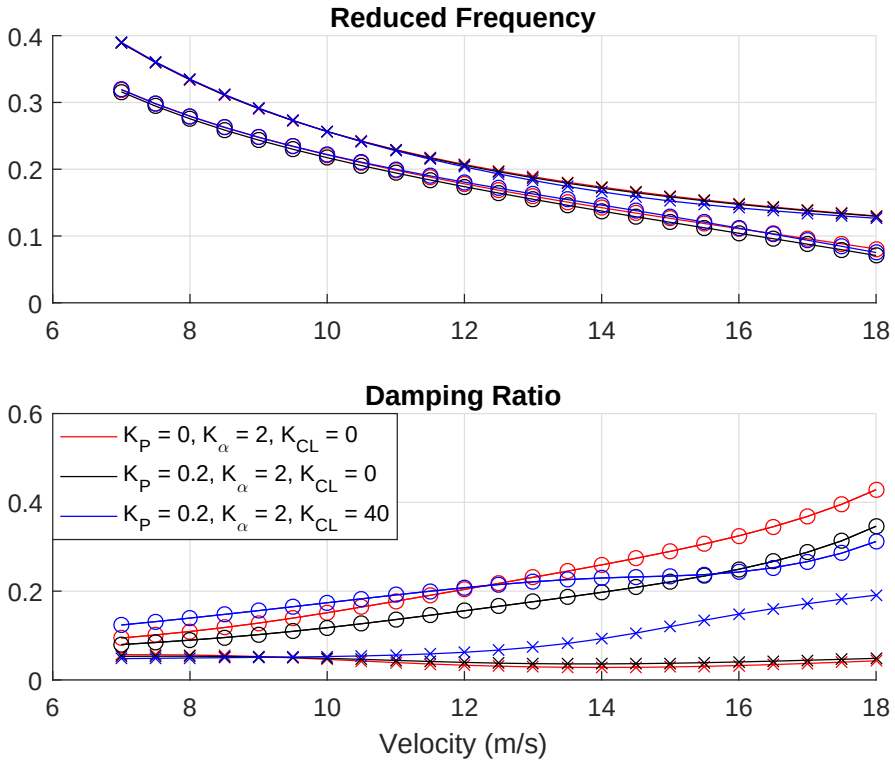

Figure 5.7: Effect of Velocity on System Modes

Figures 5.7 and 5.8 show the results of linear analysis conducted on the closed-loop system. The variation of modal eigenvalues for different control gains and the freestream velocity is investigated. Modes associated with the servodynamics or aerodynamic lag-

states are not shown. Note that the system is stabilized by simply eliminating $C_{L_\alpha}\alpha$ through the gain K_α (case: $K_P = 0, K_\alpha = 2, K_{CL} = 0$).

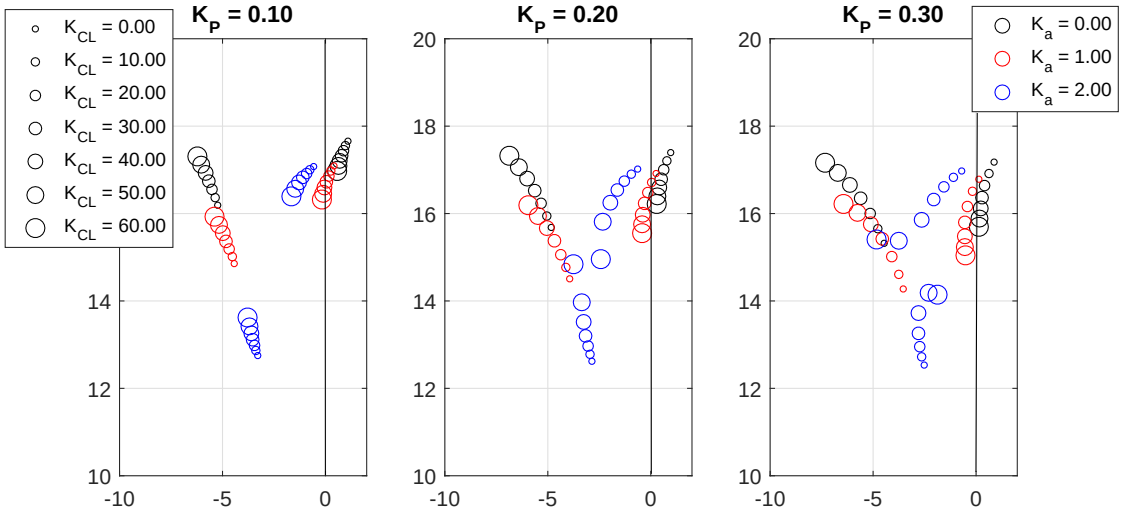

Figure 5.8: Effect of Gains on System Eigenvalues

Figure 5.8 also reveals a marked change in the eigenvalue trajectories for $K_\alpha = 2$. Improvement in performance (increased modal damping) is obtained by including and increasing control gains: K_P and K_{CL}. However, improvements in performance will be accompanied by increased control effort. The analysis shows the modal damping increasing with airspeed. However, in practice, the servo will eventually lose control authority at high dynamic pressures possibly resulting in system instability. Note that for the tested wind tunnel speed range, the servodynamics model is assumed to be invariant with the freestream velocity. The closed-loop system shows a greater separation of modal frequencies compared with the uncontrolled system indicating an increased resistance for modal interactions (Compare Figs. 5.3b and 5.7). Strong coupling between aeroelastic modes may be recognized as a characteristic feature of binary flutter. Including

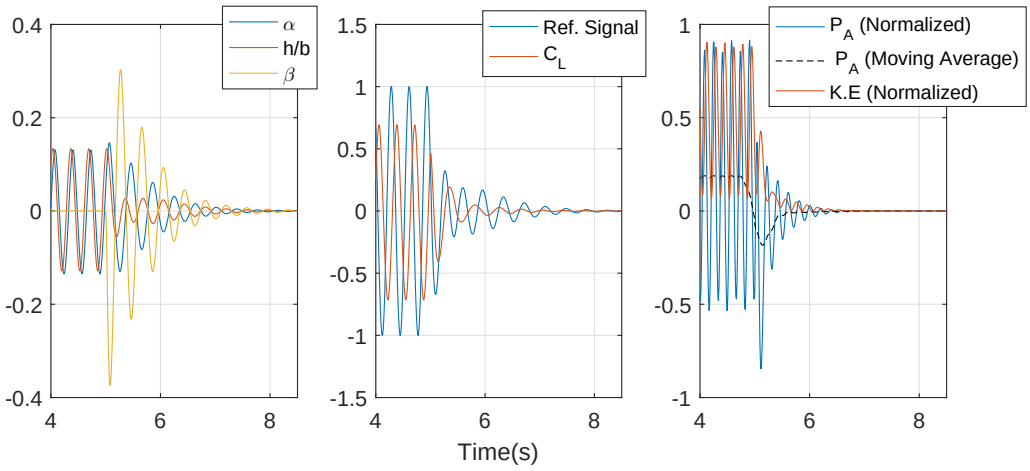

Figure 5.9: Nonlinear System Simulation ($U = 14m/s$)

gains K_P and K_{CL} has a negligible influence on the modal reduced frequencies (Fig. 5.7).

Figure 5.9 shows the time-domain simulation of the closed-loop nonlinear system for conditions similar to the experimental setup. The controller stabilizes the fully developed LCO in about two seconds. As discussed earlier, in addition to preventing a Hopf bifurcation, the control does not allow the existence of stable harmonic LCOs. Should the nonlinear response contain multiple harmonics, it is possible to show stability using Eq. 5.11 through a Fourier series expansion. The worst-case scenario described by Eq. 5.15 implies that stable regions determined from (Eq. 5.10, Figs. 5.5 and 5.6) will remain stable for the following redefinition for β (required for Fourier decomposition):

$$\beta = K_e \frac{C_L}{C_{L_\beta}} - K_\alpha \alpha \tag{5.18}$$

Note that Figs. 5.5 and 5.6 are independent of frequency. The cross-terms arising in Eq. 5.10 due to disparate harmonics may be expanded and shown to be zero when

integrated through the corresponding cycle. In contrast to this simple control scheme, the use of state-feedback while accounting for nonlinearities and model uncertainty requires a relatively complex adaptive feedback linearization scheme to suppress LCOs (For instance, see Ref. [19]).

Figure 5.9(b) shows the performance of the controller in tracking $C_{L_{ref}}$ and Fig. 5.9(c) shows the instantaneous aerodynamic power P_A and the kinetic energy ($K.E$) of the system. $K.E$ is calculated as follows:

$$K.E = \frac{1}{2} m_T \dot{h}^2 + m_W x_\alpha b \dot{h} \dot{\alpha} + \frac{1}{2} I_\alpha \dot{\alpha}^2 \tag{5.19}$$

To aid in comparison, P_A and $K.E$ are normalized with respect to their maximum absolute values. An approximate estimate of the per cycle mean of P_A computed using a moving average filter is also shown. For the open-loop system in LCO prior to control action, the mean P_A is constant and positive. The energy balance between aerodynamic and dissipative structural damping forces results in a constant mean $K.E$. The controller initially shows strong phase-tracking performance and this results in the negative peak P_A. Phase-tracking performance eventually deteriorates as system responses are minimized. However, at this stage, the system energy has already significantly reduced.

Since the natural frequencies for the NATA apparatus are small (≈ 2 Hz), tracking the system response $(\xi' - (a+0.5)\alpha')$ results in smooth stabilization. However, if higher gains are specified, faster stabilization may be obtained at the expense of noise

amplification, and possibly, instability. Low gains provide some disturbance rejection, but also result in steady-state errors. However, from Eq. 5.10, note that maintaining low phase-lags is critical for stability; amplitude errors are relatively inconsequential. Stabilization, therefore, is limited by phase-tracking performance. As noted earlier, at high dynamic pressures, tracking performance, and therefore, stability may be compromised due to torque limitations of the servomotor. Note that for $K_{CL} = 40$, assuming low reduced frequencies and fast servodynamics, a low value for $K_c \approx \frac{C_{L_\beta} K_P K_{CL}}{1+C_{L_\beta} K_P} \approx 10$ is found as a result of the low proportional gain.

The controller, if it is has successfully stabilized the wing, will drive the wing to an aeroelastic equilibrium position, i.e., a stable fixed point of the nonlinear system. Assuming the steady-state error associated with the feedback system is small ($\beta_{CL} \approx 0$), $\beta \approx -K_\alpha \alpha$. The fixed point(s) are then determined from Eq. 5.1. To ensure only one stable fixed point exists at zero pitch and zero plunge, the following condition may be derived:

$$U_{crit} < \sqrt{\frac{k_{\alpha_{lin}}}{2\rho s b^2 (C_{m_\alpha} - C_{m_\beta} K_\alpha)}} \tag{5.20}$$

where $k_{\alpha_{lin}}$ is the linearized pitch stiffness. For the NATA system, $U_{crit} = 20.5$ m/s. Only one stable fixed point exists in this case since the pitch stiffness is spring-hardening. Simulations show that the nonlinear system stabilizes to a nonzero pitch and plunge position for $U \geq U_{crit}$. For a wing that is in open-loop aeroelastic equilibrium

where the geometric angle of attack is nonzero, C_L, α, h are measured with respect to their equivalent equilibrium values prior to applying control. The controller will then stabilize the wing to the aeroelastic equilibrium.

5.4 Experimental Demonstration

The controller was tested at Texas A&M university's 3'x4' low speed wind tunnel. The test facility is equipped with a Pitch-Plunge Drive System (PPDS) for forced oscillation experiments and a Nonlinear Aeroelastic Test Apparatus (NATA), descriptions of which are provided in Section 4. The control structure outlined in Fig. 5.4 is implemented on the NI-PXI platform for real-time acquisition and control command processing. The processing includes the identification of the LESP from the hot-film sensors and the subsequent unsteady lift estimation.

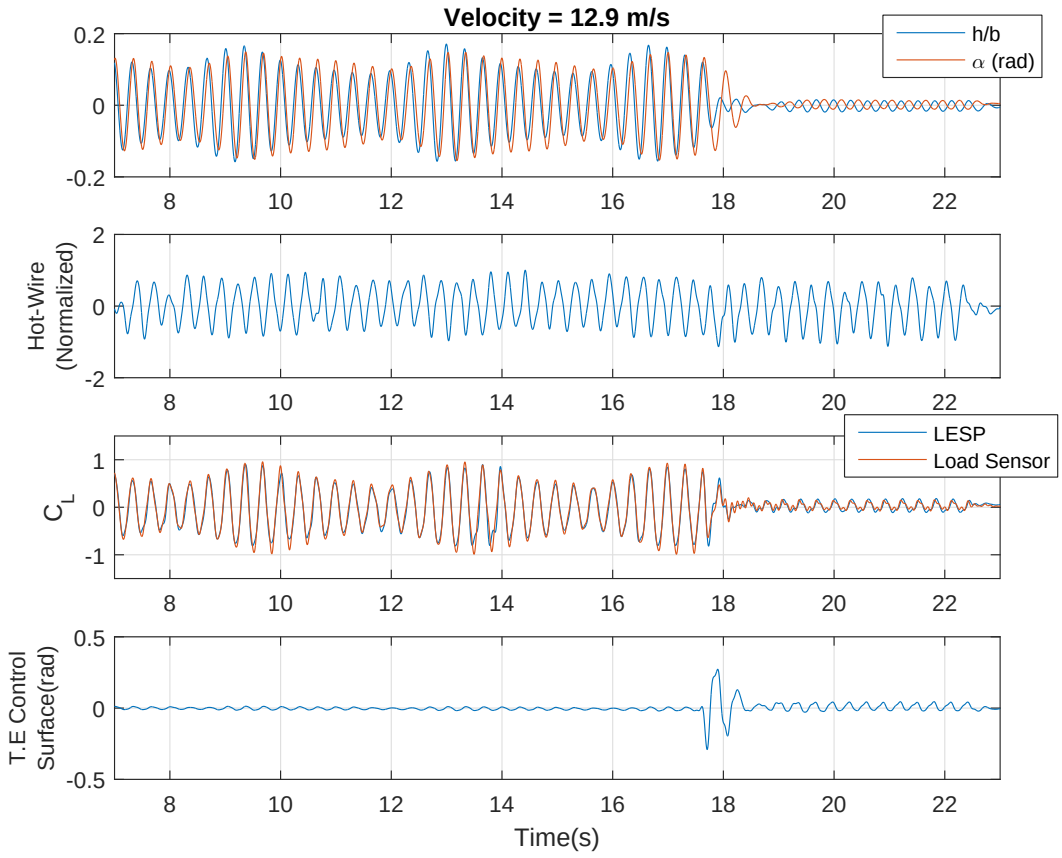

Figure 5.10: Gust Load Alleviation

Figure 5.10 demonstrates the capability of the controller in suppressing LCOs and alleviating gust loads. The control gain setting: $K_P = 0.2, K_\alpha = 2, K_{CL} = 40$ is used for this case. The gust generator is first activated and as a result of flow disturbances, the open-loop system is entrained to a LCO. The system LCO responses are seen to be modulated due to the oncoming gust excitation. The frequency content of the gusts is known approximately from the hot-wire sensor mounted ahead of the NATA wing. Good agreement is noted between loads estimated using the LESP and the load sensor recognizing that multiple sources contribute to the aerodynamic loading - gusts and

motion in pitch, plunge and control surface modes. After the system response has fully developed, the controller is activated (at about 17.5 seconds). The controller succeeds in suppressing the LCO as well as significantly attenuating the effect of gusts. Fast stabilization is achieved in about one second.

Figures 5.11 and 5.12 show the progressive effect of including various controller gains. Figure 5.11 demonstrates stabilization performance given a perturbation in the plunge mode. The wing is released from an initial plunge displacement $h = 0.2b$ with the controller active. Note that the pitch mode is also excited due to inertial and aerodynamic coupling. For the results shown in Fig. 5.12, the controller is activated after the LCO has fully developed, approximately 10 secs after an initial pitch displacement of 10 deg is given to the open-loop system. As noted previously (see Figs. 5.7 and 5.8), the case: $K_P = 0, K_\alpha = 2, K_{CL} = 0$ in Figs. 5.11 and 5.12 demonstrates that it is possible to stabilize the system by simply rejecting the angle of attack contribution. However, stability is marginal, as the system takes about six seconds to reach equilibrium. A substantial improvement in stabilization performance in terms of settling time is achieved by using C_L output feedback. Further gains in performance are obtained by including gain K_{CL}.

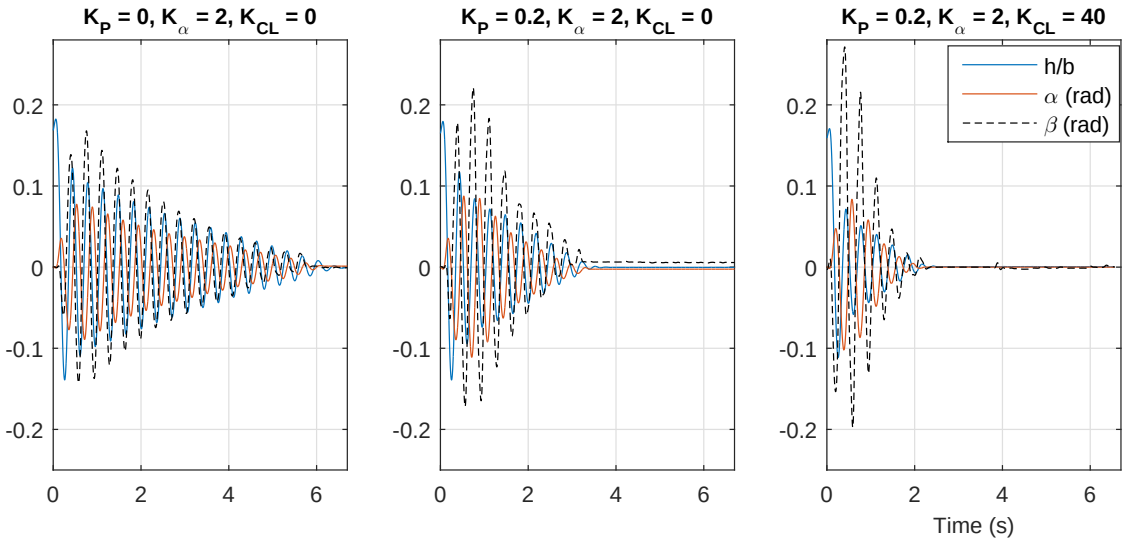

Figure 5.11: Response to Initial Plunge Displacement

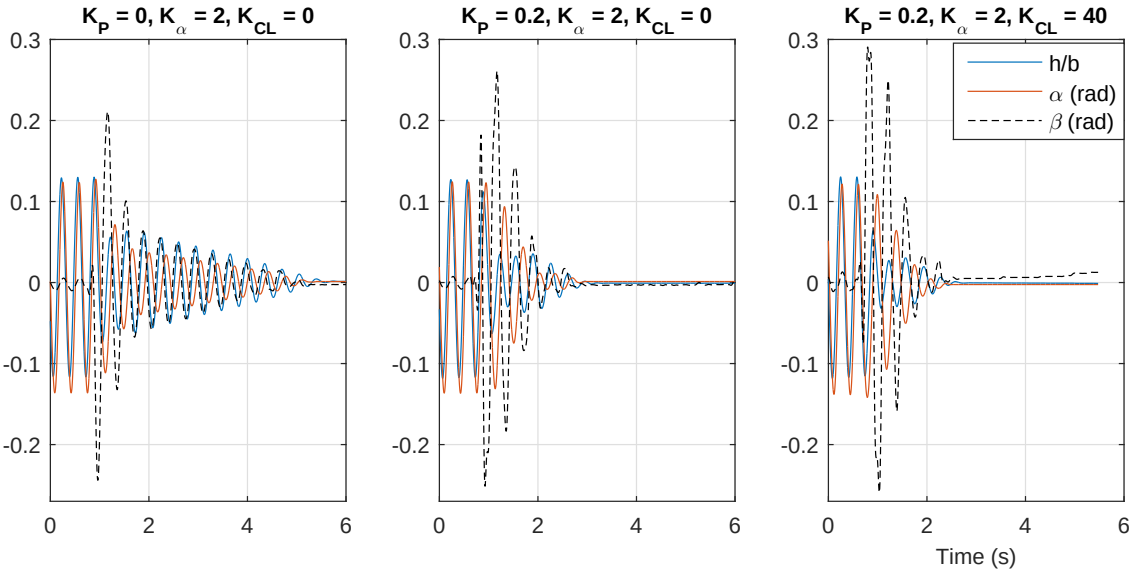

Figure 5.12: LCO Suppression

However, the effect of reference tracking is more pronounced for the initial plunge displacement case, since the controller with $C_{L_{Ref}} = K_{CL}\xi'$ provides a virtual damping effect in the plunge mode. The settling time for this case reduces to about a second. This

effect is however less pronounced for LCO stabilization (Fig. 5.12) due to the dominance of the pitch mode. Note that with improvements in performance, controller effort also increases as evidenced by the larger control surface displacements. In particular, large pitch displacements for the wing in LCO (Fig. 5.12) result in large control commands due to the high K_α gain.

6 APPLICATION: DISTRIBUTED SENSING AND CONTROL

6.1 Introduction

In this section, the energy-based sectional sensing control approach is extended to a flying wing configuration. Flying wing configurations offer several advantages [61] – Reduced wetted area, increased possibility for laminar flow, reduced intersection drag and high aerodynamic efficiency. However, the configuration is susceptible to the Body-Freedom-Flutter (BFF) phenomenon where the rigid-body modes interact with the structural modes. Typically, for swept-back flying wing configurations, this involves the coupling of the short-period pitch mode with a bending mode. Several studies have appeared in the recent literature examining this phenomenon [4, 61–65]. The X-56A MUTT (Multi-Utility Technology Testbed) [10] is an ongoing program to study active control methods to suppress BFF. In addition, several tools have been developed to investigate the interaction of rigid-body modes and structural modes for high-aspect ratio aircraft. Patil and Hodges developed NATASHA (Nonlinear Aeroelastic Trim and Stability of HALE Aircraft) [66] using composite beam theory and Peters' inflow method to model the unsteady aerodynamics. A similar tool was developed by Cesnik et al – UM/NAST (University of Michigan, Nonlinear Aeroelastic Simulation Toolbox) [67]. ASWING is an analysis tool developed by Drela [68] for the analysis and control design of high-aspect ratio aircraft using nonlinear beam theory and an unsteady lifting line aerodynamic model. For this study, ASWING is used to generate an ASE model of a

flexible flying wing configuration equipped with co-located sensors and actuators. A load-based feedback approach is used to constrain the aerodynamic loads to track certain velocity signals associated with the structural modes. The reference signals are specified such that they result in energy dissipation, potentially stabilizing BFF. Further stability and better tracking performance is achieved by rejecting the contribution of airfoil pitch. A high-pass filter is utilized to ensure the controller is active only for frequencies relevant to BFF. For controller performance comparisons, a LQG controller is designed based on output feedback of co-located sensors measuring kinematic states.

This section is organized as follows. Section 6.2 outlines the distributed controls approach based on the sectional framework. Section 6.3 provides various results characterizing the open-loop dynamics of the aircraft, the controller performance, sensitivity to gains and robustness. A preliminary version of this section appears in Ref. [69]. Corrections and updates are provided herein.

6.2 Extension to Flying Wing Configurations

The sectional controls approach described in Section 5 may be extended to a flying wing configuration using a co-located sensor and actuator framework distributed spanwise. If energy dissipation is achieved for all individual sections, then structural stabilization may be expected for the full configuration. Advanced tracking structures for this MIMO system may be designed to suitably decouple interactions between sections.

However, provided interactions are weak, simple control structures may be designed independently for each section using the sectional approach described previously. For the test case evaluated in the next section, this simple scheme achieved appreciable extension of the critical flutter speed. To decouple the stabilization action from the rigid-body dynamics (other than the BFF short-period mode), a high-pass filter is introduced. The cut-off frequency is chosen based on the natural frequency of the BFF mode (identified from an open-loop analysis of the flexible aircraft).

Figure 6.1 illustrates the approach. The sensor package that is distributed spanwise along the elastic axis provides aerodynamic (loads) and inertial (displacements, velocities) measurements. The control structure is mirrored across all sections. Gain K_P acts on the feedback path for the circulation to track the velocity signals. Gain K_D that acts on the velocity signals controls the amount of damping entering the system. Gain K_α acting on the sectional pitch output attenuates the contribution of the airfoil pitch to the aerodynamic loads. The primary actuators are the trailing-edge control surfaces (TECS) distributed spanwise. To mitigate moments generated as a result of TECS deflections, leading-edge surfaces are used. For each section, given the TECS command β_{com}, the leading edge deflection is given by $\gamma = \frac{-C_{m_\beta}}{C_{m_\gamma}}$. Since the only states that need to be integrated are those of the high-pass filter, the overall output feedback control structure will be of low-order provided low-order filters are used. For the configuration investigated subsequently, first-order filter structures were sufficient for stabilization.

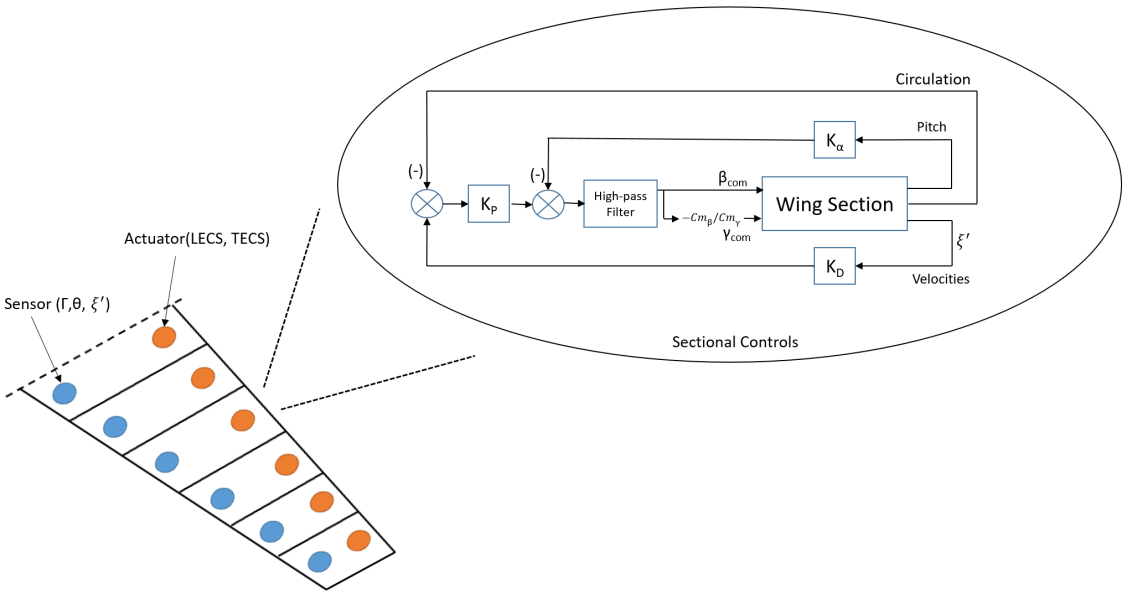

Figure 6.1: Distributed Sensing and Controls Framework

6.3 Results

The control approach is evaluated using the flexible flight analysis tool – ASWING. The sample configuration – Flying Wing UAV – available from Ref. [70] is used for analysis. The configuration is modified to include co-located sensor, actuator pairs distributed along the elastic axis. Linearization is performed at the specified velocity with boundary conditions corresponding to free-flight. Reduced order models (ROMs) are imported to the Simulink environment for controls design and analysis. ASWING's ROM procedure involves the use of an eigenmode expansion. Previous work [69] on this approach used outputs that are not accurately captured by the eignmode expansion [70]. In the following analysis, outputs that are not properly captured (such as accelerations, position with respect to earth axis or heading angle) are not used. The state-space based

ROMs generated from an eigenvalue analysis in ASWING are complex-valued. To convert to a real-valued form, a state-space model is identified from the pulse response of the time-discretized model using the Eigenvalue Realization Method [71]. Actuator dynamics are subsequently added to the model.

The following analysis is reported herein: (1) Open-loop characterization, (2) Closed-loop analysis and the effect of gains K_P,K_α and K_D, (3) Robustness and (4) Comparison with LQG.

6.3.1 Open-Loop Characteristics

Planform Parameters	Value	Mass Properties	Value
Area	212.4 ft^2	Total Weight	11.02 slug
Span	78.3 ft	CG Location	4.188 ft from nose
Aspect Ratio	28.9	Pitch Inertia (about CG)	47.59 slug-ft^2
Taper Ratio	0.6	Roll Inertia (about CG)	2901 slug-ft^2
Mean Aerodynamic Chord	2.5 ft	Yaw Inertia (about CG)	2948 slug-ft^2
Wing LE Sweep	11.3 deg		

Table 6.1: System Parameters: BFF Vehicle

The planform description and the mass properties of the flying wing configuration are listed in Table 6.1. Note the substantial high aspect ratio and wing sweep are conducive for BFF instability. Figure 6.2 shows the variation of system eigenvalues as the velocity

increases from 40 to 80 ft/s. The lightly damped BFF mode turns unstable at $U = 65$ ft/s. The BFF mode shape at $U = 70$ ft/s is shown in Fig. 6.3. Note the mode is comprised of contributions from the pitch rigid body mode and structural bending. The analysis shown in Fig. 6.2, closely resembles that found in Ref. [70], thus validating the ROM/model import procedure to the Simulink environment. The ASE model consists of 56 states.

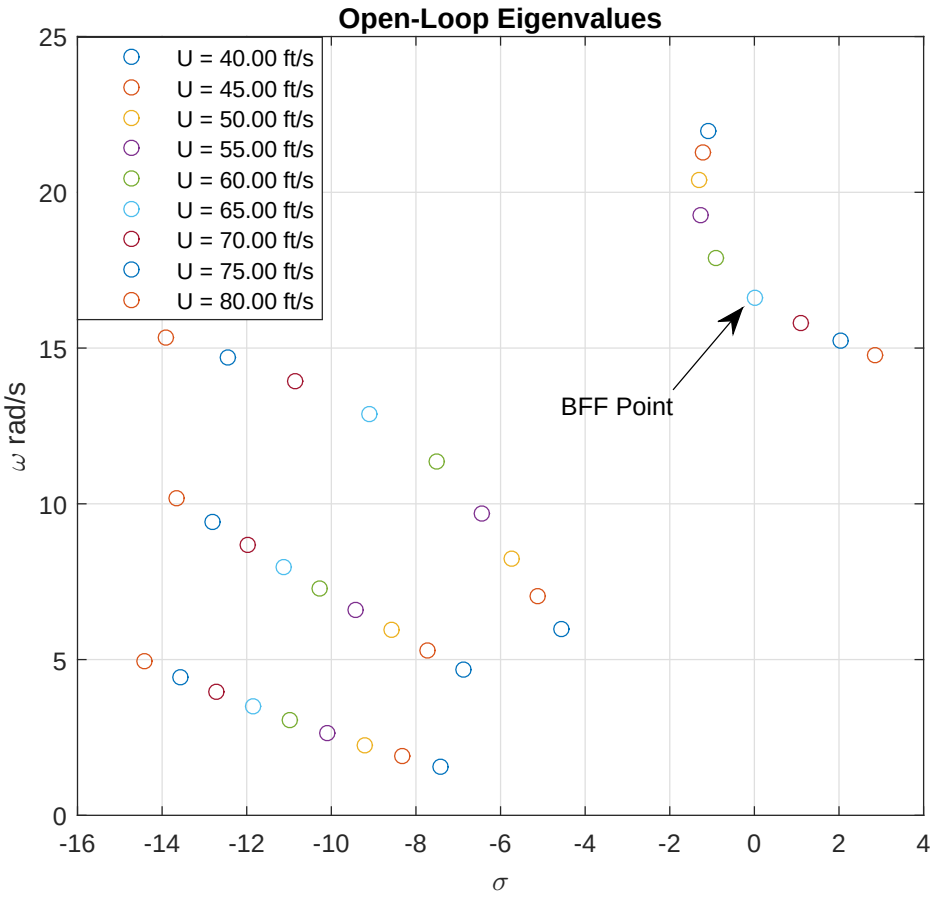

Figure 6.2: System Eigenvalues with Freestream Velocity

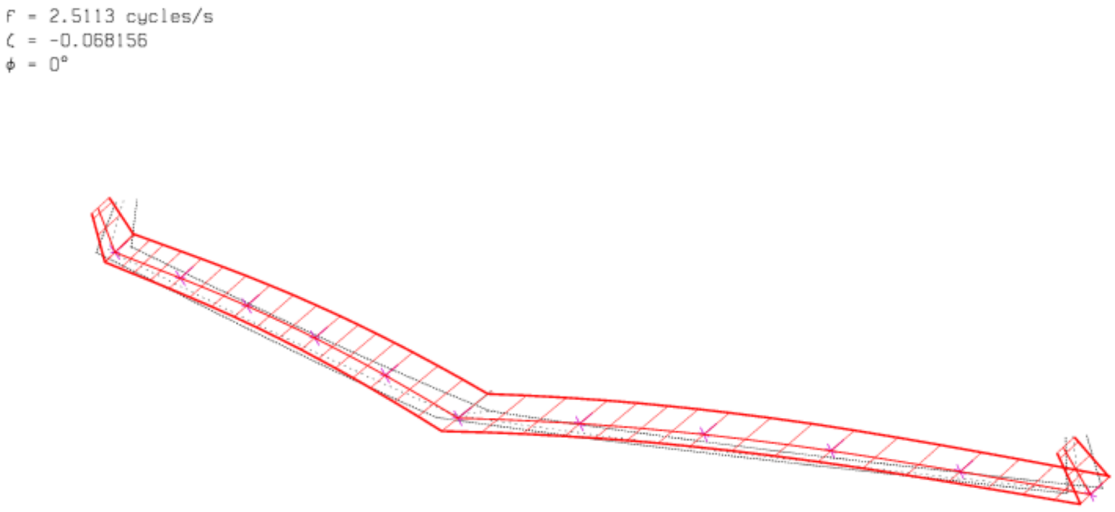

Figure 6.3: BFF Mode Shape, U = 70 ft/s

6.3.2 Closed-Loop Analysis

To implement closed-loop controls, the flying wing is divided into 5 sections consisting of co-located sensors and actuators. The control surface size (both leading and trailing edge) is set at 20% chord. Ref. [72] provides sectional control derivatives: $C_{L_\beta} = 3.45, C_{M_\beta} = -0.64, C_{L_\gamma} = 0.25, C_{M_\gamma} = 0.16$. The cut-off frequency for the high-pass filter is chosen to approximately match that of the BFF mode at 2 Hz. The filter is specified to be first-order of the form $\frac{T_s s}{T_s s+1}$. The filter acts on the 5 sections, and thus, the controller consists of only 5 states. In addition, actuator dynamics are added to each of the 5 control inputs. The dynamics is specified to be a first-order low pass filter (of the form: $\frac{1}{T_s s+1}$) with a cut-off at 10 Hz. The high-pass, low-pass filter (notch filter) combination ensures that the controller operates only on the high-frequency modes relevant to BFF. Actuator limits are specified as +/- 25 deg. The tracking signal for the

lift coefficient, is specified as $C_{L_{ref}} = K_d \left(\frac{-\dot{R}_z}{U} \right)$. Ref. [68] provides further details on the sign conventions and other relevant definitions used in ASWING. The lag terms arising from $\frac{d\Gamma}{dt}$, though appearing in the ASE model are ignored for feedback, since quasi-steady forces are expected to dominate. The lag terms will be significant for large reduced frequencies.

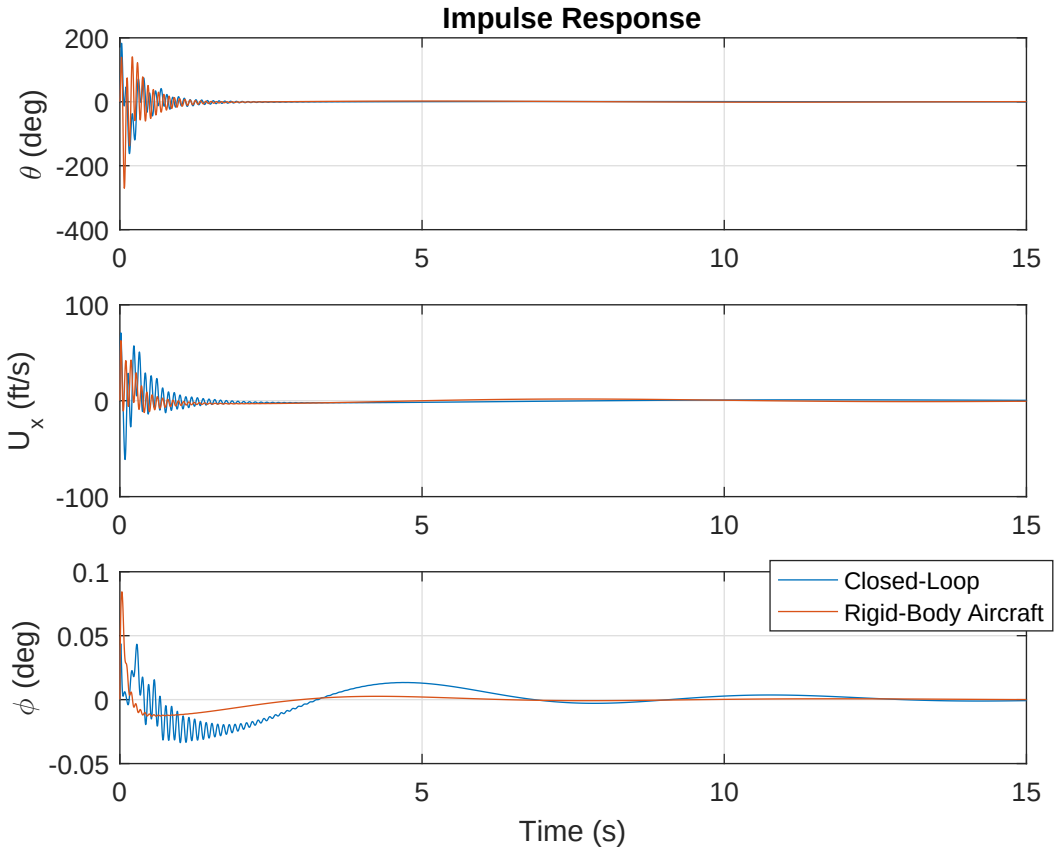

Figure 6.4: Closed-loop Characteristics, U = 100 ft/s

Figure 6.4 shows the impulse response of closed-loop system at $U = 100$ ft/s, approximately 50% higher than the flutter speed. The impulse is applied equally across all

TECS inputs (with LECS following the structure shown in Fig. 6.1). The outputs across the sections are averaged. The control gains are specified as: $K_\alpha = 1, K_P = 1, K_D = 6$. Three outputs are shown: pitch angle (θ), forward velocity (U_x) and roll angle (ϕ).

The dynamics of an equivalent rigid-body dynamics aircraft is overlaid for comparison. The rigid-body flight dynamics is generated by increasing the bending and torsional stiffness values to 10 times the baseline. Observe that though the closed-loop system is stabilized, residual high-frequency dynamics remain that are however quickly damped out within 1.5 secs. Damping may be increased by increasing the K_D gain. However, this will lead to larger control inputs and possibly instability for large values. Also, note that the low frequency modes associated with the longitudinal dynamics are relatively more damped when compared to the lateral mode. This is due to the high-pass filter having a cut-off frequency in the vicinity of the short-period mode and the action of rejecting the airfoil pitch contribution through gain, K_α. As a result, the stabilization effect partially extends to the low-frequency pitch mode. However, there is a minor spillover effect onto the lateral modes that is destabilizing (compared with the rigid-body mode).

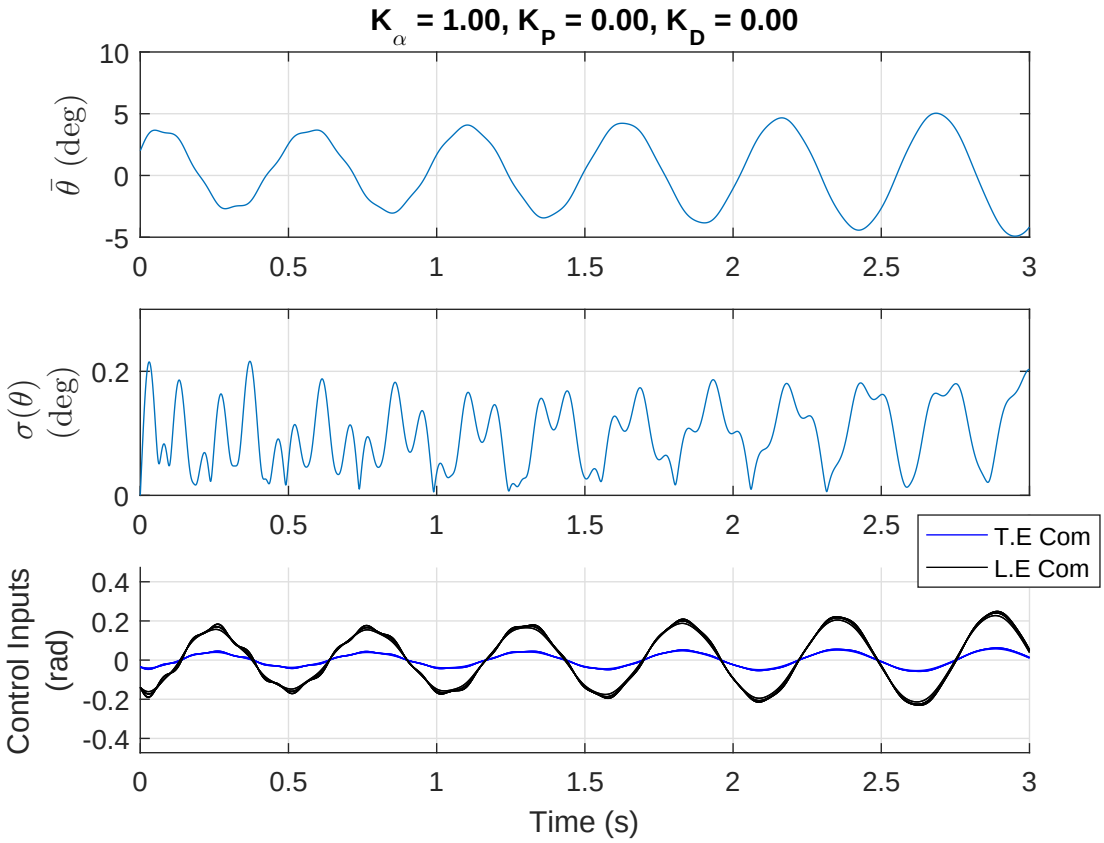

Figure 6.5: Effect of Gains on Controller Performance (K_α), U = 100 ft/s

Figures 6.5, 6.6 and 6.7 show the progressive effect of including the three gains – K_α, K_P, K_D – on controller performance. Specifically, the effect on the pitch mode is investigated. The mean pitch angle across sections $\bar{\theta}$ representing the rigid-body dynamics and the standard deviation $\sigma(\theta)$ representing the deformation is shown. The time-domain simulations are shown for an initial condition where the initial pitch angle across all sections is specified: $\theta_1..\theta_n = 2$ deg. The initial state is computed from the pseudo-inverse of the equivalent state-space C_θ matrix, $x_0 = pinv(C_\theta)[\theta_1..\theta_n]^T$. Figure 6.5 shows that marginal stability may be achieved by simply rejecting the pitch contribution through the

gain K_α. Note that high K_α gains may result in large control inputs. Therefore, for tuning the gains, it is suggested to tune K_α first to ensure control inputs are within limits. Improved stability is found by introducing feedback gain K_P (Fig. 6.6). As a result of feedback, the closed-loop system may show improved robustness to uncertainty and external disturbances.

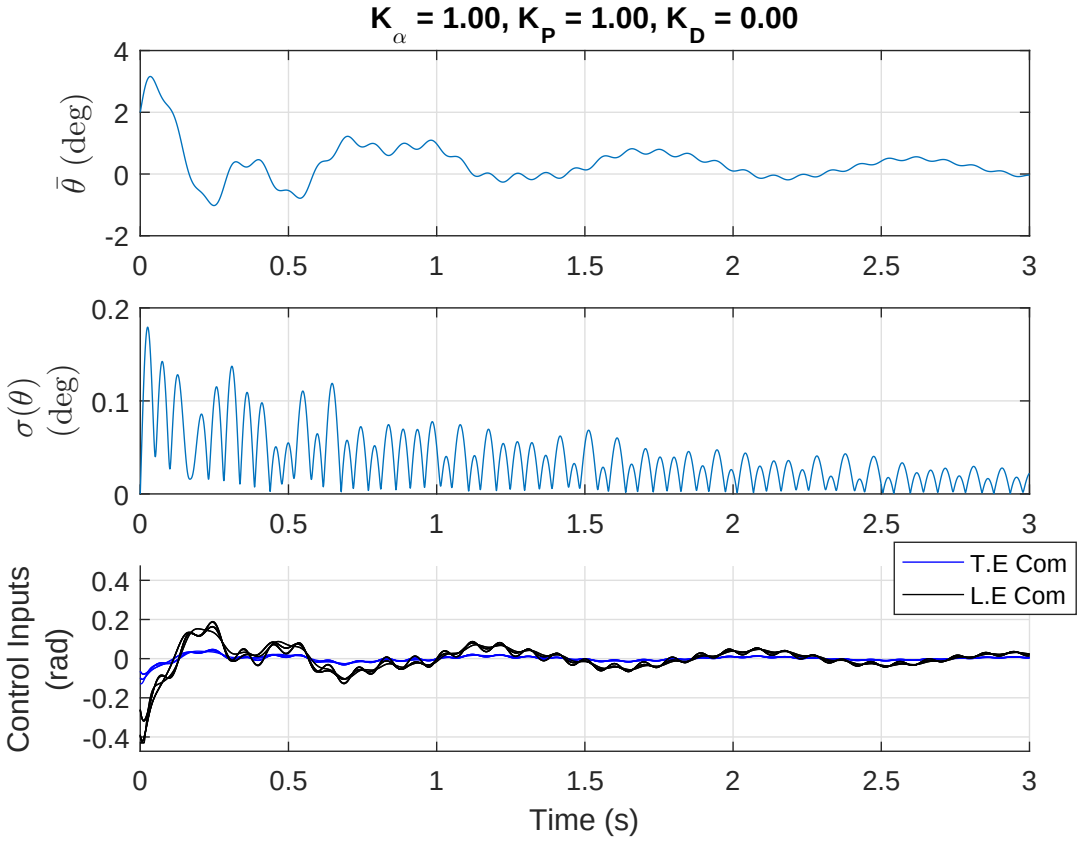

Figure 6.6: Effect of Gains on Controller Performance (K_α, K_P), U = 100 ft/s

The closed-loop response shows residual high-frequency components that are eventually damped out (See $\bar{\theta}$ and $\sigma(\theta)$ time histories). Improved damping is achieved through the energy dissipation gain, K_D (See Fig. 6.7). System responses are stabilized within 1 sec. Note that higher gains will yield better system performance but will also

result in larger control inputs and lower stability margins. Similar behavior of these gains on controller performance was observed in closed-loop aeroelastic wind tunnel tests as noted in Section 5.

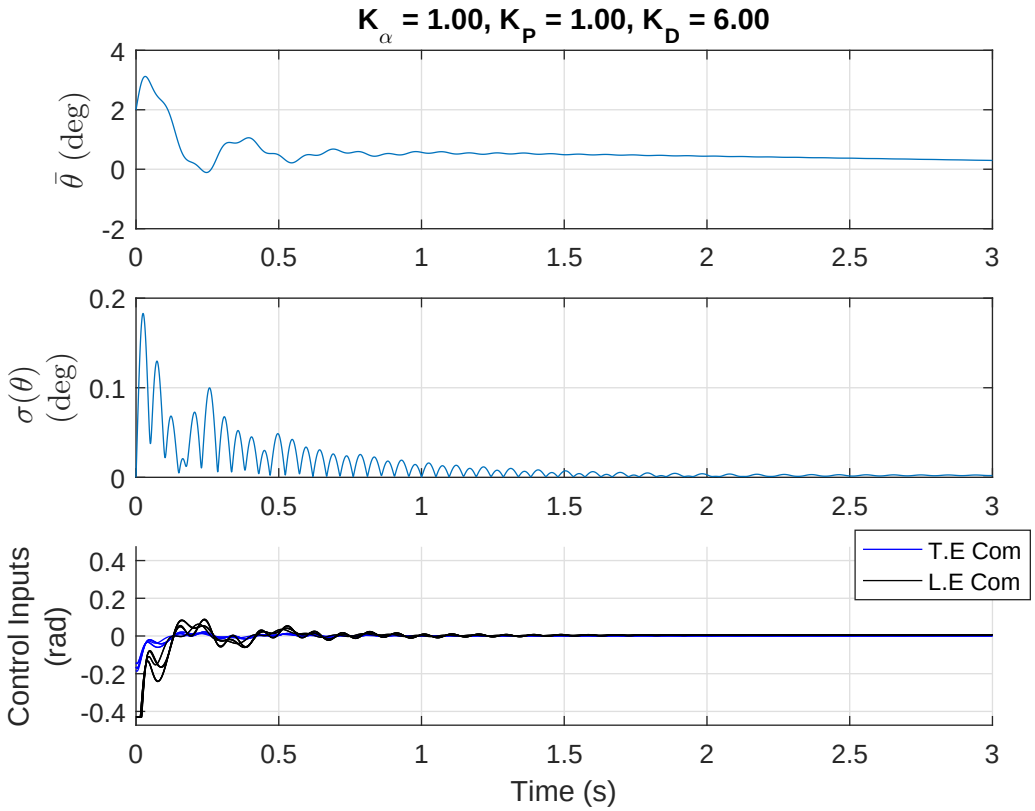

Figure 6.7: Effect of Gains on Controller Performance (K_α, K_P, K_D), U = 100 ft/s

6.3.3 Robustness

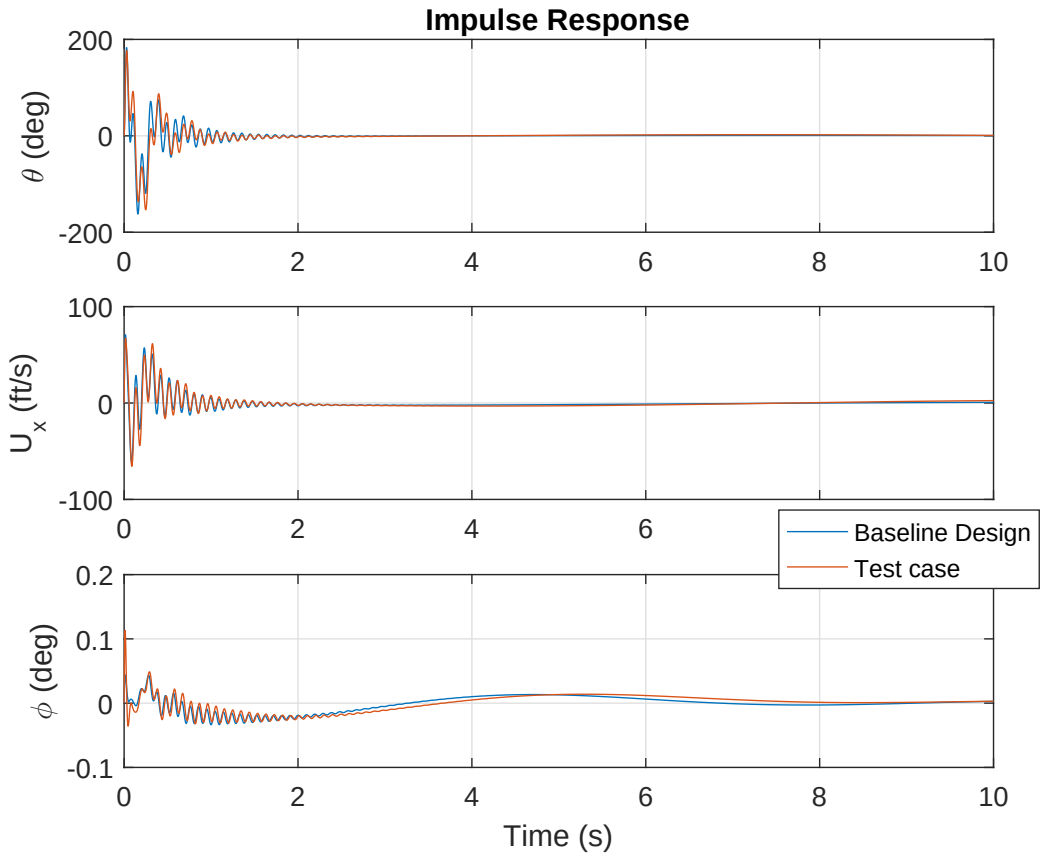

Figure 6.8: Controller Robustness (Energy-Based), U = 100 ft/s

The controller sensitivity to model variation is investigated by testing the control law on a "Test" configuration with a 8% change in the CG location (moved aft). Note that the controller does not use a model-based state-estimator and therefore is expected to show some measure of robustness against uncertainty. Figure 6.8 shows the closed-loop impulse response of both "Baseline" and "Test" configurations. The input/output definitions and gains follow those specified in Fig. 6.4. The results show that the behavior

of high-frequency dynamics are mostly unchanged. Minor variations are seen for the low frequency lateral mode.

6.3.4 Comparison with LQG

The low-order energy-based approach is compared with a conventional high-order, dynamic output-feedback LQG controller to illustrate potential benefits of this novel scheme. The LQG controller is synthesized by coupling a full-state feedback LQR controller with a Kalman filter. The previous control architecture of using co-located sensors and actuators (5 sections) is adopted to aid in comparison. However, to mimic the common approach of using inertial sensors, aerodynamic sensors (e.g., circulation) are not included. Inertial-sensor-based measurements – θ, ϕ, U_x, U_z – are made available at every section for output feedback. The closed-loop impulse response for both the baseline and test configuration are shown (conditions identical to previous section). In addition, the closed-loop response of the system for 2 deg pitch initial condition described previously is also provided.

The tuning matrices for the LQR controller ($Q = 0.1, R = 1$) and the Kalman filter ($Q = 0.1, R = 1$), all of which are diagonal, were designed to minimize closed-loop response variations to system changes and also maintain saturation constraints on the control inputs.

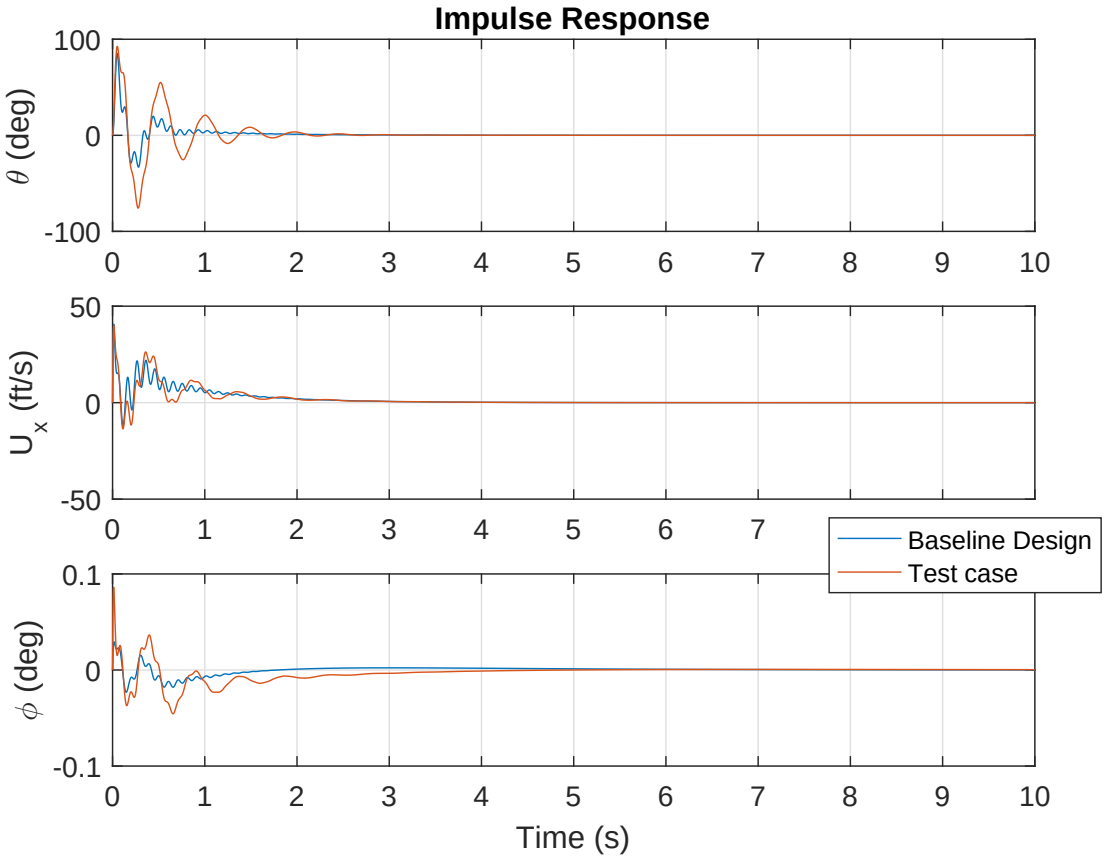

Figure 6.9: Controller Robustness (LQG), U = 100 ft/s

Figure 6.9 shows stabilization for both high-frequency and low frequency modes. System responses are damped within 2 secs. As observed, the Kalman filter does account for model variations to some extent, though not to the extent observed for energy-based approach. An alternative approach with performance guarantees under uncertainty is to use the H_∞ framework. However, the controller order will increase due to addition of weighting filters. The closed-loop response given an initial condition (Fig. 6.10) closely resembles that of Fig. 6.7 suggesting that the energy-based approach is near optimal (for comparable settling time and control effort).

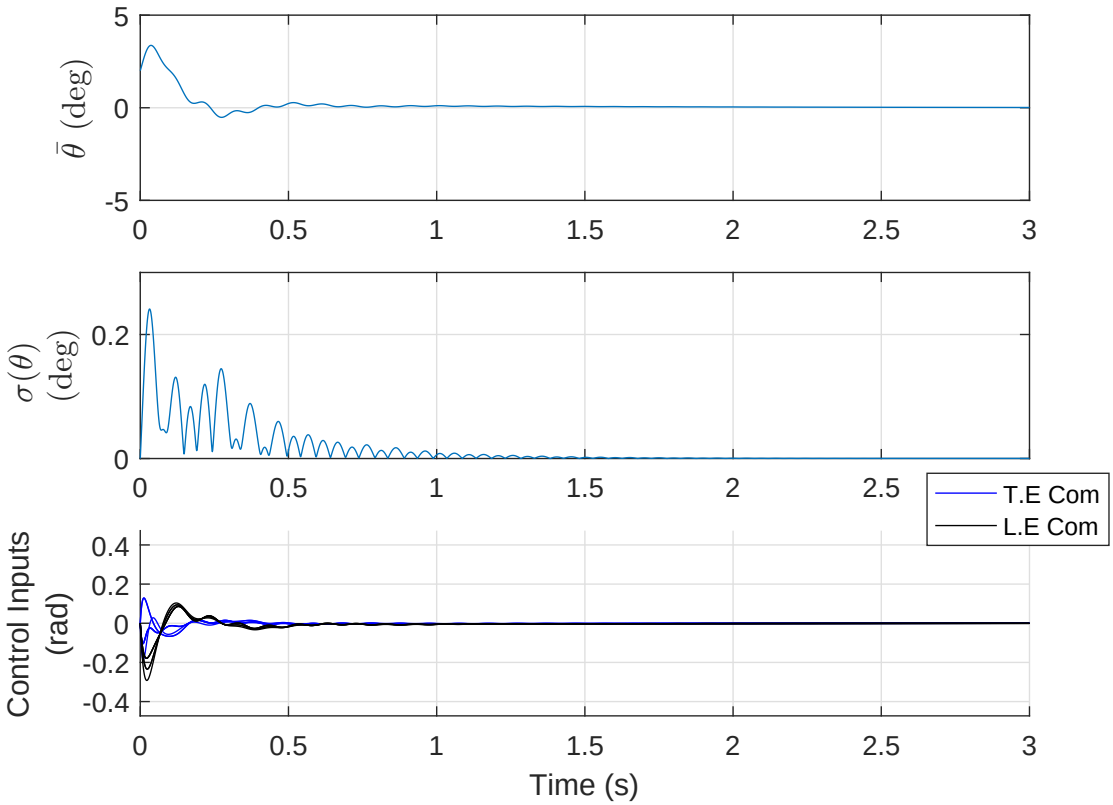

Figure 6.10: Closed-Loop Response (LQG), 2 deg Pitch Initial Condition, U = 100 ft/s

The controller order synthesized using LQG (size: 56) is dependent on the dynamics of the system whereas that of the energy-based method (size: 5) depends on the number of wing sections (through the use of high-pass filters). Reducing the size of the LQG controller using balanced realization, a minimum size of 19 states were found necessary for stability (with a subsequent loss of performance). Although, the control subsystem for stability augmentation/BFF suppression is of low order, the overall flight control system including subsystems handling rigid-body flight dynamics may be of a larger order. However, as suggested in Ref. [4], the use of low-order classical control techniques for the

flexible flight dynamics problem offers the advantage of simple, transparent, physics-based control designs. Modern state-feedback approaches offer a systematic, unified treatment of rigid and flexible aircraft dynamics, but tend to produce complex, high-order designs.

7 CONCLUSIONS AND FUTURE WORK

Important conclusions drawn from this research are summarized in this section and topics for future research are outlined.

7.1 Conclusions

Aeroservoelastic systems are inherently complex exhibiting features such as large dimensionality, significant uncertainty and nonlinearities. Consequently, the conventional inertial sensor-based state-feedback approach for aeroelastic stabilization may show conservative performance due to the inability to handle systemic complexities. Efficient controller synthesis for high performance aeroelastic stabilization may require a fundamentally different approach. In this research, the "Fly-By-Feel" sensing concept is investigated as an alternative control method. This sensing framework may potentially provide aerodynamic state estimates with tighter uncertainty bounds. Furthermore, real-time aerodynamic load measurements may be used directly in output-feedback using robust low-order controller structures for aeroelastic stabilization. Conclusions are summarized as follows:

1. The theoretical development using potential flow assumptions concerning the LESP, an aerodynamic observable, and its significance for unsteady aerodynamics and aeroservoelasticity was presented. Using important results derived by Theodorsen,

a simple first-order accurate model relating the LESP to the unsteady lift was developed. The theory accounted for various boundary conditions – pitch, plunge and control surface motions. In addition, the linearity of the formulation permitted the inclusion of thickness and camber effects. The theory confirmed intuition that the LESP is directly related to circulatory lift. Incorporating the LESP resulted in a significant simplification over conventional models such as Theodorsen that is based only on airfoil kinematics. In using the LESP, a dynamical model (transfer function or aerodynamic lag states) is not required to account for the wake generated by an oscillating airfoil. For low reduced frequencies, further simplification resulted in a model that requires only the LESP and the control surface deflection measurements. The analytical model was then validated using numerical simulations and experiments. The results emphasize the advantage of the LESP over the geometric angle of attack in measuring circulation. The numerical results in addition to verifying the model, quantified the effects of several nuances such as thickness, viscous effects, reduced frequency and approximating the nose region as a parabola. For instance, the LESP rate $\dot{\delta}$ was shown to have a significant effect only for relatively high reduced frequencies ($k > 0.2$). The experimental results apart from verifying the theory for steady flows, unsteady pitch and plunge maneuvers, validated additional scenarios such as control surface oscillations and gusts that were not considered for the numerical studies. The theory predictions agreed well with the load sensor estimates for C_L. However, the experimental results revealed a small phase-lag

between C_L estimated from the LESP and that from the load sensor mainly due to the hot-film substrate heat loss. The phase-lag was corrected using a first-order filter.

2. A sensor framework designed for unsteady lift measurements was implemented on a recently constructed aeroservoelastic experimental facility at Texas A&M university. The facility consists of a pitch-plunge drive system and a nonlinear aeroservoelastic apparatus. The facility with the integrated sensor framework is useful for studies of significance to aeroservoelasticity – limit cycle oscillations, active flutter suppression in the presence of gusts or unsteady aerodynamic identification. System identification procedures for the facility were developed and validated. Methods to estimate aerodynamic loads were developed for three sensor configurations based on force/torque transducers, hot-film sensors and airfoil kinematics. Associated physics-based models were developed and validated. The force transducer sensor model was first validated by comparing the inertial load predictions with load measurements in a wind-off test. For small amplitude oscillations, it was found that loads estimated by the three sensor configurations were in close agreement with minor discrepancies. To account for these errors, methods for model calibration were developed with the load sensor as a calibration reference. Discrepancies in load predictions using kinematics are primarily due to the inherent small-disturbance potential flow assumptions involved in Theodorsen's model. The model was tuned based on experimental data using a prediction-error

minimizing algorithm. Apart from directly identifying the LESP from a calibrated high-resolution sensor array, it was shown that it is possible to estimate the LESP using an uncalibrated sparse sensor array using the nonlinear PCA technique.

3. A physics-based active control method was developed for the purpose of aeroelastic stabilization using Fly-By-Feel sensing. The method involves the use of the LESP to control aerodynamic loads such that their effect on the structure is energy dissipative. Energy-based methods are utilized to determine structural rate signals for load reference tracking that are stabilizing. Tracking performance is improved by rejecting known components of lift (predominantly the pitch angle for low reduced frequencies). The stability margins of the control structure were assessed graphically using the aerodynamic work functional concept. Computational and experimental studies were conducted to evaluate controller performance. A state-space aeroservoelastic model was derived for the purpose of linear frequency-domain analysis and nonlinear time-domain simulations. Using the simulation tool, the controller was shown to stabilize nonlinear behavior such as LCOs as well as expand the flutter envelope. The capability of the controller in suppressing LCOs was also experimentally demonstrated using the NATA-II apparatus. Simultaneous aeroelastic stabilization and gust load alleviation was demonstrated. Computational and experimental studies were performed to investigate the effect of controller gains. The study may be useful to guide derivation of optimal gains for this control

structure. In contrast to the high-order state-feedback approach, the proposed control structure that was shown to be effective for aeroelastic stabilization is of low-order since the use of a complex (high-order, nonlinear and uncertain) aeroservoelastic state estimator is avoided. The simplicity of the control structure is therefore attractive for hardware implementation, verification and validation procedures.

4. The sectional load-based feedback control method was then extended to a flying wing configuration using a distributed sensing and controls architecture. Using output feedback of aerodynamic loads and inertial measurements (pitch, velocities), the approach is shown to be effective in suppressing body freedom flutter of a flying wing configuration. A first-order high-pass filter is used to ensure the controller operates in the frequencies relevant to the BFF mode. An ASE model is desirable to tune controller gains and characterize performance. However, a high-order state-estimator is not required, and therefore, the controller shows robustness to modest model variations. Overall, the low-order energy-based control method achieves favorable stabilization performance with good robustness characteristics for the targeted unstable aeroelastic mode. However, since BFF involves a rigid-body mode, the control system for flutter suppression will show some coupling with subsystems handling the short-period mode. The performance of this novel control scheme was then compared with the conventional LQG control formulation.

7.2 Future Work

The following opportunities for future research are identified:

(a) Although the sectional unsteady theory developed herein is capable of partially accounting for finite-span effects through the approximation of downwash as an equivalent plunge velocity, characterization of the LESP behavior for swept finite-span wings through numerical simulations and experiments are necessary for accurate span-wise load estimates.

(b) The developments in this research are limited to small amplitude airfoil maneuvers. Extensions to large angle of attack maneuvers will be required for sensing and control applications involving phenomena such as dynamic stall.

REFERENCES

[1] Livne, E., "Integrated Aeroservoelastic Optimization: Status and Direction," *Journal of Aircraft*, Vol. 36, No. 1, 1999, pp. 122–145.

[2] Mangalam, S., Mangalam, A., and Flick, P., "Unsteady Aerodynamic Observable for Gust Load Alleviation and Flutter Suppression," *26th AIAA Applied Aerodynamics Conference*, American Institute of Aeronautics and Astronautics, Honolulu, HI, Aug. 2008.

[3] Keel, L. H. and Bhattacharyya, S. P., "Robust, Fragile, or Optimal?" *IEEE Transactions on Automatic Control*, Vol. 42, No. 8, 1997, pp. 1098–1105.

[4] Schmidt, D. K., "Stability Augmentation and Active Flutter Suppression of a Flexible Flying-Wing Drone," *Journal of Guidance, Control, and Dynamics*, Vol. 39, No. 3, 2015, pp. 1–14.

[5] Suryakumar, V. S., Babbar, Y., Strganac, T. W., and Mangalam, A. S., "Unsteady Aerodynamic Model based on the Leading-Edge Stagnation Point," *Journal of Aircraft*, Vol. 53, No. 6, 2016, pp. 1626–1637.

[6] Mukhopadhyay, V., "Historical Perspective on Analysis and Control of Aeroelastic Responses," *Journal of Guidance, Control, and Dynamics*, Vol. 26, No. 5, 2003, pp. 673–684.

[7] Livne, E., "Future of Airplane Aeroelasticity," *Journal of Aircraft*, Vol. 40, No. 6, 2003, pp. 1066–1092.

[8] Weisshaar, T. A., "Static and Dynamic Aeroelasticity," *Encyclopedia of Aerospace Engineering*, John Wiley & Sons, Ltd, Chichester, UK, Dec. 2010.

[9] Pendleton, E. W., Bessette, D., Field, P. B., Miller, G. D., and Griffin, K. E., "Active Aeroelastic Wing Flight Research Program: Technical Program and Model Analytical Development," *Journal of Aircraft*, Vol. 37, No. 4, 2000, pp. 554–561.

[10] Jones, J. and Cesnik, C. E., "Nonlinear Aeroelastic Analysis of the X-56 Multi-Utility Aeroelastic Demonstrator," *15th Dynamics Specialists Conference, AIAA SciTech*, San Diego, CA, Jan. 2016.

[11] Lucia, D., "The SensorCraft Configurations: A Non-Linear Aeroservoelastic Challenge for Aviation," *46th AIAA/ASME/ASCE/AHS/ASC Structures, Structural Dynamics & Materials Conference*, Austin, Texas, April 2005.

[12] Vartio, E., Shaw, E., and Vetter, T., "Gust Load Alleviation Flight Control System Design for a SensorCraft Vehicle," *26th AIAA Applied Aerodynamics Conference*, American Institute of Aeronautics and Astronautics, Honolulu, HI, Aug. 2008.

[13] Waszak, M. R., "Modeling the Benchmark Active Control Technology Wind-Tunnel Model for Application to Flutter Suppression," *AIAA Atmospheric Flight Mechanics Conference*, San Diego, CA, July 1996.

[14] O', T., Neil, and Strganac, T. W., "Aeroelastic Response of a Rigid Wing Supported by Nonlinear Springs," *Journal of Aircraft*, Vol. 35, No. 4, 1998, pp. 616–622.

[15] Strganac, T. W., Ko, J., and Thompson, D. E., "Identification and Control of Limit Cycle Oscillations in Aeroelastic Systems," *Journal of Guidance, Control, and Dynamics*, Vol. 23, No. 6, 2000, pp. 1127–1133.

[16] Block, J. J. and Strganac, T. W., "Applied Active Control for a Nonlinear Aeroelastic Structure," *Journal of Guidance, Control, and Dynamics*, Vol. 21, No. 6, 1998, pp. 838–845.

[17] Ko, J., Strganac, T. W., and Kurdila, A. J., "Adaptive Feedback Linearization for the Control of a Typical Wing Section with Structural Nonlinearity," *Nonlinear Dynamics*, Vol. 18, No. 3, 1999, pp. 289–301.

[18] Kurdila, A. J. and Akella, M. R., "Nonlinear Control Methods for High-Energy Limit-Cycle Oscillations," *Journal of Guidance, Control, and Dynamics*, Vol. 24, No. 1, 2001, pp. 185–192.

[19] Platanitis, G. and Strganac, T. W., "Control of a Nonlinear Wing Section Using Leading- and Trailing-Edge Surfaces," *Journal of Guidance, Control, and Dynamics*, Vol. 27, No. 1, 2004, pp. 52–58.

[20] Prime, Z., Cazzolato, B., Doolan, C., and Strganac, T., "Linear-Parameter-Varying Control of an Improved Three-Degree-of-Freedom Aeroelastic Model," *Journal of Guidance, Control, and Dynamics*, Vol. 33, No. 2, 2010, pp. 615–619.

[21] Noll, T. E., Perez-Davis, M. E., Ishmael, S. D., Tiffany, G. C., and Gaier, M., "Investigation of the Helios Prototype Aircraft Mishap Volume I Mishap Report," `http://www.nasa.gov/pdf/64317main_helios.pdf`, Accessed: 2016-11-20.

[22] Silva, W. A., Piatak, D. J., and Scott, R. C., "Identification of Experimental Unsteady Aerodynamic Impulse Responses," *Journal of Aircraft*, Vol. 42, No. 6, 2005, pp. 1548–1551.

[23] Leishman, J. G. and Beddoes, T. S., "A Semi-Empirical Model for Dynamic Stall," *Journal Of The American Helicopter Society*, Vol. 34, No. 3, 1989, pp. 3–17.

[24] Mangalam, A. S. and Brenner, M. J., "Fly-by-Feel Sensing and Control: Aeroservoelasticity," *AIAA Atmospheric Flight Mechanics Conference*, American Institute of Aeronautics and Astronautics, Atlanta, GA, June 2014.

[25] Vogel, J. and Kelkar, A., "Aircraft Control Augmentation and Health Monitoring Using Flush Air Data System Feedback," *26th AIAA Applied Aerodynamics Conference*, American Institute of Aeronautics and Astronautics, Honolulu, HI, Aug. 2008.

[26] Mangalam, S. M., Flick, P. M., and Brenner, M. J., "Higher Level Aerodynamic Input for Aeroservoelastic control of Flexible Aircraft," *Proceedings of the AIAA Atmospheric Flight Mechanics Conference and Exhibit*, American Institute of Aeronautics and Astronautics, Hilton Head, SC, Aug. 2007.

[27] Woods, L. C., "The Lift and Moment Acting on a Thick Aerofoil in Unsteady Motion," *Philosophical Transactions of the Royal Society A: Mathematical, Physical and Engineering Sciences*, Vol. 247, No. 925, Nov. 1954, pp. 131–162.

[28] Woods L.C., *The Theory of Subsonic Plane Flow*, Cambridge University Press, 2011.

[29] Mangalam, A. and Moes, T., "Real-Time Unsteady Loads Measurements Using Hot-Film Sensors," *22nd Applied Aerodynamics Conference and Exhibit*, American Institute of Aeronautics and Astronautics, Providence, RI, Aug. 2004.

[30] Mangalam, A. and Davis, M., "Ground/Flight Correlation of Aerodynamic Loads with Structural Response," *47th AIAA Aerospace Sciences Meeting including The New Horizons Forum and Aerospace Exposition*, American Institute of Aeronautics and Astronautics, Orlando, FL, Jan. 2009.

[31] Mangalam, A., Moore, G., Berg, D., Blaylock, M., and Rumsey, M., "Real-Time Aerodynamic Observable for Wind Turbine Applications," *51st AIAA/ASME/ASCE/AHS/ASC Structures, Structural Dynamics, and Materials Conference*, American Institute of Aeronautics and Astronautics, Orlando, FL, April 2010.

[32] Mangalam, A., Jutte, C., and Brenner, M., "Aerodynamic and Structural Measurement of the Aerostructures Test Wing for Flutter Testing," *AIAA Atmospheric Flight Mechanics Conference*, American Institute of Aeronautics and Astronautics, Toronto, Canada, Aug. 2010.

[33] Van Dyke, M. D., "Second-Order Subsonic Airfoil Theory Including Edge Effects," Tech. Rep. NACA-TR-1274, NACA, 1956.

[34] McCroskey, W., "Inviscid Flowfield of an Unsteady Airfoil," *AIAA Journal*, Vol. 11, No. 8, 1973, pp. 1130–1137.

[35] Theodorsen, T., "General Theory of Aerodynamic Instability and the Mechanism of Flutter," Tech. Rep. NACA-TR-496, NACA, 1949.

[36] Bisplinghoff, R. L., Ashley, H., and Halfman, R. L., *Aeroelasticity*, Dover Publications, 1983.

[37] Brunton, S. L., Rowley, C. W., and Williams, D. R., "Reduced-Order Unsteady Aerodynamic Models at Low Reynolds Numbers," *Journal of Fluid Mechanics*, Vol. 724, 2013, pp. 203–233.

[38] James, E. C., "Leading Edge Separation Criterion for an Oscillating Airfoil," Tech. Rep. AD-A148 249, Vehicle Research Corp Pasadena CA, 1984.

[39] Katz, J. and Plotkin, A., *Low-Speed Aerodynamics, Second Edition*, Vol. 126, Cambridge University Press, 2004.

[40] Wagner, H., "Über die Entstehung des dynamischen Auftriebes von Tragflügeln," *ZAMM - Zeitschrift für Angewandte Mathematik und Mechanik*, Vol. 5, No. 1, 1925, pp. 17–35.

[41] Bandyopadhyay, P. R., Beal, D. N., Hrubes, J. D., and Mangalam, A., "Relationship of Roll and Pitch Oscillations in a Fin Flapping at Transitional to High Reynolds Numbers," *Journal of Fluid Mechanics*, Vol. 702, July 2012, pp. 298–331.

[42] Jumper, E. J. and Hugo, R. J., "Loading Characteristics of Finite Wings Undergoing Rapid Unsteady Motions - A Theoretical Treatment," *Journal of Aircraft*, Vol. 31, No. 3, 1994, pp. 495–502.

[43] Drela, M. and Giles, M. B., "Viscous-Inviscid Analysis of Transonic and Low Reynolds Number Airfoils," *AIAA Journal*, Vol. 25, No. 10, 1987, pp. 1347–1355.

[44] Cebeci, T., Platzer, M., Chen, H., Chang, K.-C., and Shao, J. P., *Analysis of Low-Speed Unsteady Airfoil Flows*, Springer, Berlin, 2005.

[45] Babbar, Y., Suryakumar, V. S., and Strganac, T. W., "Experiments in Free and Forced Aeroelastic Response," *51st AIAA Aerospace Sciences Meeting including the New Horizons Forum and Aerospace Exposition*, American Institute of Aeronautics and Astronautics, Dallas, TX, Jan. 2013, pp. 1–10.

[46] Babbar, Y., Suryakumar, V. S., Strganac, T. W., and Mangalam, A. S., "Measurement and Modeling of Aeroelastic Response under Gust," *33rd AIAA Applied Aerodynamics Conference*, American Institute of Aeronautics and Astronautics, Dallas, TX, June 2015.

[47] Babbar, Y. and Suryakumar, V. S., "An Approach for Prescribed Experiments for Aerodynamic - Structural Dynamic Interaction," *51st AIAA Aerospace Science Meet-*

ing Including the New Horizons Forum and Aerospace Exposition, American Institute of Aeronautics and Astronautics, Dallas, TX, Jan. 2013.

[48] Menendez, A. N. and Ramaprian, B. R., "The Use of Flush-Mounted Hot-Film Gauges to Measure Skin Friction in Unsteady Boundary Layers," *Journal of Fluid Mechanics*, Vol. 161, Dec. 1985, pp. 139.

[49] Doorly, J. E. and Oldfield, M. L. G., "The Theory of Advanced Multi-Layer Thin Film Heat Transfer Gauges," *International Journal of Heat and Mass Transfer*, Vol. 30, No. 6, 1987, pp. 1159–1168.

[50] Cole, S. R., Noll, T. E., and Perry, B., "Transonic Dynamics Tunnel Aeroelastic Testing in Support of Aircraft Development," *Journal of Aircraft*, Vol. 40, No. 5, 2003, pp. 820–831.

[51] Piatak, D. J. and Cleckner, C. S., "Oscillating Turntable for the Measurement of Unsteady Aerodynamic Phenomena," *Journal of Aircraft*, Vol. 40, No. 1, 2003, pp. 181–188.

[52] Hurtado, J. E., *Kinematic and Kinetic Principles*, Lulu Press, Inc, 2014.

[53] Kramer, M. A., "Nonlinear Principal Component Analysis Using Autoassociative Neural Networks," *AIChE Journal*, Vol. 37, No. 2, 1991, pp. 233–243.

[54] Scholz, M., "Validation of nonlinear PCA," *Neural Processing Letters*, Vol. 36, No. 1, 2012, pp. 21–30.

[55] Jones, R. T., “Operational Treatment of the Nonuniform-Lift Theory in Airplane Dynamics,” Tech. Rep. NACA-TN-667, NACA, 1938.

[56] Ljung, L., *System Identification Toolbox, User's Guide*, The Mathworks Inc., 2016.

[57] Patil, M. J., “From Fluttering Wings to Flapping Flight: The Energy Connection,” *Journal of Aircraft*, Vol. 40, No. 2, 2003, pp. 270–276.

[58] Nissim, E., “Flutter Suppresson using Active Controls Based on the Concept of Aerodynamic Energy,” Tech. Rep. NASA TN D-6199, NASA Langley Research Center, 1971.

[59] Bendiksen, O. O., “Energy Approach to Flutter Suppression and Aeroelastic Control,” *Journal of Guidance, Control, and Dynamics*, Vol. 24, No. 1, 2001, pp. 176–184.

[60] Suryakumar, V. S., Babbar, Y., Strganac, T. W., and Mangalam, A. S., “Control of a Nonlinear Wing Section using Fly-by-Feel Sensing,” *AIAA Atmospheric Flight Mechanics Conference*, American Institute of Aeronautics and Astronautics, Dallas, TX, June 2015.

[61] Love, M. H., Zink, P. S., Wieselmann, P. A., and Youngren, H., “Body Freedom Flutter of High Aspect Ratio Flying Wings,” *46th AIAA/ASME/ASCE/AHS/ASC Structures, Structural Dynamics, and Materials Conference*, American Institute of Aeronautics and Astronautics, Austin, TX, April 2005.

[62] Schmidt, D. K., "MATLAB-Based Flight-Dynamics and Flutter Modeling of a Flexible Flying-Wing Research Drone," *Journal of Aircraft*, Vol. 53, No. 4, 2015, pp. 1045–1055.

[63] Simpson, R. J., Palacios, R., and Goulart, P. J., "Integrated Flight Dynamics and Aeroelasticity of Flexible Aircraft with Application to Swept Flying Wings," *56th AIAA/ASCE/AHS/ASC Structures, Structural Dynamics, and Materials Conference*, American Institute of Aeronautics and Astronautics, Kissimmee, FL, Jan. 2015.

[64] Richards, P. W., Yao, Y., Herd, R. A., Hodges, D. H., and Mardanpour, P., "Effect of Inertial and Constitutive Properties on Body-Freedom Flutter for Flying Wings," *Journal of Aircraft*, Vol. 53, No. 3, 2016, pp. 756–767.

[65] Leitner, M., Knoblach, A., Kier, T. M., Moreno, C. P., Kotikalpudi, A., Pfifer, H., and Balas, G. J., "Flight Dynamics Modeling of a Body Freedom Flutter Vehicle for Multidisciplinary Analyses," *AIAA Modeling and Simulation Technologies Conference*, American Institute of Aeronautics and Astronautics, Kissimmee, FL, Jan. 2015.

[66] Patil, M. J. and Hodges, D. H., "Flight Dynamics of Highly Flexible Flying Wings," *Journal of Aircraft*, Vol. 3, No. 6, 2006, pp. 1790–1799.

[67] Shearer, C. M. and Cesnik, C. E., "Nonlinear Flight Dynamics of Very Flexible Aircraft," *Journal of Aircraft*, Vol. 44, No. 5, 2007, pp. 1528–1545.

[68] Drela, M., "Integrated Simulation Model for Preliminary Aerodynamic, Structural, and Control-Law Design of Aircraft," *40th Structures, Structural Dynamics, and Ma-*

terials Conference and Exhibit, American Institute of Aeronautics and Astronautics, Cambridge, MA, April 1999.

[69] Suryakumar, V. S., Mangalam, A. S., Babbar, Y., and Strganac, T. W., "A Load-Based Feedback Approach for Distributed Aeroservoelastic Control," *AIAA Atmospheric Flight Mechanics Conference*, American Institute of Aeronautics and Astronautics, Washington D.C, June 2016.

[70] Drela, M., "ASWING," `http://web.mit.edu/drela/Public/web/aswing/`, Accessed: 2016-11-20.

[71] Juang, J. and Pappa, R. S., "An Eigensystem Realization Algorithm for Modal Parameter Identification and Model Reduction," *Journal of Guidance, Control, and Dynamics*, Vol. 8, No. 5, 2012, pp. 620–627.

[72] Dowell, E. H., Bliss, D. B., and Clark, R. L., "Aeroelastic Wing with Leading- and Trailing-Edge Control Surfaces," *Journal of Aircraft*, Vol. 40, No. 3, 2003, pp. 559–565.